Second-order computational homogenisation enhanced with non-uniform body forces for non-linear cellular materials and metamaterials

Ling Wu[a,*], Mohib Mustafa[a,b], Javier Segurado[b], Ludovic Noels[a]

[a]*University of Liege, Department of Mechanical and Aerospace Engineering, Computational & Multiscale Mechanics of Materials, Allée de la découverte 9, B-4000 Liège, Belgium*
[b]*IMDEA Materials Institute, Calle Eric Kandel 2, Getafe, 28906, Madrid, Spain*

Abstract

Although "classical" multi-scale methods can capture the behaviour of cellular, including lattice, materials, when considering lattices or metamaterial local instabilities, corresponding to a change of the micro-structure morphology, classical computational homogenisation methods fail. On the one hand, first order computational homogenisation, which considers a classical continuum at the macro-scale cannot capture localisation bands inherent to cell buckling propagation. On the other hand, second-order computational homogenisation, which considers a higher order continuum at the macro-scale, introduces a size effect with respect to the Representative Volume Element (RVE) size, which is problematic when the RVE has to consider several cells to recover periodicity during local instability. In this paper we reformulate in a finite-strain setting the second-order computational homogenisation using the idea of equivalent homogenised volume. From this equivalence, arises at the micro-scale a non-uniform body force that acts as a supplementary volume term over the RVE. In the presented method, this non-uniform body-force term arises from the equivalence of energy, i.e. the Hill-Mandel condition, between the micro- and macroscopic volumes and depends mainly on the relation between the micro-scale and macro-scale deformation gradient. We show by considering elastic and elasto-plastic metamaterials and cellular materials that this approach reduces the RVE size dependency on the homogenised response.

Keywords: Computational homogenisation, Second-order homogenisation, Cellular materials, Metamaterials

1. Introduction

Metamaterials are architectured materials with specially designed patterns at the meso-scale able to induce peculiar properties that are not observed in natural materials. They may possess a variety of properties depending on the applications that they are designed for. Mechanical metamaterials can provide properties such as negative effective bulk modulus [1], negative Poisson's ratio [2], finite bulk but vanishing shear modulus [3] or a high stiffness with an ultra low density [4]. Although the manufacturing of these materials cannot easily be achieved with traditional manufacturing methods, with the recent advances in 3D printing, the precision, repeatability and material ranges of 3D printing have reached a point such that some 3D processes are considered viable as an industrial-production technology and offer the possibility to produce the very complex meso-scale geometries inherent to metamaterials.

---

*Corresponding author
Email addresses:* `L.Wu@ulg.ac.be` (Ling Wu), `mohib.mustafa@imdea.org` (Mohib Mustafa), `javier.segurado@imdea.org` (Javier Segurado), `L.Noels@ulg.ac.be` (Ludovic Noels)

However, from the aspect of modelling, due to the complex internal geometry of metamaterials, Direct Numerical Simulations (DNS), which refer to the geometry of inner structure being explicitly meshed in simulations, are often limited to few unit cells, or few Representative Volume Elements (RVEs). The full-field numerical analysis of a structure made out of an architectured material can be prohibitively expensive, especially when a series of computations are required in the structure design phase. With the modern 3D printing techniques, scientists are able to build metamaterials of a variety of intricate patterns on a relatively small scale, allowing to treat them as a homogeneous medium, and a possible solution to circumvent the technical difficulties of DNS is to substitute the architectured material by a homogeneous one having equivalent effective properties. However, metamaterials act like an engineered structure, rather than a conventional bulk material, and since mid-60s in the seminal works of Mindlin, Toupin, and others [5–7], the researchers have investigated the theoretical formulation of continuum mechanics, concluding that the classical Cauchy elasticity is not always rich enough to model architectured materials. It has been shown that an effective description should involve additional degrees of freedom (Cosserat, micromorphic media [8, 9]) or high order gradients of the displacement [5].

To replace the complex micro-structural linear behaviour with an equivalent continuum model, homogenisation can be employed to extract an equivalent linear response. In order to consider higher-order effects, strain-gradient enhanced homogenisation of heterogeneous materials has been the subject of intense research. In [10, 11], a homogeneous Cosserat continuum was adopted to represent the effective behaviours of heterogeneous Cauchy medium. The high order strain gradients enhanced constitutive laws of heterogeneous materials with periodic micro-structures were established from an asymptotic analysis in the context of finite element modelling in [12], and using a combination of variational and asymptotic techniques in [13]. A Fast Fourier Transform approach was developed to compute the effective coefficients of a strain-gradient elastic model in [14]. A strain-gradient continuum of effective mechanical properties was constructed based on an equivalent strain energy, which is computed using a finite element approach, in [15]. Considering polynomial boundary conditions, which are extension of affine conditions and correspond to considering several spatial derivative orders of the displacement field on the unit cell, overall Cosserat, second gradient, or micromorphic homogeneous media were successively obtained depending on the choice of the polynomial in [16]. Micropolar and strain-gradient homogenisation schemes were applied to auxetic hexa- and tetra-chiral cells in [17], in which analytical expressions of the micropolar response and finite element method (FEM) estimations of the effective higher-order coefficients were respectively evaluated. Micropolar elastic continuum was also considered as homogenised media for random composites in [18] to study the RVE size effect on the effective properties. In [19], a polynomial displacement field was imposed on the unit cell of a periodic micro-structure, and the higher-order macroscopic constitutive responses were derived through a micro-mechanical method and compared to that obtained by asymptotic homogenisation. The effective coefficients of anisotropic first- and second-order displacement gradient linear elastic continuum models were identified from the response of the explicit representation of two-dimensional random fibre networks in [20]. In [21], based on FEM calculations of RVEs, Mindlins strain gradient elasticity was used to model as a homogeneous media local heterogeneous Cauchy linear architectured materials.

In the context of non-linear behaviours, such as finite deformation, using effective coefficients of high order moduli to define the second-order homogeneous continuum is not enough. Second-order computational homogenisation [22–24] incorporates $\mathbf{G}_\mathrm{M}$, the gradient of the macroscopic deformation gradient $\boldsymbol{F}_\mathrm{M}$, to form the boundary value problem on the RVE, and replaces the explicit high order constitutive model by online direct finite element resolutions of the RVE, see Fig. 1(a). More recently, micromorphic computational homogenisation framework was specifically developed to predict the buckling behaviour and patterning change of mechanical metamaterials [25, 26]. In this formalism, the patterning modes $\boldsymbol{\varphi}_i$ of a micro-structure are introduced as prior knowledge and the high order gradients of the displacement are replaced by the gradients of new macroscopic unknowns, which are the coefficients of those modes, see Fig. 1(b). Micromorphic computational homogenisation was also applied on auxetic tetra-chiral structure in [27].

In the context of substituting a complex micro-structural linear behaviour with an equivalent continuum model, polynomial boundary conditions, in particular Quadratic Boundary Conditions (QBC), which consider the strain gradient, prescribed on the RVE have been extensively used to determine higher-order effective properties [10, 11, 16, 23, 28, 29]. This method is popular since it is a straightforward extension
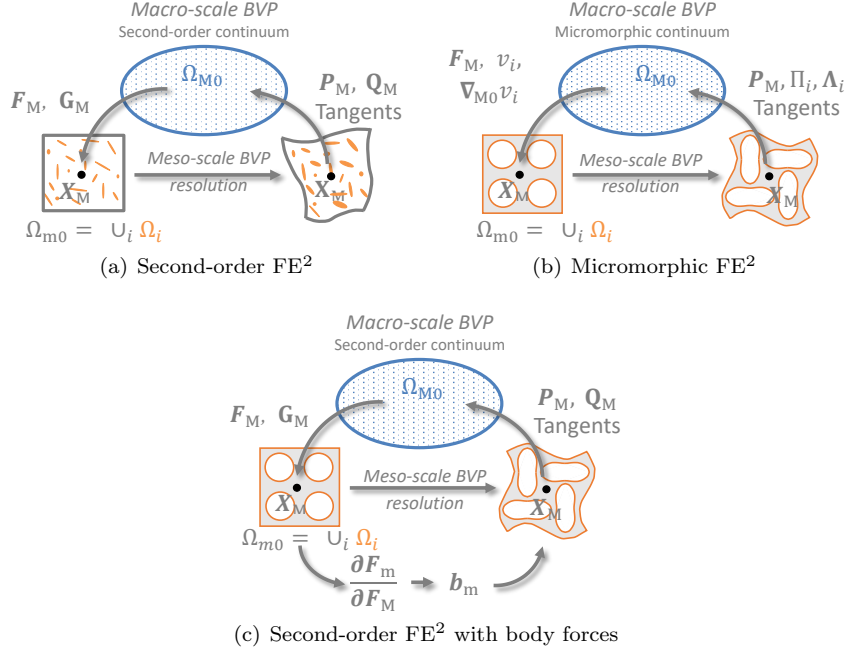
2

Figure 1: Higher-order computational homogenisation schemes: (a) Second-order homogenisation framework in which the macro-scale is enriched by the high order stress $\mathbf{Q}_M$ and the meso-scale problem boundary conditions are defined by both the macro-scale deformation gradient $\boldsymbol{F}_M$ and its gradient $\mathbf{G}_M = \boldsymbol{F}_M \otimes \nabla_{M0}$; (b) Micromorphic approach with patterning modes $\boldsymbol{\varphi}_i$ in which the modes amplitude v_i and amplitude gradient $\nabla_{M0}v_i$ are down-scaled with the macro-scale deformation gradient $\boldsymbol{F}_M$ to define the meso-scale boundary value problem whose resolution yields the homogenised stress $\boldsymbol{P}_M$ and stress like quantities Π_i and $\boldsymbol{\Lambda}_i$ satisfying $\nabla_{M0} \cdot \boldsymbol{\Lambda}_i = \Pi_i$; and (c) Developed enhanced second-order homogenisation framework in which a local body force $\boldsymbol{b}_m$, which depends on $\frac{\partial \boldsymbol{F}_m}{\partial \boldsymbol{F}_M}$, is introduced in the meso-scale boundary value problem.

of the classical Kinematic Uniform Boundary Conditions (KUBC) used in classical homogenisation [30] and some quadratic terms of QBC corresponding to bending modes are sufficient for the construction of an overall couple-stress medium [31]. Although this method has been used in numerous situations, its drawbacks have also been shown in numerical and analytical studies: first, the effective strain-gradient properties do not converge with respect to the RVE size [12, 16, 32]; and second, the effective strain-gradient properties remain non zero when a homogeneous Cauchy material volume is used as RVE [16, 21, 32] which is contradictory to the behaviour of Cauchy continuum. These drawbacks indicate that the use of QBC over the RVE is not always adequate to compute higher-order moduli, and all the components of the macroscopic strain gradient cannot be chosen arbitrarily to form QBC over the RVE, as pointed out in [33]. The asymptotic analysis on second-order problem shows that a body force arises naturally [33], and a body force is also derived from the local equilibrium equations in [21]. As a consequence, a uniform body force has been used as a part of the deformation constraints in [21], besides QBC, in the finite element analysis of the RVE. A uniform body force has also been introduced explicitly in the asymptotic analysis of higher-order homogenisation in [13]. In the micromorphic computational homogenisation [26], in order to constrain the deformation of the RVE, Lagrange multipliers, which act as body forces, were applied. The physical explanation for the need to introduce a body force is that applying the constraints at the boundary of the RVE alone do not propagate the gradient of deformation gradient to the RVE centre: numerical studies in [16] have shown a significant boundary layer effect when only RVE boundary constraints in gradient enhanced computational homogenisation are considered. As a consequence, the deformation remains mainly located in a boundary layer of the RVE, and leaves the central cell almost undeformed. This phenomenon is exacerbated when considering RVE of architectured periodic materials made of several unit cells. This case arises for some

3

heterogeneous materials, such as metamaterials for which a change in the micro-structure patterning occurs during the deformation, see Fig. 1(c). In that case, the RVE periodicity implies considering an assembly of several cells, whose number can be defined from a Bloch wave analysis [34, 35], yielding meso-scale RVEs that can have a comparable size to that of the macroscopic elements.

In multi-scale analyses, the validity of the homogenisation requires the size of the heterogeneity to be much smaller than the wavelength of the static mechanical loading on structures. However, when the meso-structure coarsens, the usual scale separation assumption, which assumes a uniform macroscopic field attribution to each RVE, does not hold anymore, and the effect of the macroscopic fields variation on the RVE length needs to be considered during the homogenisation process. This is particularly true when considering metamaterials for which capturing the change in the micro-structure patterning requires to consider a periodic RVE made of an assembly of unit cell as previously explained. In this case, not only the scale separation assumption in the multi-scale analysis does not hold anymore, but also using the microscopic volume-averaged response at a macroscopic material point becomes questionable. The gradient-enhanced computational homogenisation, which is illustrated in Fig. 1(a), has been developed in [36] to conduct FE^2 non-linear multi-scale analyses in this context. The macroscopic material follows the second-order continuum, and its constitutive law at each material point is replaced by the solution of a RVE boundary value problem which is defined by the macroscopic deformation gradient $\boldsymbol{F}_\mathrm{M}$ and its gradient $\mathbf{G}_\mathrm{M}$. However, with second-order homogenisation, the size of the RVEs directly relates to the characteristic length scale of the Mindlin strain gradient continuum [23]. As a consequence, for a cellular material made of a periodic micro-structure, considering a $N \times N$-unit cell RVE will not lead to the same structural response as considering a $2N \times 2N$-unit cell RVE as shown in [16, 37], preventing to define a RVE allowing to capture changes in the micro-structure patterning. Although this problem is avoided with the micromorphic approach, the latter requires to define a priori the number of modes that are handled during the approach.

In the present paper, an enhanced second-order computational homogenisation process is proposed using the idea of equivalent homogenised volume. In a RVE or unit cell, the microscopic material follows a Cauchy continuum, and the material in the corresponding macroscopic volume obeys a second-order continuum, but we assume that the volumes at micro- and macro-scales are equivalent in a volume-averaged sense. To this end, and considering a finite-strain setting, the body force, which has been used in higher-order homogenisation in an infinitesimal strain setting [13, 21, 33], results from the equilibrium equation of the macroscopic equivalent volume, and is applied to the microscopic counterpart of the equivalent volume, i.e. the RVE, see Fig. 1(c). This body force thus acts as a supplementary volume term to the QBC prescribed over the RVE. In order to remove the spurious effects that occur for non-zero homogenised strain-gradient properties on RVEs of homogeneous Cauchy material, a correction to the asymptotic analysis combined with the finite element method was proposed in [32]. The correction was also introduced in the asymptotic analysis in [33] and when extracting the effective higher-order properties from finite element computations in [21]. In the presented method, the correction term arises from the equivalence of energy, i.e. the Hill-Mandel condition, between the micro- and macroscopic volumes.

The macroscopic media obtained from the presented computational homogenisation is second-order continuum in general. This second-order continuum is resolved with $\mathcal{C}^0$ FEM, by considering the enriched discontinuous Galerkin method (EDG) [38], which weakly enforced the $\mathcal{C}^1$-continuity. The macro-scale constitutive law results from the resolution of the body-force enhanced meso-scale boundary value problem. Nevertheless, the effective high order properties can be extracted from the derivatives of the high order stress with respect to the high order strain to be compared to the values found in the literature [21] in the case of an infinitesimal strain setting.

The outline of the paper is as follows. In Section 2, the key ingredients of the second-order computational homogenisation are recalled in terms of the kinematic fields definition and scale transition formulation. The concept of second-order computational homogenisation based on the equivalent homogenised volume formulated in a finite-strain setting in Section 3. From this equivalence, a non-uniform body force that acts as a supplementary volume term over the RVE arises from the Hill-Mandel condition. The resolution of the resulting multi-scale problem is detailed in Section 4, in which the macro-scale high order continuum is discretised using an enriched discontinuous Galerkin approach. Finally, in Section 5, we first study the second-order homogenised response of elastic RVEs and compare the predictions with the method suggested

in [21] in which the body force is uniform. The change of patterning of a metamaterial RVE is then studied with the presented method and when considering a uniform, but not constant, body force. We eventually conduct second-order FE^2 multi-scale analyses of beam bending, honeycomb structure compression and metamaterials structure compression in the context of linear elasticity, non-linear elasto-plasticity and non-linear elasticity.

2. The kinematic field

2.1. Microscopic kinematic field

In a Representative Volume Element (RVE), the micro-scale material point is denoted by $\boldsymbol{X}_\mathrm{m}$ and its position in the deformed state by $\boldsymbol{x}_\mathrm{m}$, whilst the mapping ϕ_m defines the relation $\boldsymbol{x}_\mathrm{m} = \phi_\mathrm{m}(\boldsymbol{X}_\mathrm{m})$. The microscopic kinematic field can be expressed by truncating the Taylor series expansion at the second-order term, and reads

$$\boldsymbol{x}_\mathrm{m} \;=\; \boldsymbol{F}_\mathrm{M} \cdot \boldsymbol{X}_\mathrm{m} + \frac{1}{2}\mathbf{G}_\mathrm{M} : (\boldsymbol{X}_\mathrm{m} \otimes \boldsymbol{X}_\mathrm{m}) + \boldsymbol{w}(\boldsymbol{X}_\mathrm{m}), \quad \forall \boldsymbol{X}_\mathrm{m} \in \Omega_{\mathrm{m}0}, \tag{1}$$

where $\Omega_{\mathrm{m}0}$ refers to the reference configuration of the RVE domain (potential voids included). In this equation, the macro deformation gradient tensor, $\boldsymbol{F}_\mathrm{M}(\boldsymbol{X}_\mathrm{M})$ and its gradient $\mathbf{G}_\mathrm{M}(\boldsymbol{X}_\mathrm{M}) = \boldsymbol{F}_\mathrm{M} \otimes \nabla_{\mathrm{M}0}$ take the values at the macro-scale material point $\boldsymbol{X}_\mathrm{M}$, which serves as the microscopic coordinate origin of the RVE $\Omega_{\mathrm{m}0}(\boldsymbol{X}_\mathrm{M})$, and $\boldsymbol{w}(\boldsymbol{X}_\mathrm{m})$ is the fluctuation field of zero-average on the RVE $\Omega_{\mathrm{m}0}(\boldsymbol{X}_\mathrm{M})$. Thus the microscopic deformation gradient $\boldsymbol{F}_\mathrm{m}$ in the RVE reads

$$\boldsymbol{F}_\mathrm{m}(\boldsymbol{X}_\mathrm{m}) \;=\; \boldsymbol{F}_\mathrm{M} + \mathbf{G}_\mathrm{M} \cdot \boldsymbol{X}_\mathrm{m} + \boldsymbol{w}(\boldsymbol{X}_\mathrm{m}) \otimes \nabla_{\mathrm{m}0}, \quad \forall \boldsymbol{X}_\mathrm{m} \in \Omega_{\mathrm{m}0}, \tag{2}$$

where $\mathbf{G}_\mathrm{M} = \mathbf{G}_\mathrm{M}^{\mathrm{T}_{2,3}}$ with $\bullet^{\mathrm{T}_{I,J}}$ referring to the permutation of indices I and J, e.g. $a_{iJK}^{\mathrm{T}_{2,3}} = a_{iKJ}$.

2.2. Scale transition

The kinematic variables at the macroscopic material point $\boldsymbol{X}_\mathrm{M}$ are associated to the ones at the microscopic scale through their volume-averages on the RVE $\Omega_{\mathrm{m}0}(\boldsymbol{X}_\mathrm{M})$. In particular

- The most commonly used kinematic averaging relation requires that the volume-average of the microscopic deformation gradient tensor $\boldsymbol{F}_\mathrm{m}(\boldsymbol{X}_\mathrm{m})$ equals the macroscopic deformation gradient tensor $\boldsymbol{F}_\mathrm{M}$, yielding

$$\frac{1}{V_{\mathrm{m}0}} \int_{\Omega_{\mathrm{m}0}} \boldsymbol{F}_\mathrm{m} \mathrm{d}\Omega = \boldsymbol{F}_\mathrm{M}, \tag{3}$$

where $V_{\mathrm{m}0} = \int_{\Omega_{\mathrm{m}0}} \mathrm{d}\Omega$. Using the expression of $\boldsymbol{F}_\mathrm{m}$ obtained in Eq. (2), Eq. (3) can be simplified by setting the micro Cartesian coordinates origin at the geometric centre of the undeformed RVE, in which case, the volume integral of the second term of the right hand side of Eq. (2) vanishes, yielding a condition on the fluctuation field $\boldsymbol{w}(\boldsymbol{X}_\mathrm{m})$, which needs to satisfy

$$\frac{1}{V_{\mathrm{m}0}} \int_{\Omega_{\mathrm{m}0}} \boldsymbol{w} \otimes \nabla_{\mathrm{m}0} \mathrm{d}\Omega = \frac{1}{V_{\mathrm{m}0}} \int_{\Gamma_{\mathrm{m}0}} \boldsymbol{w} \otimes \boldsymbol{N}_{\mathrm{m}0} \mathrm{d}\Gamma = \boldsymbol{0}, \tag{4}$$

where the divergence theorem has been used to transform the integral over the undeformed volume $\Omega_{\mathrm{m}0}$ to its boundary $\Gamma_{\mathrm{m}0}$ of unit outward normal, in the reference configuration, $\boldsymbol{N}_{\mathrm{m}0}$.

- In order to avoid constraining high order boundary conditions on the RVE, the volume-average expression, such as Eq. (3), is not applied on the micro-scale gradient of the deformation gradient $\mathbf{G}_\mathrm{m}(\boldsymbol{X}_\mathrm{m})$. Instead, considering the volume-average of the product between Eq. (2) and $\boldsymbol{X}_\mathrm{m}$ was proposed in [36], yielding the condition, see Appendix A,

$$\int_{\Gamma_{\mathrm{m}0}} [\boldsymbol{w} \otimes \boldsymbol{N}_{\mathrm{m}0} \otimes \boldsymbol{X}_\mathrm{m} + \boldsymbol{w} \otimes \boldsymbol{X}_\mathrm{m} \otimes \boldsymbol{N}_{\mathrm{m}0}] \mathrm{d}\Gamma = \boldsymbol{0}. \tag{5}$$

The boundary conditions on the RVE are now defined. According to Eq. (1), the displacement field in the RVE reads,

$$\boldsymbol{u}_\mathrm{m}(\boldsymbol{X}_\mathrm{m}) = (\boldsymbol{F}_\mathrm{M} - \mathbf{I}) \cdot \boldsymbol{X}_\mathrm{m} + \frac{1}{2}\mathbf{G}_\mathrm{M} : (\boldsymbol{X}_\mathrm{m} \otimes \boldsymbol{X}_\mathrm{m}) + \boldsymbol{w}(\boldsymbol{X}_\mathrm{m}) , \quad \forall \boldsymbol{X}_\mathrm{m} \in \Omega_{\mathrm{m}0} , \tag{6}$$

where $\mathbf{I}$ is second-order identity tensor. Eq. (6) forms a quadratic displacement field at the boundary of the RVE, i.e. $\forall \boldsymbol{X}_\mathrm{m} \in \Gamma_{\mathrm{m}0}$. The constraints of the fluctuation field $\boldsymbol{w}(\boldsymbol{X}_\mathrm{m})$, Eqs. (4) and (5), define the minimum kinematic field

$$\mathcal{U}^\mathrm{min} = \{\boldsymbol{w}(\boldsymbol{X}_\mathrm{m}) | \text{Eqs. (4) and (5) are satisfied}\} , \tag{7}$$

and are applied at the boundary of the RVE by selected appropriate boundary conditions such that $\boldsymbol{w} \in \mathcal{U} \subset \mathcal{U}^\mathrm{min}$, with $\mathcal{U}$ depending on the selected boundary conditions kind, e.g. periodic boundary conditions with zero-average fluctuation on the RVE boundary automatically fulfil Eq. (7).

3. Computational homogenisation based on equivalent volumes
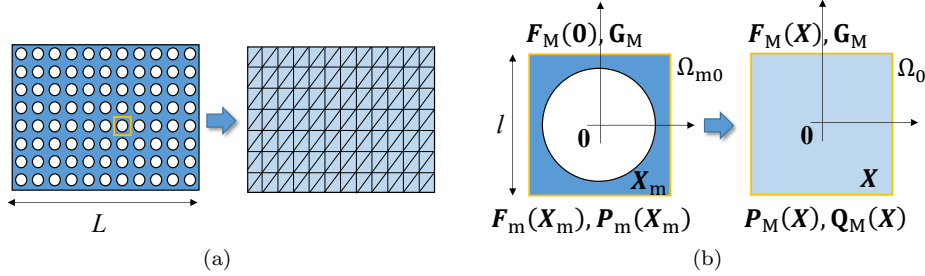

Figure 2: Methodology description: (a) Architectured material and its macroscopic FE discretisation; (b) From unit cell to homogenised volume element.

In a multi-scale analysis of structures made of architectured materials, the meso-scale RVE or unit cell can have a comparable size to that of the macroscopic elements, see Fig. 2(a). Since the RVE has a length scale of the order of the macroscopic elements, the idea of equivalent homogenised volume, see Fig. 2(b), is used to develop a new second-order computational homogenisation process. In a RVE or unit cell, the microscopic material model follows a Cauchy continuum, and the material model in the corresponding macroscopic volume obeys to a second-order continuum. The volumes at both the micro- and macro-scales are equivalent in a volume-averaged sense.

3.1. RVE with Cauchy continuum material

Following a Cauchy continuum, the balance of linear momentum in the RVE implies

$$\boldsymbol{b}_\mathrm{m}(\boldsymbol{X}_\mathrm{m}) + \boldsymbol{P}_\mathrm{m}(\boldsymbol{X}_\mathrm{m}) \cdot \nabla_{\mathrm{m}0} = \boldsymbol{0} , \quad \forall \boldsymbol{X}_\mathrm{m} \in \Omega_{\mathrm{m}0} , \tag{8}$$

where $\boldsymbol{b}_\mathrm{m}(\boldsymbol{X}_\mathrm{m})$ is an applied body force on the RVE, and the first Piola-Kirchhoff stress, $\boldsymbol{P}_\mathrm{m}(\boldsymbol{X}_\mathrm{m})$, is evaluated from the microscopic deformation gradient $\boldsymbol{F}_\mathrm{m}(\boldsymbol{X}_\mathrm{m})$ following the local constitutive law

$$\boldsymbol{P}_\mathrm{m}(\boldsymbol{X}_\mathrm{m}, t) = \boldsymbol{P}_\mathrm{m}(\boldsymbol{F}_\mathrm{m}(\boldsymbol{X}_\mathrm{m}, t); \boldsymbol{Z}_\mathrm{m}(\boldsymbol{X}_\mathrm{m}, \tau), \tau \in [0, t]) , \tag{9}$$

where $\boldsymbol{Z}_\mathrm{m}$ is a set of state variables tracking history-dependent processes. Note that in the voided parts of $\Omega_{\mathrm{m}0}$ the stress tensor vanishes.

Besides, the RVE is subjected to proper boundary conditions which satisfy the relations of equivalence of the kinematic variables at the two scales, see Eqs. (4) and (5). The detailed definition of the boundary conditions will be given in Section 4.

3.2. Homogenised material

Although a Cauchy continuum is considered for the microscopic material model, a second-order continuum is required to describe the homogeneous macroscopic material because of its inner structure at the lower scale. In that context, a constant gradient of deformation gradient, $\mathbf{G}_\mathrm{M}$, is imposed on the second-order continuum volume element, Ω_0, see Fig. 2(b). Following a Taylor expansion, the deformation gradient, $\boldsymbol{F}_\mathrm{M}$, first Piola-Kirchhoff stress, $\boldsymbol{P}_\mathrm{M}$, and high order stress, $\mathbf{Q}_\mathrm{M}$, are expressed as

$$
\begin{align}
\boldsymbol{F}_\mathrm{M}(\boldsymbol{X}) &= \boldsymbol{F}_\mathrm{M}(\mathbf{0}) + \mathbf{G}_\mathrm{M} \cdot \boldsymbol{X}\,, \tag{10}\\
\boldsymbol{P}_\mathrm{M}(\boldsymbol{X}) &= \boldsymbol{P}_\mathrm{M}(\mathbf{0}) + \left.\frac{\partial \boldsymbol{P}_\mathrm{M}}{\partial \boldsymbol{F}_\mathrm{M}}\right|_{\boldsymbol{X}=\mathbf{0}} : \mathbf{G}_\mathrm{M} \cdot \boldsymbol{X}\,, \tag{11}\\
\mathbf{Q}_\mathrm{M}(\boldsymbol{X}) &= \mathbf{Q}_\mathrm{M}(\mathbf{0}) + \left.\frac{\partial \mathbf{Q}_\mathrm{M}}{\partial \boldsymbol{F}_\mathrm{M}}\right|_{\boldsymbol{X}=\mathbf{0}} : \mathbf{G}_\mathrm{M} \cdot \boldsymbol{X}\,, \tag{12}
\end{align}
$$

where the subscript "$\bullet_\mathrm{M}$" is used to indicate the homogenised macroscopic medium, and where $\boldsymbol{X} \in \Omega_0$ refers to the points of the second-order continuum volume element. The geometric centre of the second-order continuum volume element Ω_0 is chosen as the origin of the local coordinates. Hence, the volume-average of Eqs. (10-12) yields,

$$
\begin{align}
\frac{1}{V_0} \int_{\Omega_0} \boldsymbol{F}_\mathrm{M}(\boldsymbol{X}) \mathrm{d}\Omega &= \boldsymbol{F}_\mathrm{M}(\mathbf{0}) = \boldsymbol{F}_\mathrm{M}^0\,, \tag{13}\\
\frac{1}{V_0} \int_{\Omega_0} \boldsymbol{P}_\mathrm{M}(\boldsymbol{X}) \mathrm{d}\Omega &= \boldsymbol{P}_\mathrm{M}(\mathbf{0}) = \boldsymbol{P}_\mathrm{M}^0\,, \tag{14}\\
\frac{1}{V_0} \int_{\Omega_0} \mathbf{Q}_\mathrm{M}(\boldsymbol{X}) \mathrm{d}\Omega &= \mathbf{Q}_\mathrm{M}(\mathbf{0}) = \mathbf{Q}_\mathrm{M}^0\,, \tag{15}
\end{align}
$$

where "$\bullet^0$" denotes the value of a variable at the origin of the local coordinates, "$\bullet_0$" refers to the reference configuration, and $V_0 = \int_{\Omega_0} \mathrm{d}\Omega$.

The momentum balance equation of a second-order continuum can be derived from the principle of virtual work [5, 36, 39], and reads

$$
\boldsymbol{B}_\mathrm{M}(\boldsymbol{X}) + [\boldsymbol{P}_\mathrm{M}(\boldsymbol{X}) - \mathbf{Q}_\mathrm{M}(\boldsymbol{X}) \cdot \nabla_0] \cdot \nabla_0 = \mathbf{0}\,, \quad \forall \boldsymbol{X} \in \Omega_0\,, \tag{16}
$$

where $\boldsymbol{B}_\mathrm{M}(\boldsymbol{X})$ is the macroscopic body force. Substituting $\boldsymbol{P}_\mathrm{M}(\boldsymbol{X})$ and $\mathbf{Q}_\mathrm{M}(\boldsymbol{X})$ by their expressions given in Eqs. (11-12) allows rewriting Eq. (16) as

$$
\begin{align}
\boldsymbol{B}_\mathrm{M}(\boldsymbol{X}) + \left[\boldsymbol{P}_\mathrm{M}^0 + \frac{\partial \boldsymbol{P}_\mathrm{M}^0}{\partial \boldsymbol{F}_\mathrm{M}^0} : \mathbf{G}_\mathrm{M} \cdot \boldsymbol{X} - \left(\mathbf{Q}_\mathrm{M}^0 + \frac{\partial \mathbf{Q}_\mathrm{M}^0}{\partial \boldsymbol{F}_\mathrm{M}^0} : \mathbf{G}_\mathrm{M} \cdot \boldsymbol{X}\right) \cdot \nabla_0\right] \cdot \nabla_0 & \notag\\
= \boldsymbol{B}_\mathrm{M}(\boldsymbol{X}) + \left(\frac{\partial \boldsymbol{P}_\mathrm{M}^0}{\partial \boldsymbol{F}_\mathrm{M}^0} : \mathbf{G}_\mathrm{M}\right) : \mathbf{I} = \mathbf{0}\,. \tag{17}
\end{align}
$$

The balance of momentum indicates that a constant body force $\boldsymbol{B}_\mathrm{M}$ must be applied if we want to constrain a constant $\mathbf{G}_\mathrm{M}$ on the homogeneous volume Ω_0. As a result a corresponding body force $\boldsymbol{b}_\mathrm{m}$ should also be applied on the microscopic volume element $\Omega_{\mathrm{m}0}$.

3.3. Energy equivalence between the microscopic volume element and the homogeneous volume

Considering the variations of $\boldsymbol{F}_\mathrm{M}$ and $\mathbf{G}_\mathrm{M}$ (and $\mathbf{G}_\mathrm{M}^{\mathrm{T}_{2,3}}$), the equivalence of energy, or Hill-Mandel condition, between the microscopic volume element $\Omega_{\mathrm{m}0}$ and the macroscopic homogeneous volume Ω_0 reads

$$
\int_{\Omega_{\mathrm{m}0}} [\boldsymbol{P}_\mathrm{m} : \delta\boldsymbol{F}_\mathrm{m} - \boldsymbol{b}_\mathrm{m} \cdot \delta\boldsymbol{u}_\mathrm{m}] \,\mathrm{d}\Omega = \int_{\Omega_0} \left[\boldsymbol{P}_\mathrm{M} : \delta\boldsymbol{F}_\mathrm{M} + \mathbf{Q}_\mathrm{M} \vdots \delta\mathbf{G}_\mathrm{M} - \boldsymbol{B}_\mathrm{M} \cdot \delta\boldsymbol{u}_\mathrm{M}\right] \mathrm{d}\Omega\,. \tag{18}
$$

7

Using the expressions of $\boldsymbol{F}_{\mathrm{m}}$, Eq. (2), and of $\boldsymbol{u}_{\mathrm{m}} = \boldsymbol{x}_{\mathrm{m}} - \boldsymbol{X}_{\mathrm{m}}$ from Eq. (1), and since the applied macro-scale gradient on the microscopic volume element Ω_{m0} corresponds to $\boldsymbol{F}_{\mathrm{M}}^0$, the left hand side of Eq. (18) becomes

$$
\int_{\Omega_{\mathrm{m0}}} [\boldsymbol{P}_{\mathrm{m}} : \delta\boldsymbol{F}_{\mathrm{m}} - \boldsymbol{b}_{\mathrm{m}} \cdot \delta\boldsymbol{u}_{\mathrm{m}}]\,\mathrm{d}\Omega = \int_{\Omega_{\mathrm{m0}}} \boldsymbol{P}_{\mathrm{m}} : \delta\boldsymbol{F}_{\mathrm{M}}^0\mathrm{d}\Omega +
$$
$$
\int_{\Omega_{\mathrm{m0}}} \left\{ \frac{1}{2} \left[\boldsymbol{P}_{\mathrm{m}} \otimes \boldsymbol{X}_{\mathrm{m}} + (\boldsymbol{P}_{\mathrm{m}} \otimes \boldsymbol{X}_{\mathrm{m}})^{\mathrm{T}_{2,3}} \right] \vdots \delta\mathbf{G}_{\mathrm{M}} + \boldsymbol{P}_{\mathrm{m}} : (\delta\boldsymbol{w} \otimes \nabla_{\mathrm{m0}}) \right\} \mathrm{d}\Omega
$$
$$
- \int_{\Omega_{\mathrm{m0}}} \left\{ (\boldsymbol{b}_{\mathrm{m}} \otimes \boldsymbol{X}_{\mathrm{m}}) : \delta\boldsymbol{F}_{\mathrm{M}}^0 + \frac{1}{2} (\boldsymbol{b}_{\mathrm{m}} \otimes \boldsymbol{X}_{\mathrm{m}} \otimes \boldsymbol{X}_{\mathrm{m}}) \vdots \delta\mathbf{G}_{\mathrm{M}} + \boldsymbol{b}_{\mathrm{m}} \cdot \delta\boldsymbol{\omega} \right\} d\Omega.
$$
(19)

For the homogeneous volume Ω_0, the right hand side of Eq. (18) can be extended by using the expressions in Eqs.(10-12) and reads

$$
\int_{\Omega_0} \left[\boldsymbol{P}_{\mathrm{M}} : \delta\boldsymbol{F}_{\mathrm{M}} + \mathbf{Q}_{\mathrm{M}} \vdots \delta\mathbf{G}_{\mathrm{M}} - \boldsymbol{B}_{\mathrm{M}} \cdot \delta\boldsymbol{u}_{\mathrm{M}} \right] \mathrm{d}\Omega = V_0(\boldsymbol{P}_{\mathrm{M}}^0 : \delta\boldsymbol{F}_{\mathrm{M}}^0 + \mathbf{Q}_{\mathrm{M}}^0 \vdots \delta\mathbf{G}_{\mathrm{M}}) +
$$
$$
\int_{\Omega_0} \frac{1}{2} \left\{ \frac{\partial \boldsymbol{P}_{\mathrm{M}}^0}{\partial \boldsymbol{F}_{\mathrm{M}}^0} : \mathbf{G}_{\mathrm{M}} \cdot \boldsymbol{X} \otimes \boldsymbol{X} + \left(\frac{\partial \boldsymbol{P}_{\mathrm{M}}^0}{\partial \boldsymbol{F}_{\mathrm{M}}^0} : \mathbf{G}_{\mathrm{M}} \cdot \boldsymbol{X} \otimes \boldsymbol{X} \right)^{\mathrm{T}_{2,3}} \right\} \mathrm{d}\Omega \vdots \delta\mathbf{G}_{\mathrm{M}}
$$
$$
- \int_{\Omega_0} \left\{ (\boldsymbol{B}_{\mathrm{M}} \otimes \boldsymbol{X}) : \delta\boldsymbol{F}_{\mathrm{M}}^0 + \frac{1}{2} (\boldsymbol{B}_{\mathrm{M}} \otimes \boldsymbol{X} \otimes \boldsymbol{X}) \vdots \delta\mathbf{G}_{\mathrm{M}} \right\} d\Omega,
$$
(20)

because the geometric centre of the macroscopic volume serves as the origin of the local coordinates. Since $\delta\boldsymbol{F}_{\mathrm{M}}^0$ and $\delta\mathbf{G}_{\mathrm{M}}$ are arbitrary, by comparing Eq. (19) to Eq. (20), Eq. (18) yields the following equations,

$$
\int_{\Omega_{\mathrm{m0}}} \boldsymbol{P}_{\mathrm{m}}\mathrm{d}\Omega - \int_{\Omega_{\mathrm{m0}}} \boldsymbol{b}_{\mathrm{m}} \otimes \boldsymbol{X}_{\mathrm{m}}\mathrm{d}\Omega = V_0\boldsymbol{P}_{\mathrm{M}}^0 - \int_{\Omega_0} \boldsymbol{B}_{\mathrm{M}} \otimes \boldsymbol{X}\mathrm{d}\Omega,
$$
(21)

$$
\frac{1}{2} \int_{\Omega_{\mathrm{m0}}} \left[\boldsymbol{P}_{\mathrm{m}} \otimes \boldsymbol{X}_{\mathrm{m}} + (\boldsymbol{P}_{\mathrm{m}} \otimes \boldsymbol{X}_{\mathrm{m}})^{\mathrm{T}_{2,3}} \right] \mathrm{d}\Omega - \frac{1}{2} \int_{\Omega_{\mathrm{m0}}} \boldsymbol{b}_{\mathrm{m}} \otimes \boldsymbol{X}_{\mathrm{m}} \otimes \boldsymbol{X}_{\mathrm{m}}\mathrm{d}\Omega =
$$
$$
V_0\mathbf{Q}_{\mathrm{M}}^0 + \frac{1}{2} \left\{ \frac{\partial \boldsymbol{P}_{\mathrm{M}}^0}{\partial \boldsymbol{F}_{\mathrm{M}}^0} : \mathbf{G}_{\mathrm{M}} \cdot \boldsymbol{J}_{\mathrm{M}} + \left(\frac{\partial \boldsymbol{P}_{\mathrm{M}}^0}{\partial \boldsymbol{F}_{\mathrm{M}}^0} : \mathbf{G}_{\mathrm{M}} \cdot \boldsymbol{J}_{\mathrm{M}} \right)^{\mathrm{T}_{2,3}} \right\} - \frac{1}{2}\boldsymbol{B}_{\mathrm{M}} \otimes \boldsymbol{J}_{\mathrm{M}},
$$
(22)

where $\boldsymbol{J}_{\mathrm{M}} = \int_{\Omega_0} \boldsymbol{X} \otimes \boldsymbol{X}\mathrm{d}\Omega$ is the geometric inertia of the homogeneous volume. Finally, the remaining terms of Eq. (19) lead to the equation

$$
\int_{\Omega_{\mathrm{m0}}} [\boldsymbol{P}_{\mathrm{m}} : (\delta\boldsymbol{w} \otimes \nabla_{\mathrm{m0}}) - \boldsymbol{b}_{\mathrm{m}} \cdot \delta\boldsymbol{w}]\,\mathrm{d}\Omega = 0,
$$
(23)

which is the weak form that needs to be solved on the RVE Ω_{m0}.

3.4. Macroscopic stress and high order stress

For a macroscopic material point which locates at the origin of local coordinates of the homogeneous volume Ω_0, its stress and high order stress can be computed from Eqs. (21) and (22), and respectively read

$$\boldsymbol{P}_{\mathrm{M}}^0 = \frac{1}{V_0}\left(\int_{\Omega_{\mathrm{m}0}} \boldsymbol{P}_{\mathrm{m}}\mathrm{d}\Omega - \int_{\Omega_{\mathrm{m}0}} \boldsymbol{b}_{\mathrm{m}}\otimes\boldsymbol{X}_{\mathrm{m}}\mathrm{d}\Omega\right), \tag{24}$$

$$\begin{aligned}
\mathbf{Q}_{\mathrm{M}}^0 = {}& \frac{1}{2V_0}\int_{\Omega_{\mathrm{m}0}}\left[\boldsymbol{P}_{\mathrm{m}}\otimes\boldsymbol{X}_{\mathrm{m}} + (\boldsymbol{P}_{\mathrm{m}}\otimes\boldsymbol{X}_{\mathrm{m}})^{\mathrm{T}_{2,3}}\right]\mathrm{d}\Omega - \\
& \frac{1}{2V_0}\int_{\Omega_{\mathrm{m}0}}\boldsymbol{b}_{\mathrm{m}}\otimes\boldsymbol{X}_{\mathrm{m}}\otimes\boldsymbol{X}_{\mathrm{m}}\mathrm{d}\Omega - \\
& \frac{1}{2V_0}\left(\left[\frac{\partial\boldsymbol{P}_{\mathrm{M}}^0}{\partial\boldsymbol{F}_{\mathrm{M}}^0}:\mathbf{G}_{\mathrm{M}}\cdot\boldsymbol{J}_{\mathrm{M}} + \left(\frac{\partial\boldsymbol{P}_{\mathrm{M}}^0}{\partial\boldsymbol{F}_{\mathrm{M}}^0}:\mathbf{G}_{\mathrm{M}}\cdot\boldsymbol{J}_{\mathrm{M}}\right)^{\mathrm{T}_{2,3}}\right] - \boldsymbol{B}_{\mathrm{M}}\otimes\boldsymbol{J}_{\mathrm{M}}\right),
\end{aligned} \tag{25}$$

where the macroscopic body force, $\boldsymbol{B}_{\mathrm{M}}$, is assumed to be constant on the homogeneous volume element, yielding $\int_{\Omega_0}\boldsymbol{B}_{\mathrm{M}}\otimes\boldsymbol{X}\mathrm{d}\Omega = \boldsymbol{0}$ when the geometric centre of the homogeneous volume is used as the origin of local coordinates. Compared to the second-order computational homogenisation established in [36], new terms arise in the expressions of macroscopic stress, Eq. (24), and high order stress, Eq. (25).

Remark 1. We consider that the homogeneous volume element Ω_0 and the micro-volume element $\Omega_{\mathrm{m}0}$ share the same spatial locations, yielding $V_0 = V_{\mathrm{m}0}$ and $\boldsymbol{J}_{\mathrm{M}} = \boldsymbol{J}_{\mathrm{m}}$, where the geometric inertia $\boldsymbol{J}_{\mathrm{m}} = \int_{\Omega_{\mathrm{m}0}}\boldsymbol{X}_{\mathrm{m}}\otimes\boldsymbol{X}_{\mathrm{m}}\mathrm{d}\Omega$[1].

Remark 2. A homogeneous volume can always withstand high order stresses, such as bending moment and torque, even if it is made of a Cauchy continuum. The third term at the right hand side of Eq. (25) comes naturally from the equivalence of the micro- and homogeneous volumes, and this corresponds to a correction introduced to remove the spurious higher-order properties of homogeneous Cauchy continuum [21, 32, 33].

Remark 3. In both Eqs. (24) and (25), there are extra terms related to the body forces. These terms are similar to that obtained in [24], in which the effect of body forces and inertia phenomena occurring at the micro-scale was accounted for in a second-order computational homogenisation. Nevertheless, these terms have other physical interpretations in this work and they will be discussed after the expression of the body force $\boldsymbol{b}_{\mathrm{m}}$ is introduced.

3.5. Macro- and microscopic body forces $\boldsymbol{B}_M$ and $\boldsymbol{b}_m$

Since the idea of equivalent volume was adopted in the presented computational homogenisation, Eq. (17) yields a constant body force $\boldsymbol{B}_{\mathrm{M}}$, which is applied to constrain the constant macro-scale gradient of deformation gradient $\mathbf{G}_{\mathrm{M}}$ on the equivalent homogeneous volume, Ω_0. Thus a corresponding body force, $\boldsymbol{b}_{\mathrm{m}}$, is needed on the micro-volume element $\Omega_{\mathrm{m}0}$. We propose an equivalence relation for the supplementary body force which reads,

$$\int_{\Omega_{\mathrm{m}0}}\boldsymbol{b}_{\mathrm{m}}(\boldsymbol{X}_{\mathrm{m}})\mathrm{d}\Omega = \int_{\Omega_0}\boldsymbol{B}_{\mathrm{M}}\mathrm{d}\Omega = V_0\boldsymbol{B}_{\mathrm{M}}. \tag{27}$$

The simplest choice is to assume a constant $\boldsymbol{b}_{\mathrm{m}} = \boldsymbol{B}_{\mathrm{M}}$. This assumption has been used by Yvonnet et al. [21]. However, in the case of microscopic volumes consisting of porous and/or lattice structures, in which $\int_{\Omega_{\mathrm{m}0}}\boldsymbol{b}_{\mathrm{m}}\mathrm{d}\Omega \neq \int_{\Omega_0}\boldsymbol{B}_{\mathrm{M}}\mathrm{d}\Omega$, the equivalence of total body force, Eq. (27), will not be satisfied. In the equivalent homogeneous volume Ω_0, according to Eq. (17), the supplementary constrained body force reads,

$$\boldsymbol{B}_{\mathrm{M}} = -\left(\frac{\partial\boldsymbol{P}_{\mathrm{M}}^0}{\partial\boldsymbol{F}_{\mathrm{M}}^0}:\mathbf{G}_{\mathrm{M}}\right):\mathbf{I}, \tag{28}$$

---

[1]For a parallelepiped RVE, it reads

$$\boldsymbol{J}_{\mathrm{m}} = \int_{\Omega_{\mathrm{m}0}}\boldsymbol{X}_{\mathrm{m}}\otimes\boldsymbol{X}_{\mathrm{m}}\mathrm{d}\Omega = \frac{V_{\mathrm{m}0}}{12}(l_1^2\boldsymbol{e}_1\otimes\boldsymbol{e}_1 + l_2^2\boldsymbol{e}_2\otimes\boldsymbol{e}_2 + l_3^2\boldsymbol{e}_3\otimes\boldsymbol{e}_3), \tag{26}$$

where l_1, l_2 and l_3 are respectively the lengths of the three sides of the RVE, and the volume of the RVE $V_{\mathrm{m}0} = l_1 l_2 l_3$.

where $\frac{\partial \boldsymbol{P}_{\mathrm{M}}^0}{\partial \boldsymbol{F}_{\mathrm{M}}^0}$ is the macroscopic homogenised first-order material tensor. It can be approximated by neglecting the body forces contributions in Eq. (24), i.e. by considering the definition of the homogenised stress in a first order homogenisation scheme: $\boldsymbol{P}_{\mathrm{M}}^0 = \frac{1}{V_0} \int_{\Omega_{\mathrm{m0}}} \boldsymbol{P}_{\mathrm{m}} \mathrm{d}\Omega$, to simplify the problem. Thus, Eq. (28) is further extended as,

$$
\begin{aligned}
\boldsymbol{B}_{\mathrm{M}} &= -\frac{1}{V_0} \left[\frac{\partial}{\partial \boldsymbol{F}_{\mathrm{M}}^0} \left(\int_{\Omega_{\mathrm{m0}}} \boldsymbol{P}_{\mathrm{m}} \mathrm{d}\Omega \right) : \mathbf{G}_{\mathrm{M}} \right] : \mathbf{I} \\
&= -\frac{1}{V_0} \left[\int_{\Omega_{\mathrm{m0}}} \frac{\partial \boldsymbol{P}_{\mathrm{m}}}{\partial \boldsymbol{F}_{\mathrm{m}}} : \frac{\partial \boldsymbol{F}_{\mathrm{m}}}{\partial \boldsymbol{F}_{\mathrm{M}}^0} \mathrm{d}\Omega : \mathbf{G}_{\mathrm{M}} \right] : \mathbf{I} .
\end{aligned}
\tag{29}
$$

Comparing this expression to Eq. (27), a microscopic body force can be defined as

$$
\boldsymbol{b}_{\mathrm{m}} = - \left(\frac{\partial \boldsymbol{P}_{\mathrm{m}}}{\partial \boldsymbol{F}_{\mathrm{m}}} : \frac{\partial \boldsymbol{F}_{\mathrm{m}}}{\partial \boldsymbol{F}_{\mathrm{M}}^0} : \mathbf{G}_{\mathrm{M}} \right) : \mathbf{I} ,
\tag{30}
$$

where $\frac{\partial \boldsymbol{P}_{\mathrm{m}}}{\partial \boldsymbol{F}_{\mathrm{m}}}$ is the microscopic local tangent operator in the RVE, and where the term $\frac{\partial \boldsymbol{F}_{\mathrm{m}}}{\partial \boldsymbol{F}_{\mathrm{M}}^0}$, which corresponds to the strain concentration tensor, needs to be extracted from the resolution of the RVE as discussed in Section 4. Note that in the voided parts of Ω_{m0}, one has $\frac{\partial \boldsymbol{P}_{\mathrm{m}}}{\partial \boldsymbol{F}_{\mathrm{m}}} : \frac{\partial \boldsymbol{F}_{\mathrm{m}}}{\partial \boldsymbol{F}_{\mathrm{M}}^0} = 0$ since the stress tensor vanishes.

Remark 4. For a RVE of heterogeneous or architectured materials, its geometric centre may be different from its shear centre, in which case, a twisting occurs due to the applied body forces. This effect corresponds to the term $\int_{\Omega_{\mathrm{m0}}} \boldsymbol{b}_{\mathrm{m}} \otimes \boldsymbol{X}_{\mathrm{m}} \mathrm{d}\Omega$ in Eq. (24). Since the body force is non-zero when a strain gradient $\mathbf{G}_{\mathrm{M}}$ is applied, this term represents the effect of the strain gradient on the macroscopic stress. More precisely, it is related to the homogenised fifth-order material tensor, $\frac{\partial \boldsymbol{P}_{\mathrm{M}}}{\partial \mathbf{G}_{\mathrm{M}}}$. This term will not vanish for non-centro-symmetric RVEs, which is consistent with the experimental observations on non-centro-symmetric lattices [40].

Remark 5. According to the expressions of body forces in Eqs. (28) and (30), the two terms $\int_{\Omega_{\mathrm{m0}}} \boldsymbol{b}_{\mathrm{m}} \otimes \boldsymbol{X}_{\mathrm{m}} \otimes \boldsymbol{X}_{\mathrm{m}} \mathrm{d}\Omega$ and $\boldsymbol{B}_{\mathrm{M}} \otimes \boldsymbol{J}_{\mathrm{M}}$ in Eq. (25) introduce a similar expression than the bending and torsional stiffnesses in beam theory. They thus correspond to the high order stresses arising due to the existence of the strain gradient.

4. Two-scale finite element resolution

From the relations between micro- and macroscopic kinematic fields derived in Section 2, the equivalence of the deformation gradient and its gradient at the two scales requires that the fluctuation field $\boldsymbol{w}(\boldsymbol{X})$ defined in Eq. (6) satisfies the conditions (4) and (5). These equations are satisfied for a fluctuation field belonging to the minimum kinematic field $\mathcal{U}^{\min}$, Eq. (7), i.e. by selected appropriate boundary conditions such that $\boldsymbol{w} \in \mathcal{U} \subset \mathcal{U}^{\min}$, with $\mathcal{U}$ depending on the boundary conditions kind. Here we consider a parallelepiped RVE on which Periodic Boundary Conditions (PBCs) are applied. Although the implementation details of PBCs can be found in the literature, e.g. in [41], in this section, some basic equations are recalled briefly, and then the modifications required to apply the body forces are presented. Since $\boldsymbol{P}_{\mathrm{M}}^0$ and $\boldsymbol{F}_{\mathrm{M}}^0$ are the values, not only at origin of coordinates, but also of the volume-averages on the RVE, the superscript "0" will be omitted for conciseness in this section.

4.1. Definition of the Periodic Boundary Conditions (PBCs)

The boundary of the RVE is separated into positive, Γ_{m0}^+, and negative, Γ_{m0}^-, parts with their normal satisfying $\boldsymbol{N}_{\mathrm{m0}}^- = -\boldsymbol{N}_{\mathrm{m0}}^+$. Then, the condition (4) can be rewritten as

$$
\int_{\Gamma_{\mathrm{m0}}^-} [\boldsymbol{w}^- - \boldsymbol{w}^+] \otimes \boldsymbol{N}_{\mathrm{m0}}^- \mathrm{d}\Gamma = 0 ,
\tag{31}
$$

which is satisfied by constraining $\boldsymbol{w}^- = \boldsymbol{w}^+$ for the displacement fluctuation on the boundaries. By using the expression (6), PBCs immediately lead to the sufficient conditions which are formulated as

$$\boldsymbol{u}_{\mathrm{m}}^+ - \boldsymbol{u}_{\mathrm{m}}^- = (\boldsymbol{F}_{\mathrm{M}} - \mathbf{I}) \cdot \left(\boldsymbol{X}_{\mathrm{m}}^+ - \boldsymbol{X}_{\mathrm{m}}^-\right) + \frac{1}{2}\mathbf{G}_{\mathrm{M}} : \left[\boldsymbol{X}_{\mathrm{m}}^+ \otimes \boldsymbol{X}_{\mathrm{m}}^+ - \boldsymbol{X}_{\mathrm{m}}^- \otimes \boldsymbol{X}_{\mathrm{m}}^-\right] ,$$
$$\forall \boldsymbol{X}_{\mathrm{m}}^\pm \in \Gamma_{\mathrm{m}0} , \tag{32}$$

which can be expressed under the matrix form as

$$\begin{bmatrix} 1 & -1 \end{bmatrix} \begin{bmatrix} \boldsymbol{u}_{\mathrm{m}}^+ \\ \boldsymbol{u}_{\mathrm{m}}^- \end{bmatrix} = \begin{bmatrix} 1 & -1 \end{bmatrix} \begin{bmatrix} \boldsymbol{X}_{\mathrm{m}}^+ & \frac{1}{2}\boldsymbol{X}_{\mathrm{m}}^+ \otimes \boldsymbol{X}_{\mathrm{m}}^+ \\ \boldsymbol{X}_{\mathrm{m}}^- & \frac{1}{2}\boldsymbol{X}_{\mathrm{m}}^- \otimes \boldsymbol{X}_{\mathrm{m}}^- \end{bmatrix} \begin{bmatrix} \boldsymbol{F}_{\mathrm{M}}^{\mathrm{T}} - \mathbf{I} \\ \mathbf{G}_{\mathrm{M}}^{\mathrm{T}} \end{bmatrix} \quad \forall \boldsymbol{X}_{\mathrm{m}}^\pm \in \Gamma_{\mathrm{m}0} , \tag{33}$$

where we define $\left[\mathbf{G}_{\mathrm{M}}^{\mathrm{T}}\right]_{IJk} = [\mathbf{G}_{\mathrm{M}}]_{kIJ}$. Under the assumption of PBCs, the condition (5) simplifies as

$$\int_{\Gamma_{\mathrm{m}0}^-} \boldsymbol{w}\mathrm{d}\Gamma = \mathbf{0} , \tag{34}$$

which leads to

$$\int_{\Gamma_{\mathrm{m}0}^-} \left[\boldsymbol{u}_{\mathrm{m}} - (\boldsymbol{F}_{\mathrm{M}} - \mathbf{I}) \cdot \boldsymbol{X}_{\mathrm{m}} - \frac{1}{2}\mathbf{G}_{\mathrm{M}} : (\boldsymbol{X}_{\mathrm{m}} \otimes \boldsymbol{X}_{\mathrm{m}})\right] \mathrm{d}\Gamma = \mathbf{0} , \tag{35}$$

and which is rewritten under the matrix expression as

$$\begin{bmatrix} \mathbf{0} & \bigwedge_{\Gamma^{\mathrm{e}} \in \Gamma_{\mathrm{m}0}^-} \mathbb{W}\mathbb{N}^{\mathrm{e}} \end{bmatrix} \begin{bmatrix} \boldsymbol{u}_{\mathrm{m}}(\boldsymbol{X}_{\mathrm{m}})|_{\boldsymbol{X}_{\mathrm{m}} \notin \Gamma_{\mathrm{m}0}^-} \\ \boldsymbol{u}_{\mathrm{m}}(\boldsymbol{X}_{\mathrm{m}})|_{\boldsymbol{X}_{\mathrm{m}} \in \Gamma_{\mathrm{m}0}^-} \end{bmatrix} =$$
$$\begin{bmatrix} \int_{\Gamma_{\mathrm{m}0}^-} \boldsymbol{X}_{\mathrm{m}}\mathrm{d}\Gamma & \int_{\Gamma_{\mathrm{m}0}^-} \frac{1}{2} (\boldsymbol{X}_{\mathrm{m}} \otimes \boldsymbol{X}_{\mathrm{m}}) \mathrm{d}\Gamma \end{bmatrix} \begin{bmatrix} \boldsymbol{F}_{\mathrm{M}}^{\mathrm{T}} - \mathbf{I} \\ \mathbf{G}_{\mathrm{M}}^{\mathrm{T}} \end{bmatrix} , \tag{36}$$

where $\bigwedge_{\Gamma^{\mathrm{e}}}$ corresponds to an element assembly process, and where $\mathbb{W}$ and $\mathbb{N}^{\mathrm{e}}$ are respectively the weight function and shape function of the element. The constraints between all the periodic pairs $(\boldsymbol{u}_{\mathrm{m}}^+, \boldsymbol{u}_{\mathrm{m}}^-)$, Eq. (33), and the zero sum of the displacement fluctuation, Eq. (36), can be written together under the matrix form as [22, 41]

$$\mathcal{C}\mathbf{u}_{\mathrm{m}} - \mathcal{S}\mathcal{K}_{\mathrm{M}}^u = \mathbf{0} , \tag{37}$$

where the kinematic vector $\mathcal{K}_{\mathrm{M}}^u$ is the collection of $\boldsymbol{F}_{\mathrm{M}}^{\mathrm{T}} - \mathbf{I}$ and $\mathbf{G}_{\mathrm{M}}^{\mathrm{T}}$ written under a vector form, and where $\mathbf{u}_{\mathrm{m}}$ is the vector of the nodal displacements.

4.2. Iterative resolution

The local equilibrium equation (23) and linear constraints (37) result in a set of non-linear equations, which reads

$$\begin{cases} \mathbf{f}_{\mathrm{m}}\left(\mathbf{u}_{\mathrm{m}}\right) - \mathbf{b}_{\mathrm{m}}\left(\mathbf{u}_{\mathrm{m}}\right) - \mathcal{C}^{\mathrm{T}}\boldsymbol{\lambda} = \mathbf{0} \\ \mathcal{C}\mathbf{u}_{\mathrm{m}} - \mathcal{S}\mathcal{K}_{\mathrm{M}}^u = \mathbf{0} \end{cases} , \tag{38}$$

where $\mathbf{f}_{\mathrm{m}}$ and $\mathbf{b}_{\mathrm{m}}$ are respectively the internal force and body force vectors that both depend on $\mathbf{u}_{\mathrm{m}}$, and $\boldsymbol{\lambda}$ is the Lagrange multipliers vector used to enforce the constraints. This non-linear system (38) needs to be solved iteratively and is thus linearised in terms of the increments of displacements vector, $\delta\boldsymbol{u}_{\mathrm{m}}$, Lagrange multipliers vector, $\delta\boldsymbol{\lambda}$, and macroscopic kinematic vector, $\delta\mathcal{K}_{\mathrm{M}}^u$, yielding

$$\begin{cases} \mathbf{r} + \mathbf{K}_{\mathrm{B}}\delta\mathbf{u}_{\mathrm{m}} - \frac{\partial \mathbf{b}_{\mathrm{m}}}{\partial \mathcal{K}_{\mathrm{M}}^u}\delta\mathcal{K}_{\mathrm{M}}^u - \mathcal{C}^{\mathrm{T}}\delta\boldsymbol{\lambda} = \mathbf{0} , \text{ with } \mathbf{K}_{\mathrm{B}} = \frac{\partial(\mathbf{f}_{\mathrm{m}} - \mathbf{b}_{\mathrm{m}})}{\partial\mathbf{u}_{\mathrm{m}}} \\ \mathbf{r}_{\mathrm{c}} + \mathcal{C}\delta\mathbf{u}_{\mathrm{m}} - \mathcal{S}\delta\mathcal{K}_{\mathrm{M}}^u = \mathbf{0} \end{cases} , \tag{39}$$

where $\mathbf{r}$ and $\mathbf{r}_{\mathrm{c}}$ are force residual and constraints residual vectors of the system (38), respectively. We note that through Eq. (30), the applied body force $\boldsymbol{b}_{\mathrm{m}}$ is related to $\mathcal{K}_{\mathrm{M}}^u$ via the gradient of deformation gradient $\mathbf{G}_{\mathrm{M}}$ (we neglect the dependency in $\boldsymbol{F}_{\mathrm{M}}$ of $\frac{\partial \boldsymbol{P}_{\mathrm{m}}}{\partial \boldsymbol{F}_{\mathrm{m}}} : \frac{\partial \boldsymbol{F}_{\mathrm{m}}}{\partial \boldsymbol{F}_{\mathrm{M}}}$ as discussed in the next Section 4.3). The Lagrange multipliers vector is eliminated using the method presented in [42] resulting in an equivalent form of the linearised system (39), which reads

$$\left[\mathcal{C}^{\mathrm{T}}\mathcal{C} + \mathbf{Q}^{\mathrm{T}}\mathbf{K}_{\mathrm{B}}\mathbf{Q}\right]\delta\mathbf{u}_{\mathrm{m}} = \left[\mathcal{C}^{\mathrm{T}} - \mathbf{Q}^{\mathrm{T}}\mathbf{K}_{\mathrm{B}}\mathbf{R}\right]\left[\mathcal{S}\delta\mathcal{K}_{\mathrm{M}}^u - \mathbf{r}_{\mathrm{c}}\right] + \mathbf{Q}^{\mathrm{T}}\frac{\partial\mathbf{b}_{\mathrm{m}}}{\partial\mathcal{K}_{\mathrm{M}}^u}\delta\mathcal{K}_{\mathrm{M}}^u - \mathbf{Q}^{\mathrm{T}}\mathbf{r}, \tag{40}$$

where $\mathbf{R}^{\mathrm{T}} = (\mathcal{C}\mathcal{C}^{\mathrm{T}})^{-1}\mathcal{C}$ and $\mathbf{Q}^{\mathrm{T}} = \mathbf{I} - (\mathbf{R}\mathcal{C})^{\mathrm{T}}$.

By considering a constant $\mathcal{K}_{\mathrm{M}}^u$, ($\delta\mathcal{K}_{\mathrm{M}}^u = \mathbf{0}$), the system (40) simplifies as

$$\begin{aligned}
\tilde{\mathbf{K}}\delta\mathbf{u}_{\mathrm{m}} &= -\tilde{\mathbf{r}} \quad \text{with} \tag{41}\\
\tilde{\mathbf{K}} &= \mathcal{C}^{\mathrm{T}}\mathcal{C} + \mathbf{Q}^{\mathrm{T}}\mathbf{K}_{\mathrm{B}}\mathbf{Q}, \text{ and} \tag{42}\\
\tilde{\mathbf{r}} &= \mathbf{Q}^{\mathrm{T}}\mathbf{r} + \left[\mathcal{C}^{\mathrm{T}} - \mathbf{Q}^{\mathrm{T}}\mathbf{K}_{\mathrm{B}}\mathbf{R}\right]\mathbf{r}_{\mathrm{c}}. \tag{43}
\end{aligned}$$

The homogenised tangent operators can be extracted during the resolution of the system (40), by evaluating the term $\frac{\partial\mathbf{u}_{\mathrm{m}}}{\partial\mathcal{K}_{\mathrm{M}}^u}$. Since the non-linear system has been solved, the residual vectors $\mathbf{r}$ and $\mathbf{r}_{\mathrm{c}}$ vanish and considering a variation of $\mathcal{K}_{\mathrm{M}}^u$ allows Eq. (40) to be rewritten as

$$\tilde{\mathbf{K}}\delta\mathbf{u}_{\mathrm{m}} = \left[\mathcal{C}^{\mathrm{T}} - \mathbf{Q}^{\mathrm{T}}\mathbf{K}_{\mathrm{B}}\mathbf{R}\right]\mathcal{S}\delta\mathcal{K}_{\mathrm{M}}^u + \mathbf{Q}^{\mathrm{T}}\frac{\partial\mathbf{b}_{\mathrm{m}}}{\partial\mathcal{K}_{\mathrm{M}}^u}\delta\mathcal{K}_{\mathrm{M}}^u, \tag{44}$$

eventually leading to

$$\frac{\partial\mathbf{u}_{\mathrm{m}}}{\partial\mathcal{K}_{\mathrm{M}}^u} = \tilde{\mathbf{K}}^{-1}\left\{\left[\mathcal{C}^{\mathrm{T}} - \mathbf{Q}^{\mathrm{T}}\mathbf{K}_{\mathrm{B}}\mathbf{R}\right]\mathcal{S} + \mathbf{Q}^{\mathrm{T}}\frac{\partial\mathbf{b}_{\mathrm{m}}}{\partial\mathcal{K}_{\mathrm{M}}^u}\right\}. \tag{45}$$

Compared to the expression of $\frac{\partial\mathbf{u}_{\mathrm{m}}}{\partial\mathcal{K}_{\mathrm{M}}^u}$ obtained in [41], an additional body force term, $\frac{\partial\mathbf{b}_{\mathrm{m}}}{\partial\mathcal{K}_{\mathrm{M}}^u}$, or more precisely $\frac{\partial\mathbf{b}_{\mathrm{m}}}{\partial\mathbf{G}_{\mathrm{M}}}$, appears in Eq. (45). Using the expression of the body force given by Eq. (30), we have

$$\begin{aligned}
\left[\frac{\partial\mathbf{b}_{\mathrm{m}}}{\partial\mathbf{G}_{\mathrm{M}}}\right]_{ijKL} &= \int_{\Omega_{\mathrm{m0}}}\left[\frac{\partial\boldsymbol{b}_{\mathrm{m}}}{\partial\mathbf{G}_{\mathrm{M}}}\right]_{ijKL}\mathrm{d}\Omega \\
&= \bigwedge_{\Omega_0^e\in\Omega_{\mathrm{m0}}}\int_{\Omega_0^e}-\frac{1}{2}\left\{\left[\frac{\partial\boldsymbol{P}_{\mathrm{m}}}{\partial\boldsymbol{F}_{\mathrm{m}}}:\frac{\partial\boldsymbol{F}_{\mathrm{m}}}{\partial\boldsymbol{F}_{\mathrm{M}}}\right]_{iLjK}+\left[\frac{\partial\boldsymbol{P}_{\mathrm{m}}}{\partial\boldsymbol{F}_{\mathrm{m}}}:\frac{\partial\boldsymbol{F}_{\mathrm{m}}}{\partial\boldsymbol{F}_{\mathrm{M}}}\right]_{iKjL}\right\}\mathrm{d}\Omega. \tag{46}
\end{aligned}$$

An arc length algorithm can be used to solve the presented boundary value problem defined on the constrained RVE. Because the applied body forces are associated to the boundary constraints though $\mathbf{G}_{\mathrm{M}}$, some modifications related to the existence of the body forces are required with respect to the formulation presented in the literature, e.g. in [37], and are detailed in Appendix B.

4.3. Approximations when evaluating the microscopic body force $\boldsymbol{b}_m$

From the expression of the applied microscopic body force $\boldsymbol{b}_{\mathrm{m}}$, Eq. (30), it can be seen that the derivative of the local deformation gradient, i.e. $\frac{\partial\boldsymbol{F}_{\mathrm{m}}}{\partial\boldsymbol{F}_{\mathrm{M}}}$, is needed to compute $\boldsymbol{b}_{\mathrm{m}}$. This strain concentration tensor $\frac{\partial\boldsymbol{F}_{\mathrm{m}}}{\partial\boldsymbol{F}_{\mathrm{M}}}$ can only be evaluated from Eq. (45) after solving the constrained boundary value problem on the RVE, as shown in Section 4.2. Therefore, the term $\frac{\partial\boldsymbol{F}_{\mathrm{m}}}{\partial\boldsymbol{F}_{\mathrm{M}}}$ extracted from the previous loading time step is used as an approximation in evaluating the local body force at the present step, and the body force at the time step $[t, t+1]$ thus reads,

$$\boldsymbol{b}_{\mathrm{m}}^{(t+1)} \approx -\left(\frac{\partial\boldsymbol{P}_{\mathrm{m}}}{\partial\boldsymbol{F}_{\mathrm{m}}}:\left(\frac{\partial\boldsymbol{F}_{\mathrm{m}}}{\partial\boldsymbol{F}_{\mathrm{M}}}\right)^{(t)}:\mathbf{G}_{\mathrm{M}}\right):\mathbf{I}. \tag{47}$$

When solving the non-linear system of Eqs. (38), the second-order derivative, $\frac{\partial^2\boldsymbol{P}_{\mathrm{m}}}{\partial\boldsymbol{F}_{\mathrm{m}}^2}$, is required to compute the stiffness matrix, $\mathbf{K}_{\mathrm{B}}$, see Eq.(39). This second-order derivative can always be evaluated when

defining the local constitutive law (9). As an option, the computation of this second-order derivative can be avoided by replacing the present $\frac{\partial \boldsymbol{P}_{\mathrm{m}}}{\partial \boldsymbol{F}_{\mathrm{m}}}$ with its previous value in the expression of the body force $\boldsymbol{b}_{\mathrm{m}}$. Thus, a further approximation reads,

$$\boldsymbol{b}_{\mathrm{m}}^{(t+1)} \approx - \left(\left(\frac{\partial \boldsymbol{P}_{\mathrm{m}}}{\partial \boldsymbol{F}_{\mathrm{m}}} \right)^{(t)} : \left(\frac{\partial \boldsymbol{F}_{\mathrm{m}}}{\partial \boldsymbol{F}_{\mathrm{M}}} \right)^{(t)} : \mathbf{G}_{\mathrm{M}} \right) : \mathbf{I} \, . \tag{48}$$

For linear elastic problems, the approximated body forces are exact, since $\frac{\partial \boldsymbol{F}_{\mathrm{m}}}{\partial \boldsymbol{F}_{\mathrm{M}}}$ and $\frac{\partial \boldsymbol{P}_{\mathrm{m}}}{\partial \boldsymbol{F}_{\mathrm{m}}}$ stay constant during the simulations. For non-linear problems, the first approximation on $\frac{\partial \boldsymbol{F}_{\mathrm{m}}}{\partial \boldsymbol{F}_{\mathrm{M}}}$ is essential to establish the system of non-linear equations on the RVE. The second approximation on $\frac{\partial \boldsymbol{P}_{\mathrm{m}}}{\partial \boldsymbol{F}_{\mathrm{M}}}$ is optional, whilst it can simplify a part of computations and its effect on the accuracy is limited when small loading steps are considered, as it will be discussed.

4.4. Macroscopic tangent operators

The homogenised tangent operators, which are needed for the Newton-Raphson iterations of the macroscopic finite element analysis, are defined as

$$\begin{bmatrix} \mathbb{C} & \mathbb{M}^{\mathrm{PG}} \\ \mathbb{M}^{\mathrm{QF}} & \mathbb{L} \end{bmatrix} = \begin{bmatrix} \frac{\partial \boldsymbol{P}_{\mathrm{M}}}{\partial \boldsymbol{F}_{\mathrm{M}}} & \frac{\partial \boldsymbol{P}_{\mathrm{M}}}{\partial \mathbf{G}_{\mathrm{M}}} \\ \frac{\partial \mathbf{Q}_{\mathrm{M}}}{\partial \boldsymbol{F}_{\mathrm{M}}} & \frac{\partial \mathbf{Q}_{\mathrm{M}}}{\partial \mathbf{G}_{\mathrm{M}}} \end{bmatrix} \, , \tag{49}$$

and can be extracted from the numerical resolution of the RVE constrained boundary value problem. The derivatives of the macroscopic first Piola-Kirchhoff stress $\boldsymbol{P}_{\mathrm{M}}$, Eq. (24), read,

$$\begin{aligned} \frac{\partial \boldsymbol{P}_{\mathrm{M}}}{\partial \boldsymbol{F}_{\mathrm{M}}} &= \frac{1}{V_0} \frac{\partial}{\partial \boldsymbol{F}_{\mathrm{M}}} \int_{\Omega_{\mathrm{m}0}} [\boldsymbol{P}_{\mathrm{m}} - \boldsymbol{b}_{\mathrm{m}} \otimes \boldsymbol{X}_{\mathrm{m}}] \, \mathrm{d}\Omega \\ &= \frac{1}{V_0} \int_{\Omega_{\mathrm{m}0}} \left[\frac{\partial \boldsymbol{P}_{\mathrm{m}}}{\partial \boldsymbol{F}_{\mathrm{m}}} - \frac{\partial (\boldsymbol{b}_{\mathrm{m}} \otimes \boldsymbol{X}_{\mathrm{m}})}{\partial \boldsymbol{F}_{\mathrm{m}}} \right] : \frac{\partial \boldsymbol{F}_{\mathrm{m}}}{\partial \boldsymbol{F}_{\mathrm{M}}} \mathrm{d}\Omega \, , \end{aligned} \tag{50}$$

and

$$\begin{aligned} \frac{\partial \boldsymbol{P}_{\mathrm{M}}}{\partial \mathbf{G}_{\mathrm{M}}} &= \frac{1}{V_0} \frac{\partial}{\partial \mathbf{G}_{\mathrm{M}}} \int_{\Omega_{\mathrm{m}0}} [\boldsymbol{P}_{\mathrm{m}} - \boldsymbol{b}_{\mathrm{m}} \otimes \boldsymbol{X}_{\mathrm{m}}] \, \mathrm{d}\Omega \\ &= \frac{1}{V_0} \int_{\Omega_{\mathrm{m}0}} \left[\frac{\partial \boldsymbol{P}_{\mathrm{m}}}{\partial \boldsymbol{F}_{\mathrm{m}}} - \frac{\partial (\boldsymbol{b}_{\mathrm{m}} \otimes \boldsymbol{X}_{\mathrm{m}})}{\partial \boldsymbol{F}_{\mathrm{m}}} \right] : \frac{\partial \boldsymbol{F}_{\mathrm{m}}}{\partial \mathbf{G}_{\mathrm{M}}} \mathrm{d}\Omega \\ &\quad - \frac{1}{V_0} \int_{\Omega_{\mathrm{m}0}} \frac{\partial (\boldsymbol{b}_{\mathrm{m}} \otimes \boldsymbol{X}_{\mathrm{m}})}{\partial \mathbf{G}_{\mathrm{M}}} \mathrm{d}\Omega \, . \end{aligned} \tag{51}$$

The derivatives of the high order stress $\mathbf{Q}_{\mathrm{M}}$, Eq. (25), read

$$\begin{aligned} \frac{\partial \mathbf{Q}_{\mathrm{M}}}{\partial \boldsymbol{F}_{\mathrm{M}}} &= \frac{1}{2V_0} \int_{\Omega_{\mathrm{m}0}} \frac{\partial \left[(\boldsymbol{P}_{\mathrm{m}} \otimes \boldsymbol{X}_{\mathrm{m}}) + (\boldsymbol{P}_{\mathrm{m}} \otimes \boldsymbol{X}_{\mathrm{m}})^{\mathrm{T}_{2,3}} \right]}{\partial \boldsymbol{F}_{\mathrm{m}}} : \frac{\partial \boldsymbol{F}_{\mathrm{m}}}{\partial \boldsymbol{F}_{\mathrm{M}}} \mathrm{d}\Omega \\ &\quad - \frac{1}{2V_0} \int_{\Omega_{\mathrm{m}0}} \frac{\partial \left[\boldsymbol{b}_{\mathrm{m}} \otimes \left(\boldsymbol{X}_{\mathrm{m}} \otimes \boldsymbol{X}_{\mathrm{m}} - \frac{\boldsymbol{J}_{\mathrm{M}}}{V_0} \right) \right]}{\partial \boldsymbol{F}_{\mathrm{m}}} : \frac{\partial \boldsymbol{F}_{\mathrm{m}}}{\partial \boldsymbol{F}_{\mathrm{M}}} \mathrm{d}\Omega \\ &\quad - \frac{1}{2V_0} \frac{\partial}{\partial \boldsymbol{F}_{\mathrm{M}}} \left(\frac{\partial \boldsymbol{P}_{\mathrm{M}}}{\partial \boldsymbol{F}_{\mathrm{M}}} : \mathbf{G}_{\mathrm{M}} \cdot \boldsymbol{J}_{\mathrm{M}} + \left(\frac{\partial \boldsymbol{P}_{\mathrm{M}}}{\partial \boldsymbol{F}_{\mathrm{M}}} : \mathbf{G}_{\mathrm{M}} \cdot \boldsymbol{J}_{\mathrm{M}} \right)^{\mathrm{T}_{2,3}} \right) \, , \end{aligned} \tag{52}$$

and

$$
\begin{aligned}
\frac{\partial \mathbf{Q}_{\mathrm{M}}}{\partial \mathbf{G}_{\mathrm{M}}} \;=\; & \frac{1}{2V_0} \int_{\Omega_{\mathrm{m}0}} \frac{\partial \left[(\boldsymbol{P}_{\mathrm{m}} \otimes \boldsymbol{X}_{\mathrm{m}}) + (\boldsymbol{P}_{\mathrm{m}} \otimes \boldsymbol{X}_{\mathrm{m}})^{\mathrm{T}_{2,3}} \right]}{\partial \boldsymbol{F}_{\mathrm{m}}} \frac{\partial \boldsymbol{F}_{\mathrm{m}}}{\partial \mathbf{G}_{\mathrm{M}}} \mathrm{d}\Omega \\
& -\frac{1}{2V_0} \int_{\Omega_{\mathrm{m}0}} \frac{\partial \left[\boldsymbol{b}_{\mathrm{m}} \otimes \left(\boldsymbol{X}_{\mathrm{m}} \otimes \boldsymbol{X}_{\mathrm{m}} - \frac{\boldsymbol{J}_{\mathrm{M}}}{V_0} \right) \right]}{\partial \boldsymbol{F}_{\mathrm{m}}} : \frac{\partial \boldsymbol{F}_{\mathrm{m}}}{\partial \mathbf{G}_{\mathrm{M}}} \mathrm{d}\Omega \\
& -\frac{1}{2V_0} \int_{\Omega_{\mathrm{m}0}} \frac{\partial \left[\boldsymbol{b}_{\mathrm{m}} \otimes \left(\boldsymbol{X}_{\mathrm{m}} \otimes \boldsymbol{X}_{\mathrm{m}} - \frac{\boldsymbol{J}_{\mathrm{M}}}{V_0} \right) \right]}{\partial \mathbf{G}_{\mathrm{M}}} \mathrm{d}\Omega \\
& -\frac{1}{2V_0} \frac{\partial}{\partial \mathbf{G}_{\mathrm{M}}} \left(\frac{\partial \boldsymbol{P}_{\mathrm{M}}}{\partial \boldsymbol{F}_{\mathrm{M}}} : \mathbf{G}_{\mathrm{M}} \cdot \boldsymbol{J}_{\mathrm{M}} + \left(\frac{\partial \boldsymbol{P}_{\mathrm{M}}}{\partial \boldsymbol{F}_{\mathrm{M}}} : \mathbf{G}_{\mathrm{M}} \cdot \boldsymbol{J}_{\mathrm{M}} \right)^{\mathrm{T}_{2,3}} \right) , \quad (53)
\end{aligned}
$$

where the relation between the macro- and microscopic body forces, Eq. (27), has been used. The derivatives in Eqs. (52) and (53) are further expanded and presented in Appendix C.

In Eqs. (50-53), the expressions $\frac{\partial \boldsymbol{F}_{\mathrm{m}}}{\partial \boldsymbol{F}_{\mathrm{M}}}$ and $\frac{\partial \boldsymbol{F}_{\mathrm{m}}}{\partial \boldsymbol{G}_{\mathrm{M}}}$ are repeatedly used in the volume integration. According to the finite element discretisation of the RVE, one has

$$
\int_{\Omega_{\mathrm{m}0}} \begin{bmatrix} \mathcal{A} & \mathcal{B} \\ \mathcal{C} & \mathcal{D} \end{bmatrix} \begin{bmatrix} \frac{\partial \boldsymbol{F}_{\mathrm{m}}}{\partial \boldsymbol{F}_{\mathrm{M}}} \\ \frac{\partial \boldsymbol{F}_{\mathrm{m}}}{\partial \boldsymbol{G}_{\mathrm{M}}} \end{bmatrix} \mathrm{d}\Omega = \bigwedge_{\Omega_0^e \in \Omega_{\mathrm{m}0}} \int_{\Omega_0^e} \begin{bmatrix} \mathcal{A}^e & \mathcal{B}^e \\ \mathcal{C}^e & \mathcal{D}^e \end{bmatrix} \begin{bmatrix} \mathbb{B}^e \frac{\partial \mathbf{u}_{\mathrm{m}}^e}{\partial \boldsymbol{F}_{\mathrm{M}}} \\ \mathbb{B}^e \frac{\partial \mathbf{u}_{\mathrm{m}}^e}{\partial \boldsymbol{G}_{\mathrm{M}}} \end{bmatrix} \mathrm{d}\Omega , \quad (54)
$$

where $\mathbb{B}^e$ is the gradient matrix of the shape functions of the finite element Ω_0^e, $\mathcal{A}$, $\mathcal{B}$, $\mathcal{C}$ and $\mathcal{D}$ ($\mathcal{A}^e$, $\mathcal{B}^e$, $\mathcal{C}^e$ and $\mathcal{D}^e$) are the (elementary) matrix forms of the coefficient of $\frac{\partial \boldsymbol{F}_{\mathrm{m}}}{\partial \boldsymbol{F}_{\mathrm{M}}}$ or $\frac{\partial \boldsymbol{F}_{\mathrm{m}}}{\partial \boldsymbol{G}_{\mathrm{M}}}$ in Eqs. (50-53), and $\mathbf{u}_{\mathrm{m}}^e$ are the elementary displacement degrees of freedom. Using the results obtained in Section 4.2, Eq. (54) is rewritten as

$$
\int_{\Omega_{\mathrm{m}0}} \begin{bmatrix} \mathcal{A} & \mathcal{B} \\ \mathcal{C} & \mathcal{D} \end{bmatrix} \begin{bmatrix} \frac{\partial \boldsymbol{F}_{\mathrm{m}}}{\partial \boldsymbol{F}_{\mathrm{M}}} \\ \frac{\partial \boldsymbol{F}_{\mathrm{m}}}{\partial \boldsymbol{G}_{\mathrm{M}}} \end{bmatrix} \mathrm{d}\Omega = \bigwedge_{\Omega_0^e \in \Omega_{\mathrm{m}0}} \int_{\Omega_0^e} \begin{bmatrix} \mathcal{A}^e \mathbb{B}^e & \mathcal{B}^e \mathbb{B}^e \\ \mathcal{C}^e \mathbb{B}^e & \mathcal{D}^e \mathbb{B}^e \end{bmatrix} \mathrm{d}\Omega \begin{bmatrix} \frac{\partial \mathbf{u}_{\mathrm{m}}}{\partial \mathcal{K}_{\mathrm{M}}^u} \end{bmatrix} , \quad (55)
$$

where $\frac{\partial \mathbf{u}_{\mathrm{m}}}{\partial \mathcal{K}_{\mathrm{M}}^u}$ is given by Eq. (45).

Remark 6. Because of the dependency on the body forces and correction terms of the macroscopic stress and high order stress, Eqs. (24) and (25), the derivatives $\frac{\partial \boldsymbol{F}_{\mathrm{m}}}{\partial \boldsymbol{F}_{\mathrm{M}}}$, $\frac{\partial \boldsymbol{F}_{\mathrm{m}}}{\partial \boldsymbol{G}_{\mathrm{M}}}$, $\frac{\partial \boldsymbol{b}_{\mathrm{m}}}{\partial \boldsymbol{G}_{\mathrm{M}}}$ required to evaluate the body forces $\boldsymbol{b}_{\mathrm{m}}$ and the homogenised tangent operators need to be computed and saved as internal variables at each integration point of every RVE associated to the macroscopic integration points. Therefore, the presented method is computationally heavier in terms of resources than the "classical" second-order computational homogenisation scheme developed in [36], with respect to the required computer memory.

Remark 7. The macro-scale problem is solved using the enriched discontinuous Galerkin (EDG) method [38]. This method uses continuous second-order elements, and the C^1 continuity is weakly enforced with an interior penalty method. This avoids introducing extra unknown fields beside the nodal displacements, such as the derivatives of nodal displacements [23]. Contrarily to the original method in [38], because the presented method could yield a low or even negative high order modulus as it will be discussed in the next section, the operator defining the stability terms is modified, whilst the consistency term is preserved in order to ensure convergence to the unique solution, as detailed in Appendix D.

5. Numerical examples

In this section, we first study the second-order homogenised response of linear elastic RVEs. Then, the change of patterning of a metamaterial RVE is studied with the presented method and when considering a uniform, but not constant, body force. We finally conduct second-order FE^2 multi-scale analyses of beam bending, honeycomb structure compression and metamaterial structure compression in the context of elasticity, non-linear elasto-plasticity and non-linear elasticity.
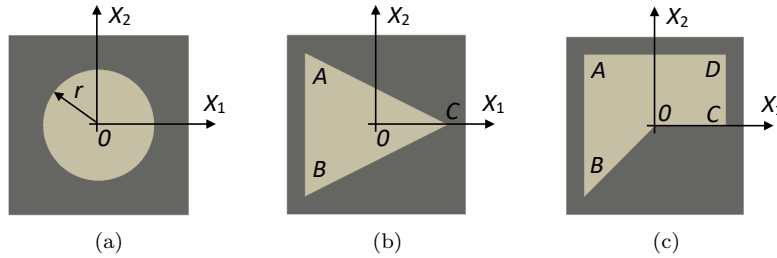
14

Figure 3: Unit cell of length $l = 1\,\mathrm{mm}$: (a) **A** – Circular inclusion ; (b) **B** – Triangular inclusion; and (c) **C** – Asymmetric inclusion.

5.1. Homogenised properties of RVEs

In the following examples, we compare the homogenised behaviours of RVEs predicted by the presented approach with the ones from reference [21] on the different elastic unit-cells presented in Fig. 3. Unless stated otherwise, the length of unit cell is chosen as $l = 1\,\mathrm{mm}$, and the three kinds of unit cells are described as

- **A** – Circular inclusion whose radius is defined by its volume fraction V_f according to $r = l\sqrt{\frac{V_\mathrm{f}}{\pi}}$;

- **B** – Triangular inclusion whose vertices coordinates are $A = [-0.4l, 0.4l]$, $B = [-0.4l, -0.4l]$, $C = [0.4l, 0]$;

- **C** – Asymmetric inclusion whose vertices coordinates are $A = [-0.4l, 0.4l]$, $B = [-0.4l, -0.4l]$, $C = [0.4l, 0]$, $D = [0.4l, 0.4l]$.

Both phases of these unit cells are made of isotropic linear elastic materials, and their Young's moduli and the Poisson's ratios are denoted by (E_0, ν_0) and $(E_\mathrm{I}, \nu_\mathrm{I})$ for the matrix and inclusion phases, respectively. The effective coefficients of second-order homogenised modulus of the RVE are evaluated in order to study the effect of the body force as compared to "classical" second-order homogenisation, and to compare the present model predictions with the results obtained in [21]. With respect to the latter reference, the methods differ on two aspects. On the one hand, in [21], constant and uniform body forces, $\boldsymbol{b}_\mathrm{m} = \boldsymbol{B}_\mathrm{M}$ are applied on RVEs to compute the effective moduli. In this work, the body force applied on the RVE is computed through Eq. (30), which can vary according to the heterogeneity in the RVE. On the other hand, in [21], Quadratic Boundary Conditions (QBC), which read

$$\boldsymbol{u}_\mathrm{m}(\boldsymbol{X}_\mathrm{m}) = (\boldsymbol{F}_\mathrm{M} - \boldsymbol{I}) \cdot \boldsymbol{X}_\mathrm{m} + \frac{1}{2}\mathbf{G}_\mathrm{M} : (\boldsymbol{X}_\mathrm{m} \otimes \boldsymbol{X}_\mathrm{m}) \qquad \forall \boldsymbol{X}_\mathrm{m} \in \partial\Omega_\mathrm{m0}\,, \tag{56}$$

are applied on the RVEs to compute the effective moduli, whilst periodical boundary conditions, which permit fluctuation $\boldsymbol{w}(\boldsymbol{X}_\mathrm{m})$ to exist on the RVE boundary $\partial\Omega_0$, are used in the present methodology.

5.1.1. Effect of inclusion volume fraction V_f of unit cell **A** on the homogenised properties of RVEs

The studied RVE consists in a cluster of 4×4 unit cells with the material properties $E_0 = 1\,\mathrm{MPa}$, $\nu_0 = 0.45$ for the matrix, and $E_\mathrm{I} = 10\,\mathrm{MPa}$, $\nu_\mathrm{I} = 0.3$ for the inclusions. The variation of the ratio between the radius of the inclusions r and the length of the unit cell l is used to represent the change of inclusion volume fraction V_f. The effective coefficients of the second-order homogenised modulus, $\mathbb{L}$ in Eq. (49), of the RVE are computed with and without body forces, and the results are presented in Fig. 4 together with the results of the reference [21], in which a uniform body force is considered. The studied cases show that the effective high order moduli obtained with the proposed method have the same order of magnitude as in the reference [21] and are several orders of magnitude lower than in the absence of body forces.

15
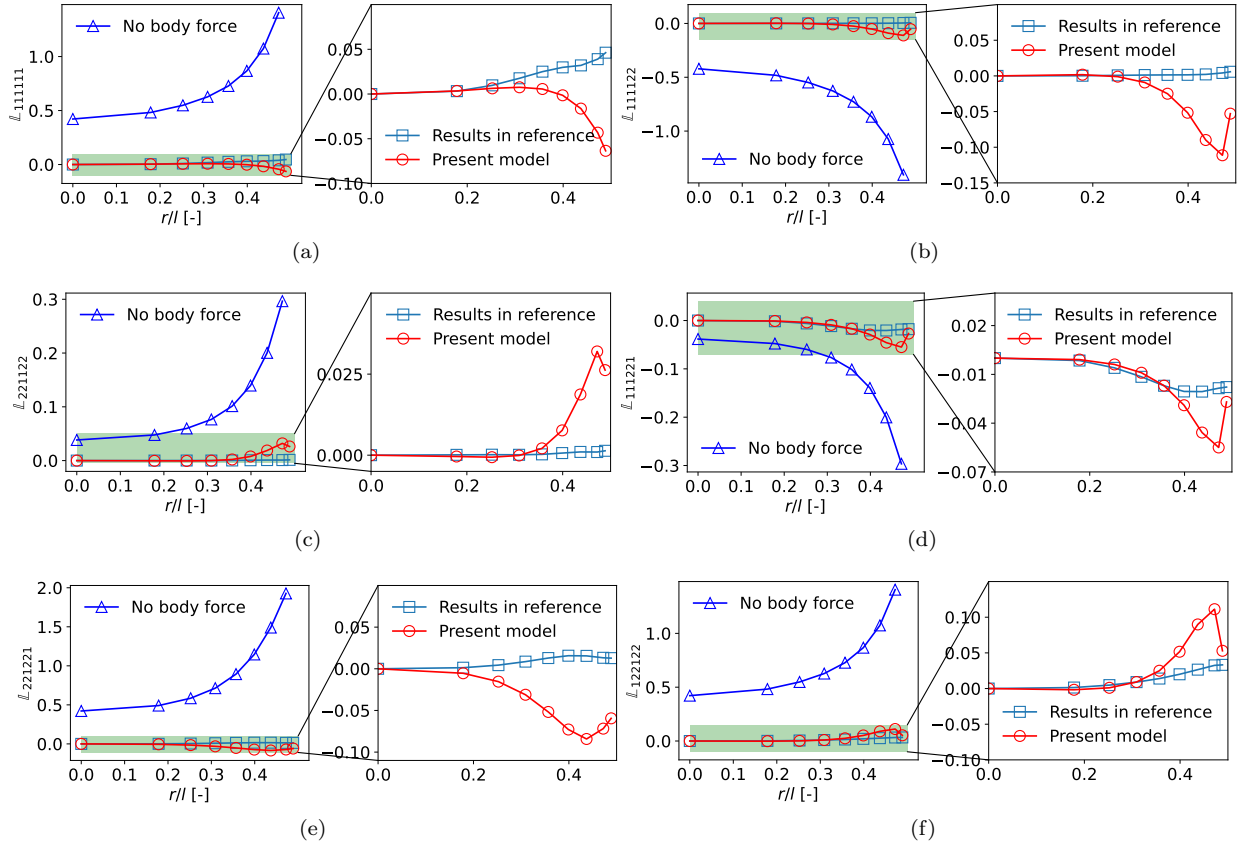
Figure 4: The effective coefficients of second-order homogenised modulus $\mathbb{L}$ (units in N) of RVEs consisting of 4×4 unit cells **A** – Comparison of the model prediction with respect to classical second-order homogenisation and with respect to reference [21] for different volume fractions.
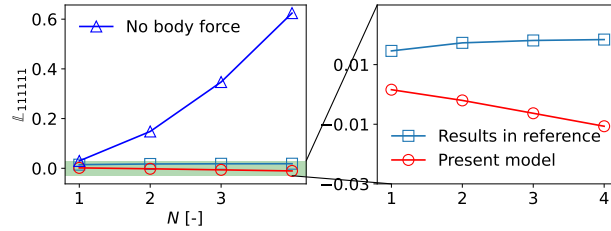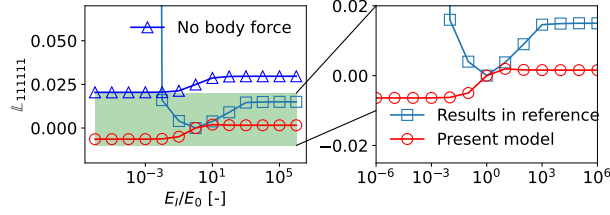

Figure 5: The effective coefficient $\mathbb{L}_{111111}$ of the second-order homogenised modulus (units in N) of the RVE with $N \times N$ unit cells **A** – Comparison of the model prediction with respect to classical second-order homogenisation and with respect to reference [21] for different numbers of cell N.

5.1.2. Effect of the number of unit cells on the homogenised properties of RVEs consisting of $N \times N$ unit cells **A**

For this study, successive RVEs consisting of $N \times N$ unit cells **A**, i.e. considering circular inclusions see Fig. 3(a), are considered for increasing values of N. The elastic material properties are $E_0 = 1\,\mathrm{MPa}$, $\nu_0 = 0.3$ for the matrix, and $E_\mathrm{I} = 10^3\,\mathrm{MPa}$, $\nu_\mathrm{I} = 0.3$ for the inclusions. A constant inclusion volume fraction $V_\mathrm{f} = 0.3$ is adopted. The length of the unit cell is kept to $l = 1\,\mathrm{mm}$, and the effective properties are computed as a function of the number of unit cells $N \times N$. The effective coefficients $\mathbb{L}_{111111}$ of the second-order homogenised modulus of the presented model with a non-uniform body force and of reference

16

[21], in which a uniform body force is considered, are compared in Fig. 5 to the predictions of the "classical" second-order homogenisation without body force. Since for a $N \times N$ RVE, we have a longer RVE side, and since the unit of $\mathbb{L}_{111111}$ is in Newton, we observe an evolution of $\mathbb{L}_{111111}$ with respect to N, but which is of several orders of magnitude lower than in the absence of body forces.

5.1.3. Effect of phases properties contrast on the homogenised properties of RVEs consisting of one unit cell **A**

Figure 6: The effective coefficient $\mathbb{L}_{111111}$ of the second-order homogenised modulus (units in N) of the RVE with one unit cell **A** of $V_f = 0.3$ – Comparison of the model prediction with respect to classical second-order homogenisation and with respect to reference [21] for different contrasts E_I/E_0 of phases properties.

In this study, a RVE, which consists of 1×1 unit cell **A**, is used to avoid divergence problem with respect to the number of unit cells in the RVE. A circular inclusion with a volume fraction $V_f = 0.3$ is considered. The elastic properties of the matrix are $E_0 = 1\,\mathrm{MPa}$ and $\nu_0 = 0.3$, and the elastic properties of the inclusion satisfy $\nu_I/\nu_0 = 1$ with the contrast of Young's moduli E_I/E_0 varying from 10^{-6} to 10^6. The evolution of the effective coefficient $\mathbb{L}_{111111}$ of the second-order homogenised modulus is presented in Fig. 6. The present model with body forces leads to convergent values of the higher-order properties for both hard and soft inclusions. On the contrary, in [21], different body force assumptions were required to achieve convergent values of the higher-order properties for hard and soft inclusions.

5.1.4. Micro-structure size effect on the homogenised properties of RVEs consisting of 4×4 unit cells **B**
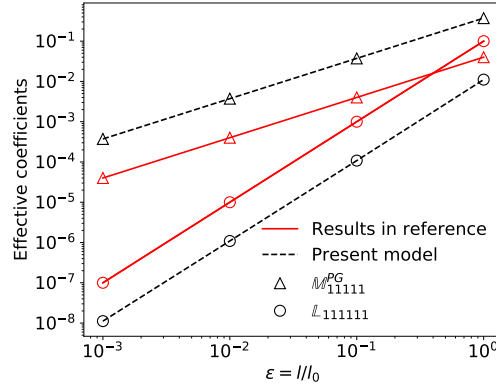
Figure 7: The micro-structure size effect on the effective coefficients of the second-order homogenised moduli $\mathbb{M}$ (units in N·mm^{-1}) and $\mathbb{L}$ (units in N) of the RVE with 4×4 unit cells **B** – Comparison of the model prediction with respect to reference [21] for different micro-structure size ratios $\varepsilon = l/l_0$, where $l_0 = 1.0$ mm.

In this example, we compare the size-effects captured by the proposed method and the results presented in reference [21] for a uniform body force. The studied RVE consists in 4×4 unit cells **B**, i.e. with a triangular inclusion as seen in Fig. 3(b). The elastic material properties are $E_0 = 1\,\mathrm{MPa}$, $\nu_0 = 0.3$ for the matrix, and $E_I = 10^2\,\mathrm{MPa}$, $\nu_I = 0.3$ for the inclusions. The length of the unit cell l varies from 1×10^{-3} to 1.0 mm. The variations of the effective high order moduli $\mathbb{M}$ and $\mathbb{L}$ defined in Eq. (49) according to $\varepsilon = l/l_0$, where $l_0 = 1.0$ mm, are presented in Fig. 7. With the proposed method, the obtained high order moduli

17

are not necessarily satisfying $\mathbb{M}^{PG} = \mathbb{M}^{QF}$, and in this example, the coefficient of $\mathbb{M}^{QF}$ is several orders of magnitude lower than $\mathbb{M}^{PG}$. Hence, only the results of $\mathbb{M}^{PG}$ are plotted in Fig. 7. It can be seen that $\mathbb{M}$ and $\mathbb{L}$ vary according to ε and ε^2, respectively, as expected when considering bending theory, similarly to the reference results.

5.2. Deformation of RVEs under different macroscopic strain gradient components

5.2.1. Body force distribution and deformation of unit cell $\mathbf{A}$
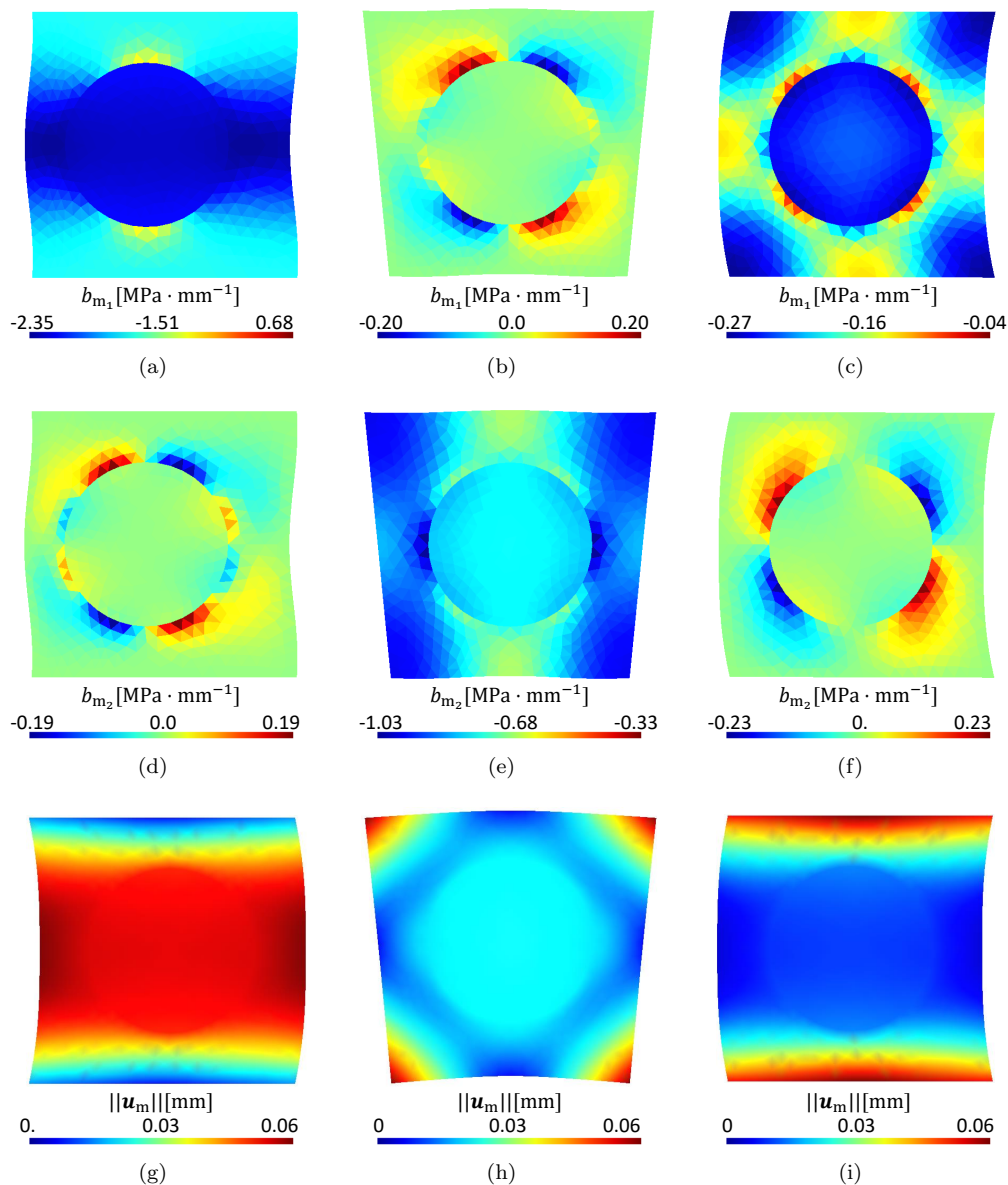
Figure 8: Body force distribution and deformed configurations of unit cell $\mathbf{A}$ simulated successively (a-f) considering the body forces and (g-i) not considering the body forces when subjected to $\boldsymbol{F}_\mathrm{M} = \mathbf{I}$ and to: (a, d, g) $G_{\mathrm{M}_{111}} = 0.4\,\mathrm{mm}^{-1}$; (b, e, h) $G_{\mathrm{M}_{112}} = G_{\mathrm{M}_{121}} = 0.2\,\mathrm{mm}^{-1}$; and (c, f, i) $G_{\mathrm{M}_{122}} = 0.4\,\mathrm{mm}^{-1}$.

18
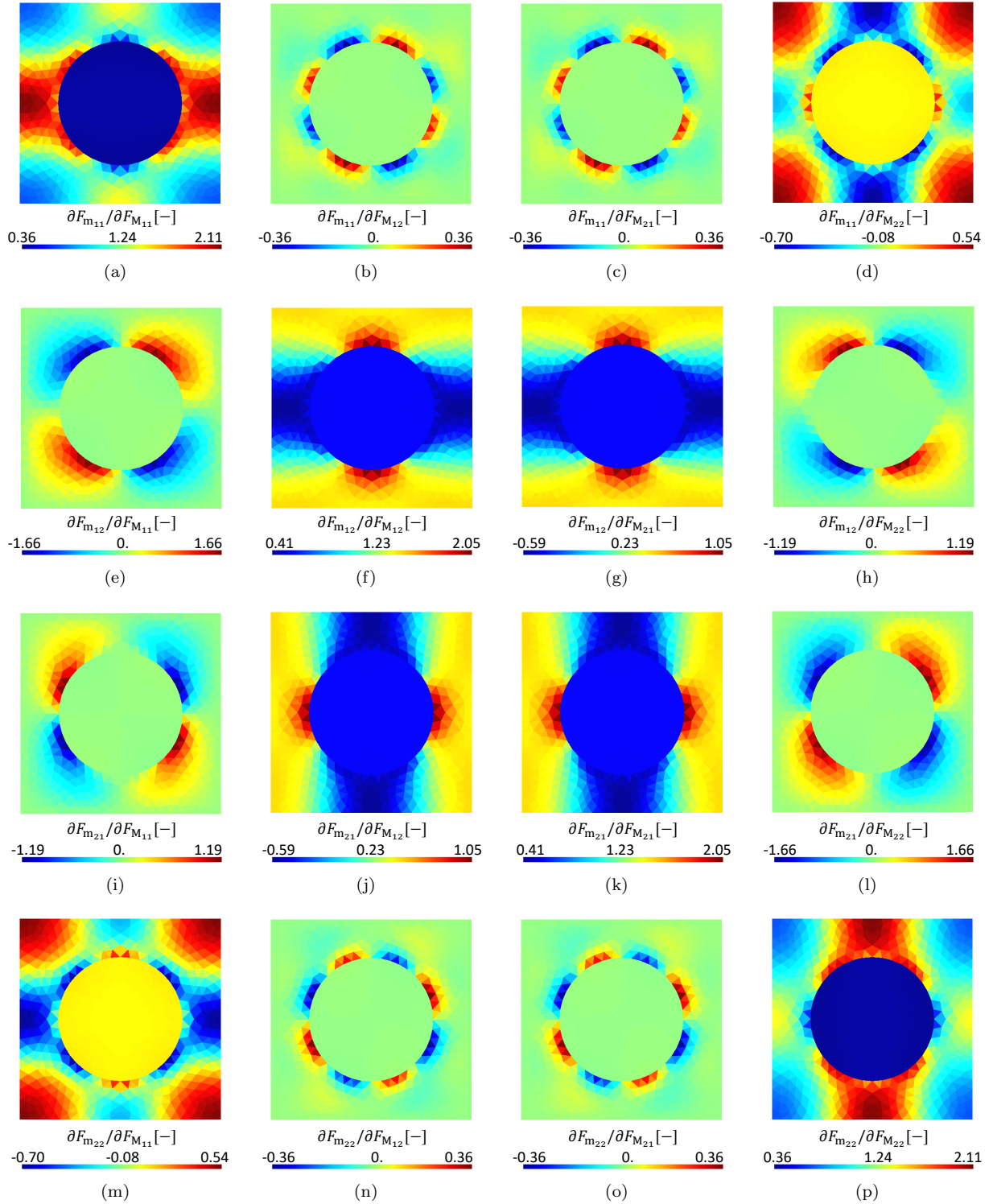
Figure 9: Distributions of the different components of $\frac{\partial \boldsymbol{F}_{\mathrm{m}}}{\partial \boldsymbol{F}_{\mathrm{M}}}$ for unit cell $\mathbf{A}$.

The unit cell $\mathbf{A}$ with inclusion volume fraction $V_f = 0.3$, is used as the RVE and subjected to different macroscopic strain gradients with zero macroscopic strain. The same material properties as presented in Section 5.1.1 are considered in this example. Three macroscopic strain gradient conditions, $G_{M_{111}} = 0.4\,\mathrm{mm}^{-1}$, $G_{M_{112}} = G_{M_{121}} = 0.2\,\mathrm{mm}^{-1}$ and $G_{M_{122}} = 0.4\,\mathrm{mm}^{-1}$ are applied successively on the unit cell. The local body force distributions are displayed on the deformed RVE in Figs. 8(a-f). The same loading conditions are then considered but without accounting for the body forces, and the corresponding deformations of the unit cell are presented in Figs. 8(g-i) for comparison purpose. It can be seen that the deformation of the unit cell is changed in the presence of the local body forces, especially for the cases $G_{M_{111}} = 0.4\,\mathrm{mm}^{-1}$ and $G_{M_{112}} = G_{M_{121}} = 0.2\,\mathrm{mm}^{-1}$. The distributions of the different components of the strain concentration tensor $\frac{\partial \boldsymbol{F}_m}{\partial \boldsymbol{F}_M}$, which governs the distribution of the body forces through Eq. (30), are illustrated in Fig. 9. In this figure, the effect of the stiffer inclusion in the matrix exemplifies the reason why the body force is not uniform. We note that in the linear case these distributions do not depend on the loading case.

5.2.2. Deformation of RVEs consisting in 4×4 unit cells $\mathbf{C}$
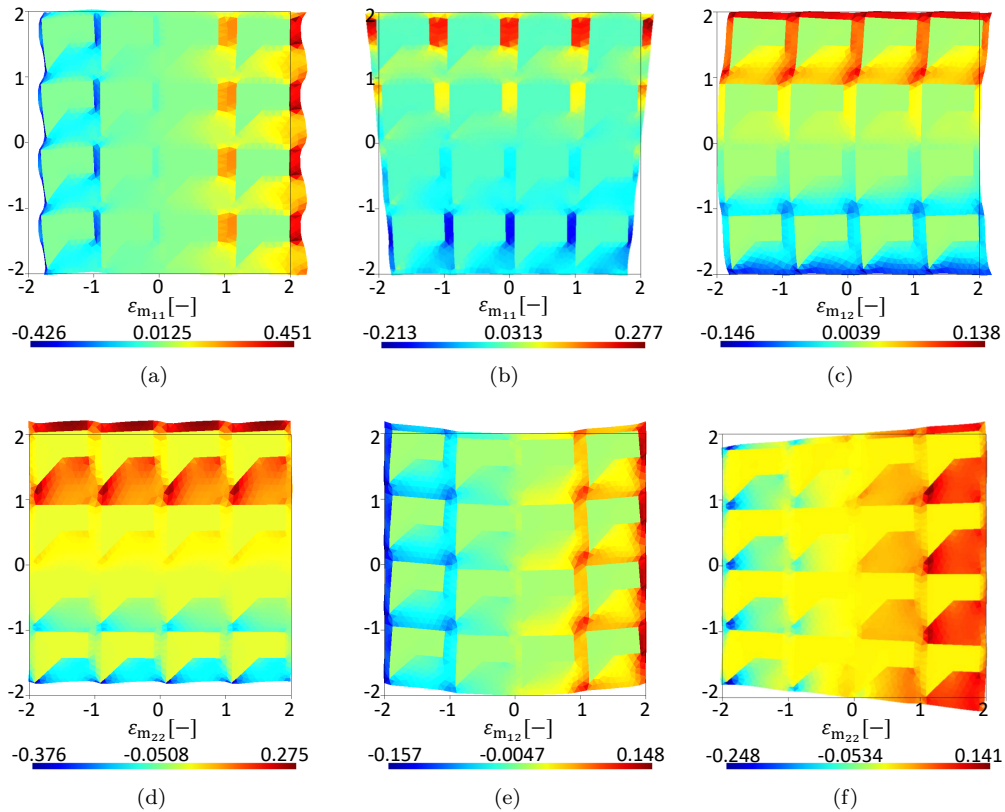
Figure 10: Strain fields and deformed configurations of a RVE with 4×4 unit cells $\mathbf{C}$ simulated considering the body forces and subjected to $\boldsymbol{F}_M = \mathbf{I}$ and to: (a) $G_{M_{111}} = 0.05\,\mathrm{mm}^{-1}$; (b) $G_{M_{112}} = G_{M_{121}} = 0.025\,\mathrm{mm}^{-1}$; (c) $G_{M_{122}} = 0.05\,\mathrm{mm}^{-1}$; (d) $G_{M_{222}} = 0.05\,\mathrm{mm}^{-1}$; (e) $G_{M_{211}} = 0.05\,\mathrm{mm}^{-1}$; and (f) $G_{M_{221}} = G_{M_{212}} = 0.025\,\mathrm{mm}^{-1}$.

In this example, the different components of the macroscopic strain gradient are successively applied on a RVE consisting of 4×4 unit cells $\mathbf{C}$. The elastic material properties are $E_0 = 1\,\mathrm{MPa}$, $\nu_0 = 0.3$ for the matrix, and $E_I = 10^2\,\mathrm{MPa}$, $\nu_I = 0.3$ for the inclusions. Higher order homogenisation is successively conducted with and without accounting for the body forces, and the associated deformed RVEs are respectively shown in Fig. 10 and in Fig. 11, in which the micro-scale strain fields are also depicted. When accounting for the body forces, the phenomenon of deformation concentrating at the RVE boundaries seen in Fig. 11, which

20
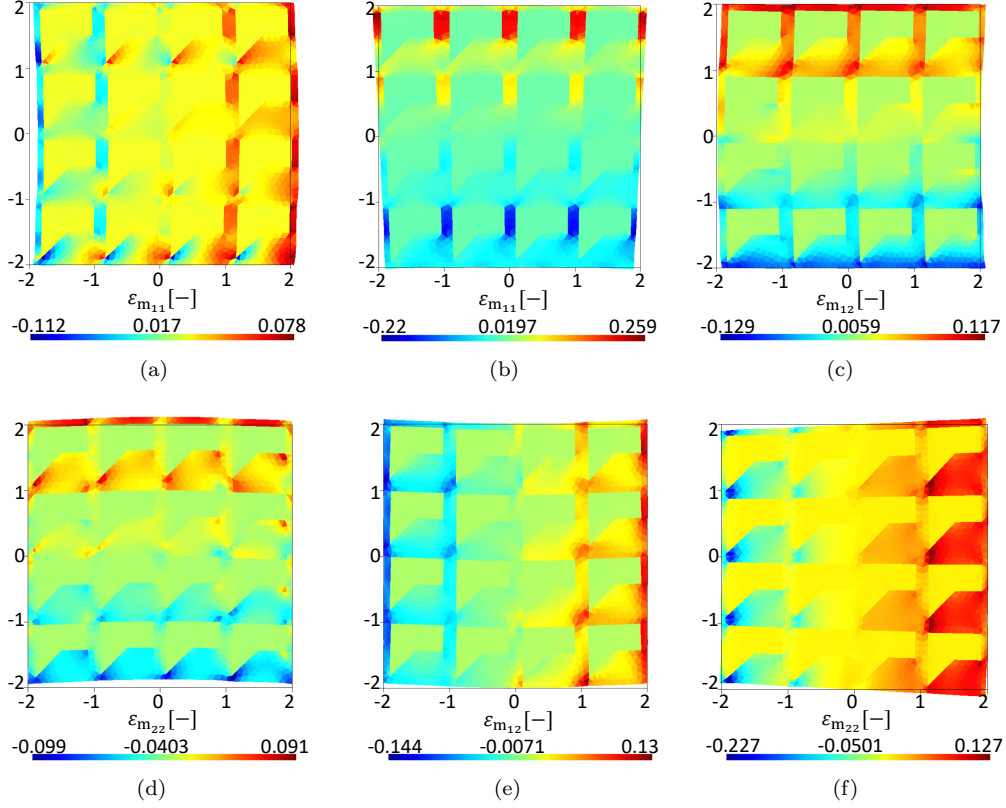
Figure 11: Strain fields and deformed configurations of a RVE with 4×4 unit cells **C** simulated not considering the body forces and subjected to $\boldsymbol{F}_{\mathrm{M}} = \mathbf{I}$ and to: (a) $G_{\mathrm{M}_{111}} = 0.05\,\mathrm{mm}^{-1}$; (b) $G_{\mathrm{M}_{112}} = G_{\mathrm{M}_{121}} = 0.025\,\mathrm{mm}^{-1}$; (c) $G_{\mathrm{M}_{122}} = 0.05\,\mathrm{mm}^{-1}$; (d) $G_{\mathrm{M}_{222}} = 0.05\,\mathrm{mm}^{-1}$; (e) $G_{\mathrm{M}_{211}} = 0.05\,\mathrm{mm}^{-1}$; and (f) $G_{\mathrm{M}_{221}} = G_{\mathrm{M}_{212}} = 0.025\,\mathrm{mm}^{-1}$.

has also been observed in [16] (Fig. 6), is avoided. Indeed, on the one hand the micro-scale deformation fields are higher when considering the body forces, in particular for loading under $G_{\mathrm{M}_{111}}$ and $G_{\mathrm{M}_{222}}$ constraints, and on the other hand the absence of body forces under $G_{\mathrm{M}_{111}}$ and $G_{\mathrm{M}_{222}}$ constraints induces a curvature of the RVE which is prevented when considering the body force; we refer to Fig. 11(a) compared to Fig. 10(a) and to Fig. 11(d) compared to Fig. 10(d).

5.3. The effect of the loading step increment on capturing the RVE instabilities under different body forces assumptions
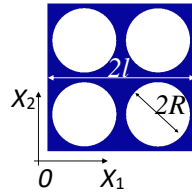
Figure 12: Holed RVE consisting of 2×2 unit cells able to capture the change of patterning.

In this section, the patterning change of a holed RVE under compression is studied. The characteristic geometry of a perfect holed RVE is illustrated in Fig. 12, with the periodicity length $l = 9.97$ mm and hole radius $R = 4.335$ mm. A small random disturbance is added to each hole by creating ellipsoids instead of

21

circles with a change of radius of $0.002 \times R$. The matrix hyperelastic material model corresponds to the real structural material used by Bertoldi et al. [35]. The constitutive behaviour of this elastomer base material is governed by the elastic potential which reads

$$\psi(\boldsymbol{F}) = c_1(I_1 - 3) + c_2(I_1 - 3)^2 - 2c_1 \log(J) + \frac{1}{2}K(J-1)^2 \,, \tag{57}$$

where $I_1 = \mathrm{tr}(\boldsymbol{C})$. The material parameters are based on the experimental characterisation conducted in [35], with $c_1 = 0.55\,\mathrm{MPa}$, $c_2 = 0.3\,\mathrm{MPa}$, $K = 55\,\mathrm{MPa}$. The RVE, see Fig. 12, consists in 2×2 unit cells in order to capture the change of patterning during the compression analysis. This periodicity was determined in [35] through a Bloch-Wave analysis. The RVE of 2×2 unit cells is under plane stress condition, and subjected to $\boldsymbol{F}_\mathrm{M} = 0.9 \times \mathbf{I}$, $G_{\mathrm{M}_{111}} = 0.02\,\mathrm{mm}^{-1}$ and $G_{\mathrm{M}_{112}} = G_{\mathrm{M}_{121}} = 0.01\,\mathrm{mm}^{-1}$.
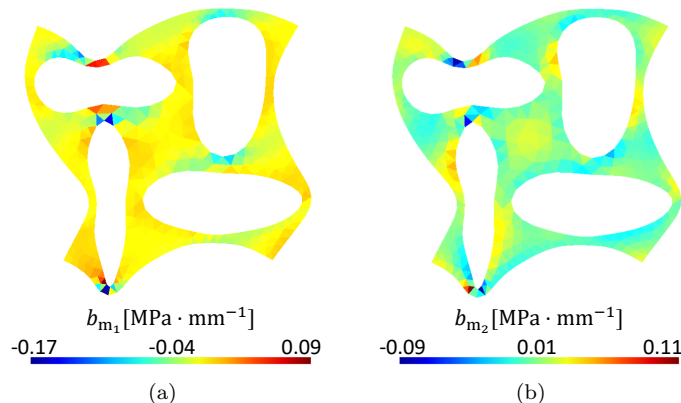
Figure 13: The distributions of the body force (48) components on the deformed holed 2×2-unit cell RVE subjected to $\boldsymbol{F}_\mathrm{M} = 0.9 \times \mathbf{I}$, $G_{\mathrm{M}_{111}} = 0.02\,\mathrm{mm}^{-1}$ and $G_{\mathrm{M}_{112}} = G_{\mathrm{M}_{121}} = 0.01\,\mathrm{mm}^{-1}$.

First, the body force is evaluated using the approximation Eq. (48). In order to assess the effect of this explicit scheme approximation, the final macroscopic deformation gradient and its gradient are applied on the RVE by considering successively 50, 100, 200, 400 and 800 loading increments. The final distributions of the body forces (48) are shown on the deformed RVE in Fig. 13. The final deformation was found to be insensitive to the number of increments (the figure displays the results for 400 increments). The evolutions of the macroscopic stress $\boldsymbol{P}_\mathrm{M}$ and of the high order stress $\mathbf{Q}_\mathrm{M}$ are plotted in Fig. 14 to show the effect of the number of loading increments. In Figs. 14(a) and 14(b), it can be seen that the number of loading steps has little effect on the evolution of the macroscopic stress $\boldsymbol{P}_\mathrm{M}$, whilst the evolution of the high order stress varies at the onset of instability, here the patterning change, with the number of loading increments, see Figs. 14(c) and 14(d). Since the body force $\boldsymbol{b}_\mathrm{m}$ needs to be computed using $\frac{\partial \boldsymbol{F}_\mathrm{m}}{\partial \boldsymbol{F}_\mathrm{M}}$, which exhibits a sudden change at the onset of patterning change, the use of the approximation Eq. (48) has an effect on the extracted high order stress at the instability onset. However, this effect gradually diminishes when the patterning change is completed, and the variation of the high order stress becomes moderate with the increase of loading steps.

Second, a uniform approximation of the body force $\bar{\boldsymbol{b}}_\mathrm{m}$ is applied on RVE during the simulations. This uniform body force $\bar{\boldsymbol{b}}_\mathrm{m}$ satisfies $\int_{\Omega_{\mathrm{m}0}} \bar{\boldsymbol{b}}_\mathrm{m} \mathrm{d}\Omega = \int_{\Omega_0} \boldsymbol{B}_\mathrm{M} \mathrm{d}\Omega$, which yields $\bar{\boldsymbol{b}}_\mathrm{m} = \frac{V_0}{\bar{V}_{\mathrm{m}0}} \boldsymbol{B}_\mathrm{M}$, where $\bar{V}_{\mathrm{m}0}$ is the volume of the material part of the RVE, i.e. voids excluded. An approximation, which is similar to Eq. (48), is used to evaluate the macroscopic body force $\boldsymbol{B}_\mathrm{M}$, and reads

$$\boldsymbol{B}_\mathrm{M}^{(t+1)} \approx -\left(\frac{\partial \boldsymbol{P}_\mathrm{M}}{\partial \boldsymbol{F}_\mathrm{M}}^{(t)} : \mathbf{G}_\mathrm{M} \right) : \mathbf{I} \,. \tag{58}$$

The evolutions of the macroscopic stress $\boldsymbol{P}_\mathrm{M}$ and of the high order stress $\mathbf{Q}_\mathrm{M}$ under this approximation of the body forces are also extracted for different numbers of loading increments and plotted in Fig. 15.
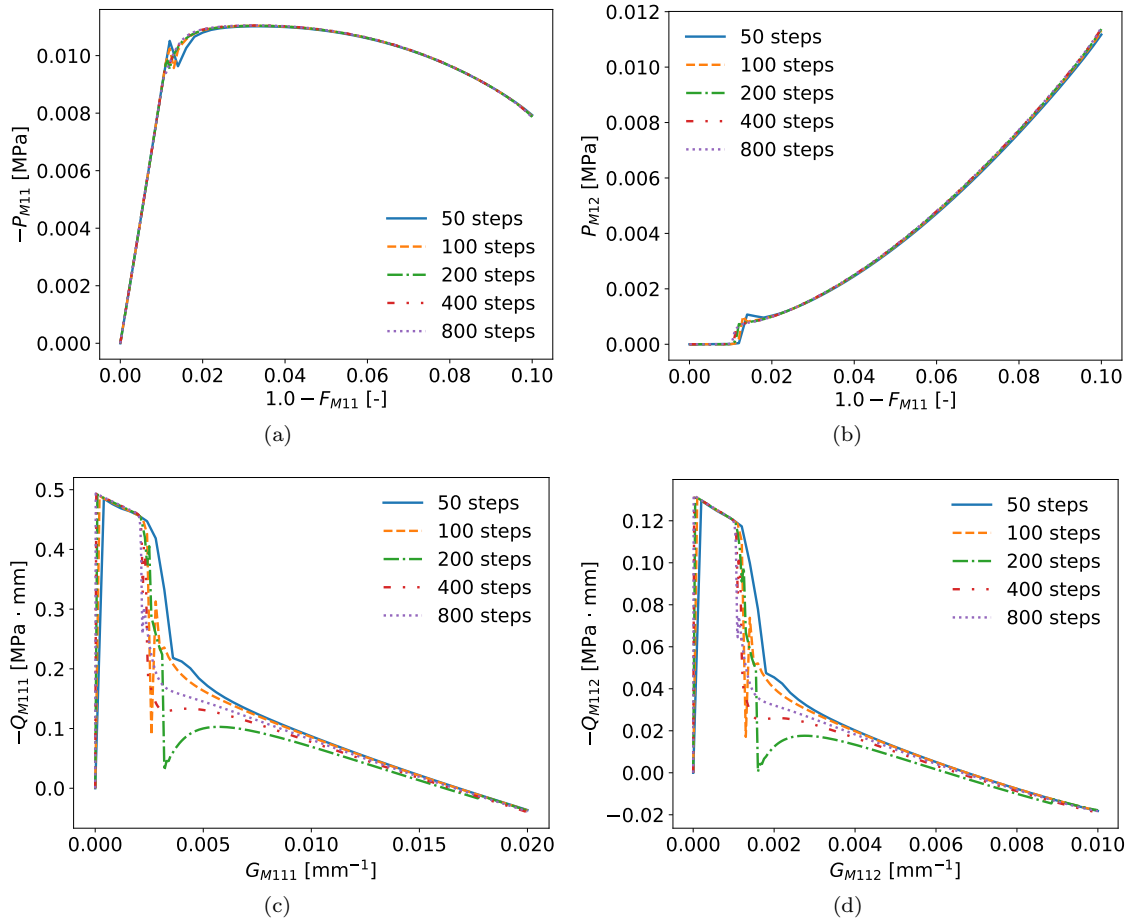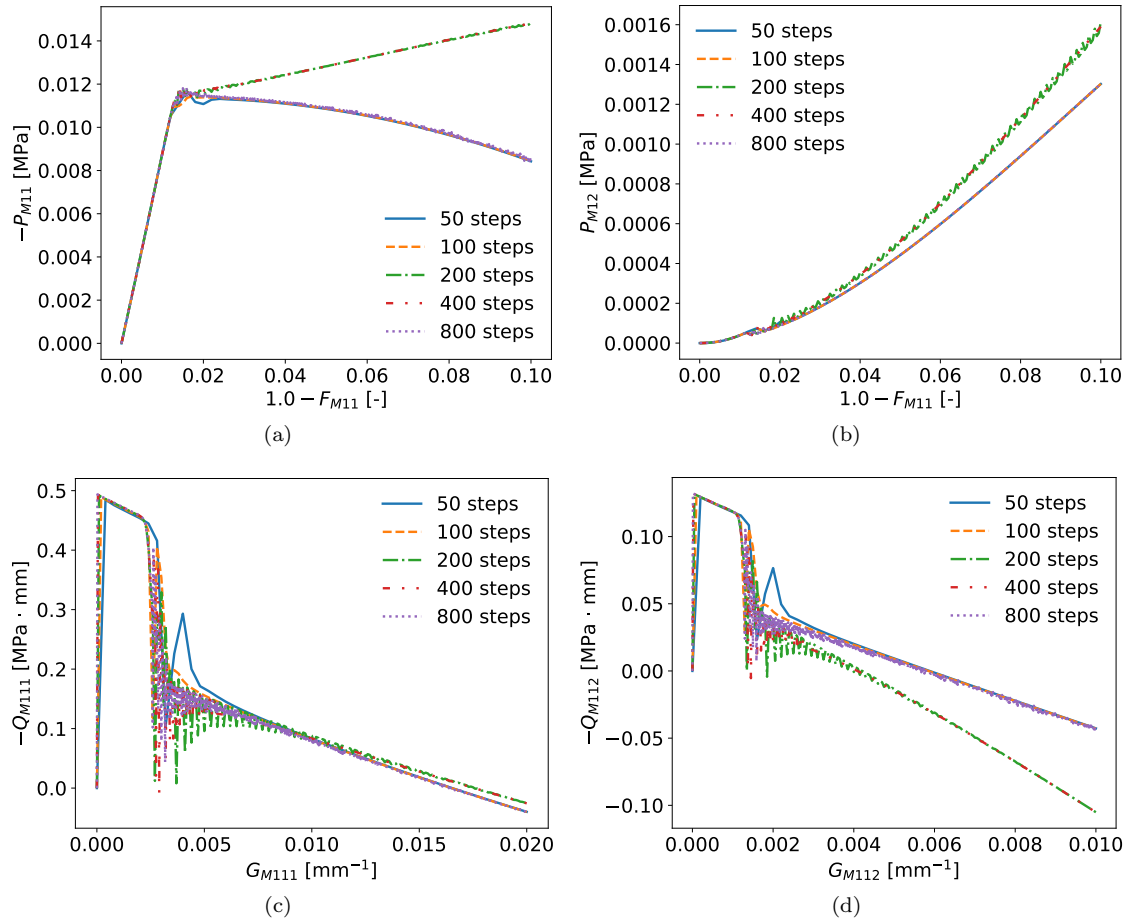
Figure 14: Macroscopic stress and high order stress evolutions of the holed 2×2-unit cell RVE when considering the body forces approximation (48) for different numbers of loading increments.

An oscillation of the high order stress appears at the deformation patterning change stage, although its amplitude decreases with the increase of loading steps, see Figs. 15(c) and 15(d). Under uniform body forces, but not constant during the deformation history, the macroscopic stress $\boldsymbol{P}_{\mathrm{M}}$ and the high order stress $\mathbf{Q}_{\mathrm{M}}$ extracted from the RVE fall into two branches for different numbers of loading steps, see Fig. 15. It turns out that the uniform body force can lead to two different deformation patterning changes at instability onset, despite the fact that the combination of $G_{\mathrm{M}_{111}} = 0.02 \, \mathrm{mm}^{-1}$ and $G_{\mathrm{M}_{112}} = G_{\mathrm{M}_{121}} = 0.01 \, \mathrm{mm}^{-1}$ should favour the deformation mode displayed in Fig. 13 since the lower left hole has more compression along the X_1-direction. The body forces at the final step are displayed on the deformed RVE for the cases of 100 and 200 loading increments in Fig. 16, which shows the two different patterning changes. In Figs. 14 and 15, fluctuations of the high order stress can be seen at the onset of RVE deformation pattering change. Therefore, during multi-scale analyses, a rather small time step at the microscopic simulation level is needed to smooth this fluctuation and guarantee the convergence of the macro-scale integration. This smaller time step required during the microscopic simulations increases the whole computation time.

5.4. Structural analyses

In this subsection, the presented method is applied in FE^2 multi-scale analyses of structures.

23

Figure 15: Macroscopic stress and high order stress evolutions of the holed 2×2-unit cell RVE when considering the uniform body forces $\frac{V_0}{V_{m0}} \boldsymbol{B}_M$ for different numbers of loading increments.

5.4.1. 2D beam under bending and shearing

A 2D beam consisting of 4×10 unit cells $\mathbf{C}$ is studied under plane strain state assumption. We use the same linear elastic material properties as in Section 5.2.2 and we adopt a RVE consisting of one unit cell $\mathbf{C}$ for the FE^2 multi-scale analysis. Two kinds of boundary conditions are successively considered: bending and shearing boundary conditions are illustrated respectively in Figs. 17(a) and 17(c). In the multiscale analyses, the high order boundary conditions are enforced by adding extra elements (in green in Figs. 17(a) and 17(c)) at the boundary of the macroscopic structure: these green elements either are totally constrained or have rigid body motion only, and the use of the EDG method weakly ensures that the gradients of displacements is continuous at their interfaces with the structural elements (in blue). The macroscopic 2D beam is discretised successively into 2×5, 3×8 and 4×10 elements, see Figs. 17(a) and 17(c) for the mesh of 4×10 elements.

The responses of the beam are presented in terms of the force vs. displacement curves in Figs. 17(b) and 17(d) for the direct numerical simulations (DNS) and for the high order computational homogenisation with and without accounting for the body forces. Besides, the corresponding deformation energies of the beam are plotted in terms of the displacement in Fig. 18. In the bending case, Figs. 17(b) and 18(a), it can be seen that the present method overestimates the response when considering coarse macroscopic meshes, whilst accurate results are obtained when the macroscopic element size reached the same size as that of the RVE. However, the high order computational homogenisation without body force still overestimates
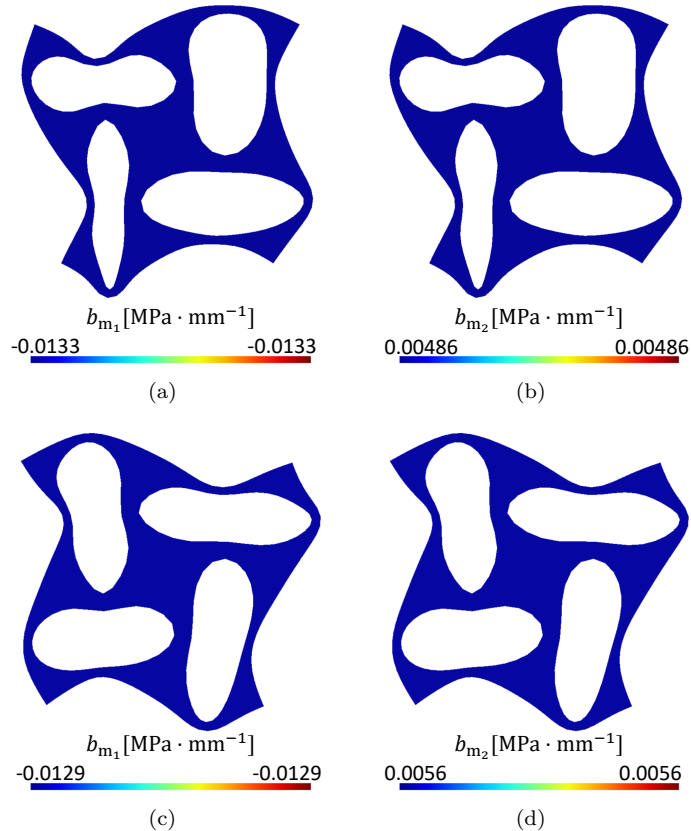
24

Figure 16: The distributions of the uniform body force $\frac{V_0}{V_{m0}} \boldsymbol{B}_M$ components on the deformed holed 2×2-unit cell RVE subjected to $\boldsymbol{F}_M = 0.9 \times \mathbf{I}$, $G_{M_{111}} = 0.02\,\mathrm{mm}^{-1}$ and $G_{M_{112}} = G_{M_{121}} = 0.01\,\mathrm{mm}^{-1}$ (we note the constant value in the scales): (a, b) When considering 100 loading increments; and (c, d) When considering 200 loading increments.

Table 1: Coefficients of tensor $\mathbb{L}$ (units in N) of RVEs consisting of one unit cell $\mathbf{C}$.

$\mathbb{L}_{111111}$	$\mathbb{L}_{222222}$	$\mathbb{L}_{121121}$	$\mathbb{L}_{221221}$	$\mathbb{L}_{122122}$	$\mathbb{L}_{211211}$
-0.0166	-0.0112	-0.0187	-0.0063	-0.0192	-0.0124

the response force with the fine mesh of 4×10 macro-scale elements. In the shearing case, Figs. 17(d) and 18(b), the response is overestimated by the methods with or without body force, although the results of the present method are closer to the DNS ones with the refinement of the macroscopic mesh. The difference observed in the shearing case can be explained as follows. In the direct numerical simulations, the displacement constraints were applied directly on the soft matrix material, which created relatively higher local deformation at the corners of the structures. This phenomenon cannot be captured by the multi-scale simulation since the cell size is close to the structural size and the macroscopic element size is much bigger than that in the direct numerical simulation. This boundary effect is less significant in the bending case.

For both bending and shearing cases, results converge upon refinement of the macro-scale mesh when considering the body forces, and an over-stiff behaviour is observed for second-order homogenisation without body force, see Figs. 17(b) and 17(d). On the one hand, second-order homogenisation without body force always yields a positive definite tensor $\mathbb{L}$, hence increasing the stiffness of the homogenised response. On the other hand, considering body forces yields non positiveness of the effective coefficients of the high order modulus $\mathbb{L}$ of cell $\mathbf{C}$ listed in Tab. 1. According to the idea of equivalent macroscopic volume used in the presented method, these negative principal components mean that the ability to withstand high order forces
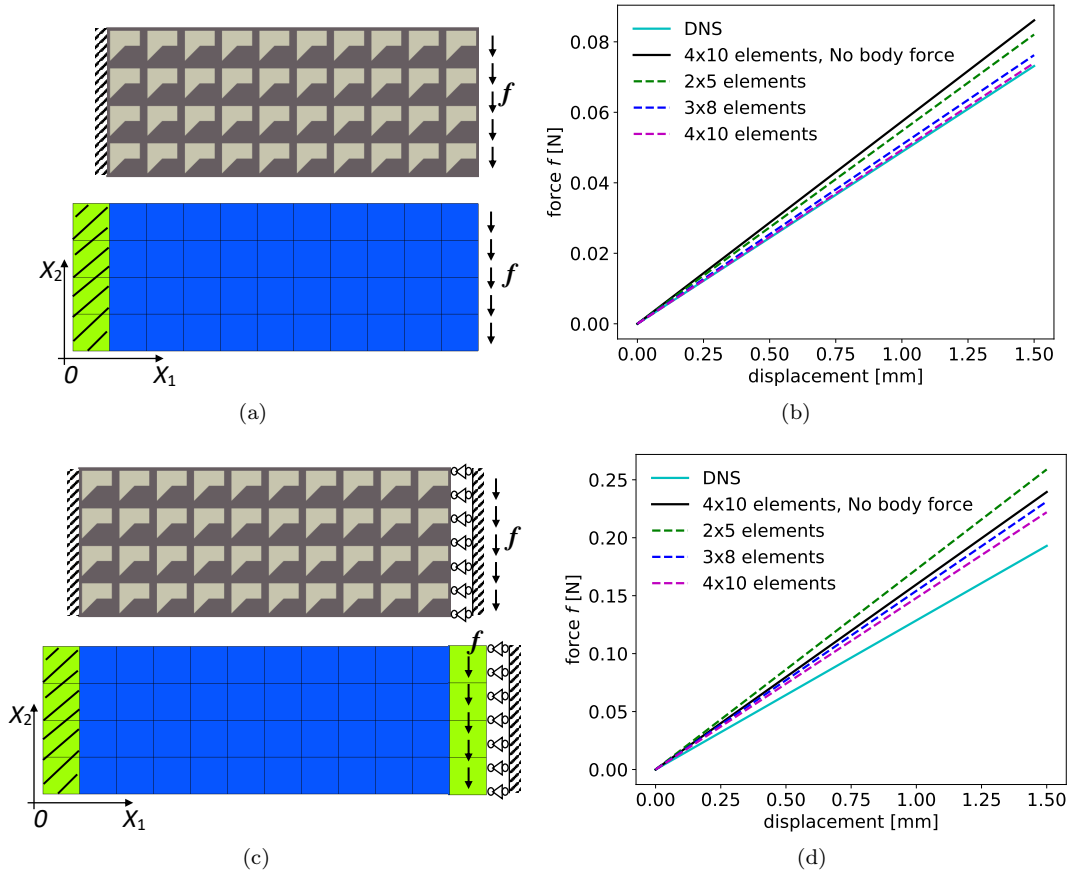
Figure 17: 2D beam consisting of 4×10 unit cells $\mathbf{C}$ – Direct numerical simulations (DNS) and different FE^2 multi-scale analyses are conducted for two kinds of boundary conditions: (a) Bending boundary conditions; (b) Force vs. displacement for the bending case; (c) Shearing boundary conditions; and (d) Force vs. displacement for shearing case.
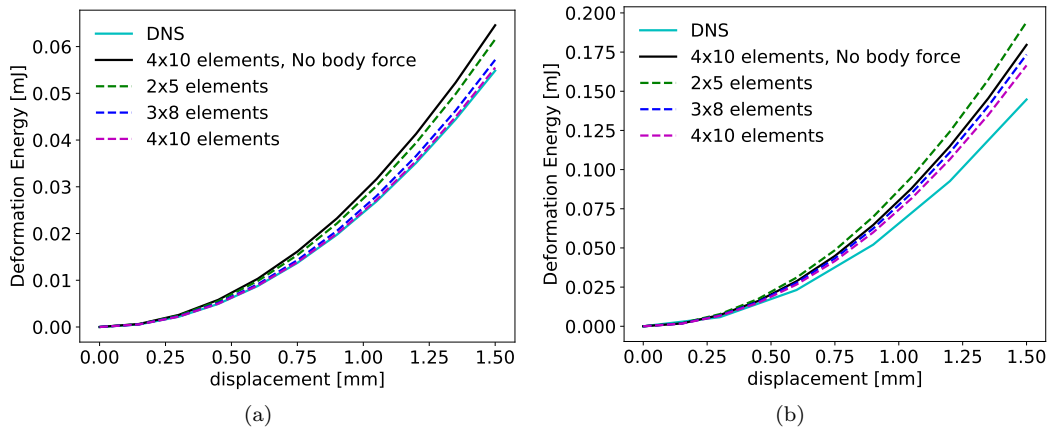

Figure 18: 2D beam consisting of 4×10 unit cells $\mathbf{C}$ – Deformation energy vs. displacement under two kinds of boundary conditions: (a) Bending boundary conditions; (b) Shearing boundary conditions.

of a heterogeneous RVE is lower, yielding structural behaviour closer to the DNS response.

26

5.4.2. Compression of a honeycomb structure
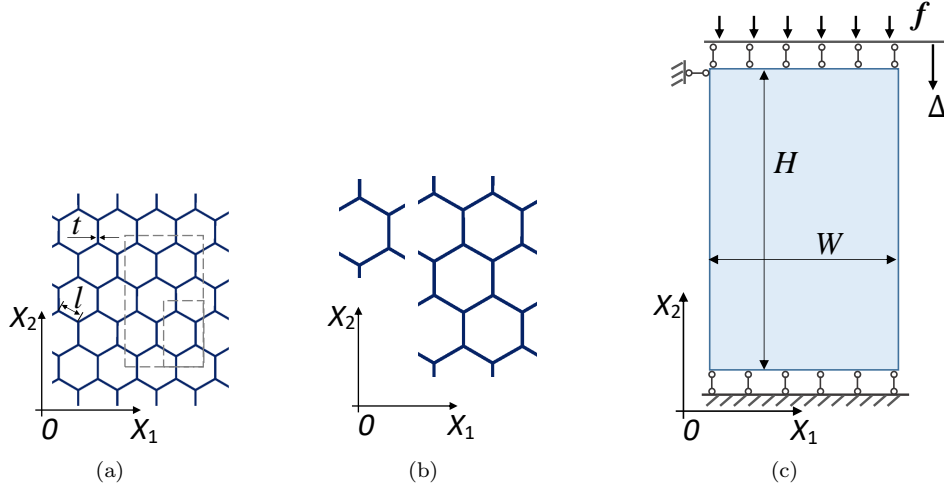
Figure 19: Honeycomb structure: (a) Hexagonal honeycomb geometry; (b) RVEs consisting of respectively 1×1 and 2×2 unit cells; and (c) Geometry and boundary conditions of a compression test.

In this section, the behaviour of a hexagonal honeycomb structure under compression is studied. The characteristic geometry of a perfect honeycomb structure is illustrated in Fig. 19(a), with the cell wall length $l = 1$ mm and the wall thickness $t = 0.1$ mm. A Voronoï tessellation is used to generate the geometry. A small random disturbance is added to each hexagonal cell by moving its centre to a random direction with a random distance within $0.01 \times l$ [37]. The wall material follows J_2-hyperelastic based elasto-plastic constitutive law, as being detailed in Appendix E. The material parameters are the initial bulk modulus $K = 67.55$ GPa, shear modulus $\mu = 25.9$ GPa, yielding stress $\tau_y^0 = 276.0$ MPa and the hardening parameter $h = 6890.0$ MPa. The macro-scale structure is under plane strain condition.
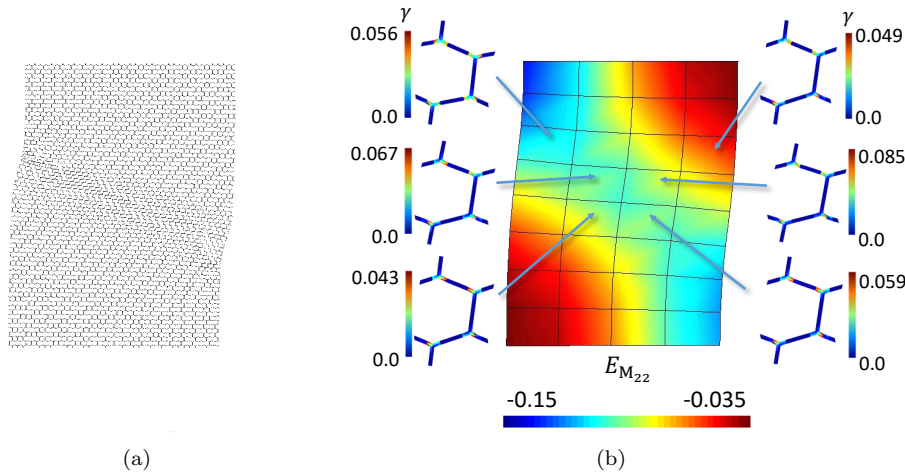

Figure 20: Compression test of a hexagonal honeycomb structure at $\Delta/H = 9\%$: (a) Deformation obtained with the direct numerical simulation; and (b) Deformation and distribution of the homogenised Green-Lagrange strain $E_{\mathrm{M}_{22}}$ at the macro-scale and deformation and distribution of the equivalent plastic stain γ at the micro-scale obtained with the multi-scale simulation.

The geometry and boundary conditions of the studied compression problem are depicted in Fig. 19(c), with $H = 102$ mm and $W = 65.8$ mm. A direct numerical simulation (DNS) of the honeycomb structure

as well as multi-scale simulations based on a second-order computational homogenisation are conducted by considering successively a mesh of 4×4 and of 8×4 quadratic quadrangles. In order to investigate the RVE size effect on the second-order computational homogenisation, two RVEs consisting of a different number of unit cells are successively considered in multi-scale simulations without and with body forces: a 1×1- and a 2×2-unit cell RVEs, see Fig. 19(b). Multi-scale simulations based on a first-order computational homogenisation are also conducted with a 1×1-unit cell RVE for the sake of comparison.
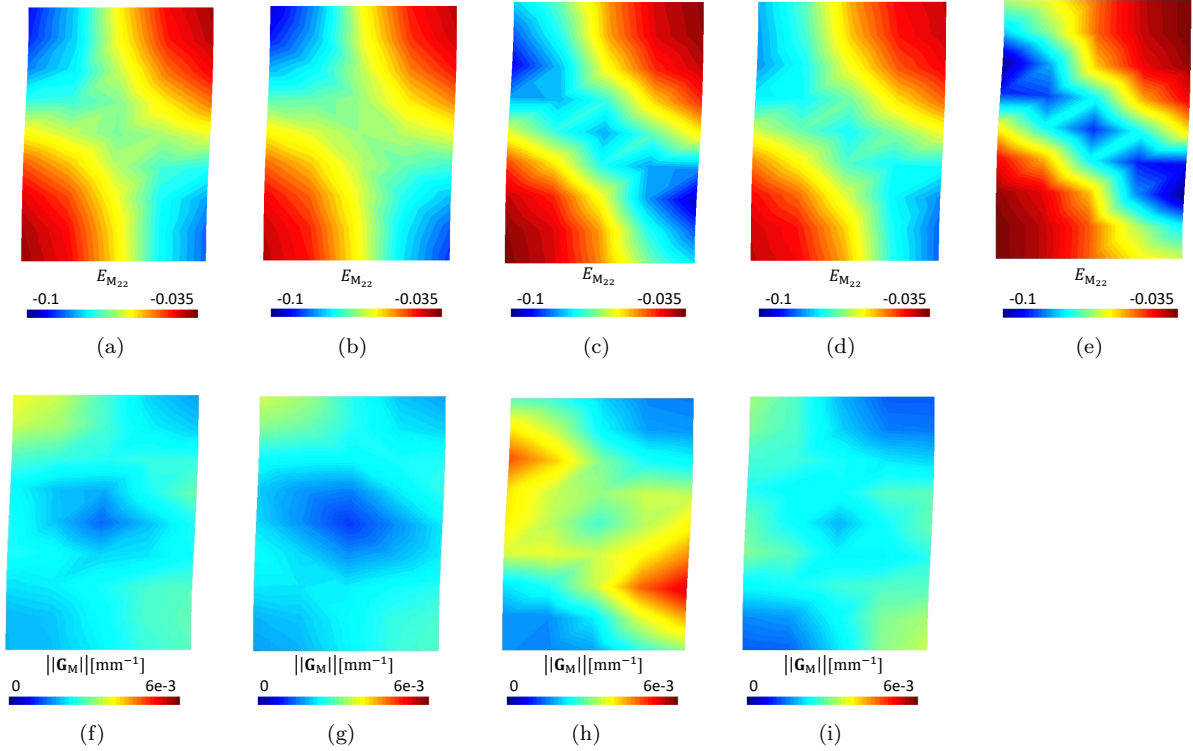

Figure 21: The predicted distributions of (a-e) the homogenised Green-Lagrange strain $E_{\mathrm{M}_{22}}$ and (g-j) the norm of the homogenised gradient of deformation gradient $\mathbf{G}_{\mathrm{M}}$ for the compression test of a hexagonal honeycomb structure after instability onset at $\Delta/H = 6.66\%$ using: (a, f) The presented method with body-force and RVEs of 1×1 unit cell; (b, g) The presented method with body-force and RVEs of 2×2 unit cells; (c, h) The second-order homogenisation without body force with RVEs of 1×1 unit cell; (d, i) The second-order homogenisation without body force with RVEs of 2×2 unit cells; and (e) The first-order homogenisation with RVEs of 1×1 unit cell.

The predicted deformation of the honeycomb structure is presented in Fig. 20(a) for the direct numerical simulation and in Fig. 20(b) for the multi-scale analysis on a macro-mesh of 8×4 elements and with body forces, in which the RVEs consisting of 1×1 unit cell are used. A good qualitative agreement is observed. The effect of the number of unit cells composing the RVE is studied in Fig. 21 by considering RVEs of 1×1 and 2×2 unit cells and a macro-mesh of 8×4 elements for both the presented computational homogenisation scheme enhanced by the body force and the original second-order homogenisation [23] without body force. The first-order computational homogenisation case is also reported for comparison purpose. When considering second-order homogenisation, the effect of the number of unit cells in the RVE on the distributions of the Green-Lagrange strain $E_{\mathrm{M}_{22}}$ and of norm of the gradient of deformation gradient $\mathbf{G}_{\mathrm{M}}$ after the instability onset can be seen clearly in Figs. 21(c), 21(h) and Figs. 21(d), 21(i) where the body force is not applied, whilst this effect is not obvious for the presented method, see Figs. 21(a), 21(f) and Figs. 21(b), 21(g). The prediction with the first-order computational homogenisation differs as it can be seen in Fig. 21(e) and exhibits a more pronounced gradient of deformation.

A quantitative analysis of the macro-mesh size and of the number of unit cells in the RVE effects, for
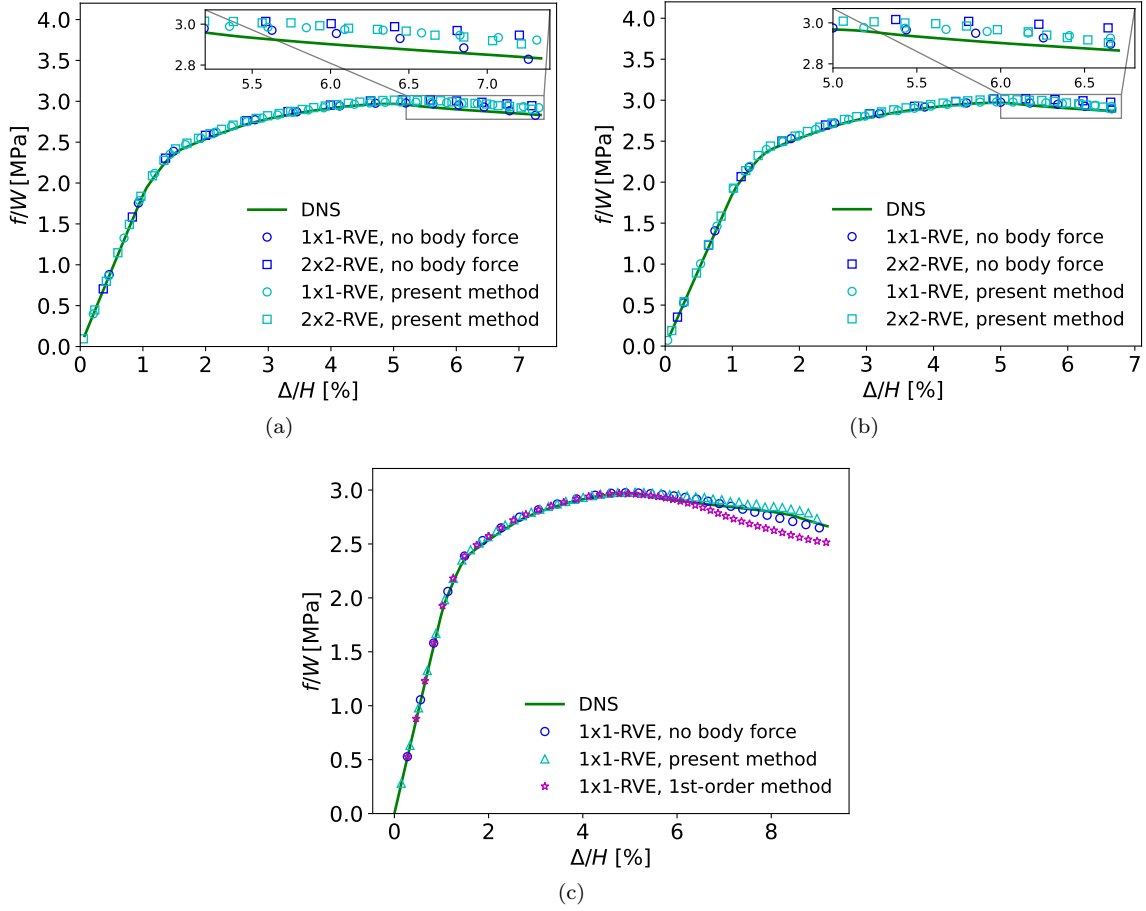
Figure 22: The vertical reaction force f/W vs. relative displacement Δ/H for the compression test of a hexagonal honeycomb structure using: (a) Effects of body force and RVE size for a macro-structure mesh of 4×4 quadratic elements; (b) Effects of body force and RVE size for a macro-structure mesh of 8×4 quadratic elements; and (c) Comparison of second-order homogenisation with first-order homogenisation for a macro-structure mesh of 8×4 quadratic elements.

both the presented computational homogenisation scheme enhanced by the body force and the original one [23] without body force, is now performed by comparing the vertical reaction force f/W vs. relative displacement Δ/H in Fig. 22. Figs. 22(a) and 22(b) show that the multi-scale simulations have converged with the macro-structure mesh size. For the original second-order computational homogenisation without body-force, the multi-scale simulations results using RVEs of 2×2 unit cells are slightly higher than when using RVEs of 1×1 unit cell, in particular during the softening stage. However, with the presented method, the difference between the results obtained by using RVEs of 1×1 or 2×2 unit cells is reduced as expected. Finally, the prediction with the first-order computational homogenisation clearly exhibits a softer behaviour than the direct numerical simulation during the post-buckling stage as it can be seen in Fig 22(c).

5.4.3. Local and global instabilities of a holed micro-structure

In this section, the patterning change of a holed structure under compression is studied. The characteristic geometry of a perfect holed structure is illustrated in Fig. 23(a), with the periodicity length $l = 9.97$ mm and hole radius $R = 4.335$ mm. A small random disturbance is added to each hole by creating ellipsoids instead of circles with a change of radius of $0.002 \times R$. The matrix hyperelastic material model corresponds to the real structural material used by Bertoldi et al. [35]. The constitutive behaviour of this elastomer
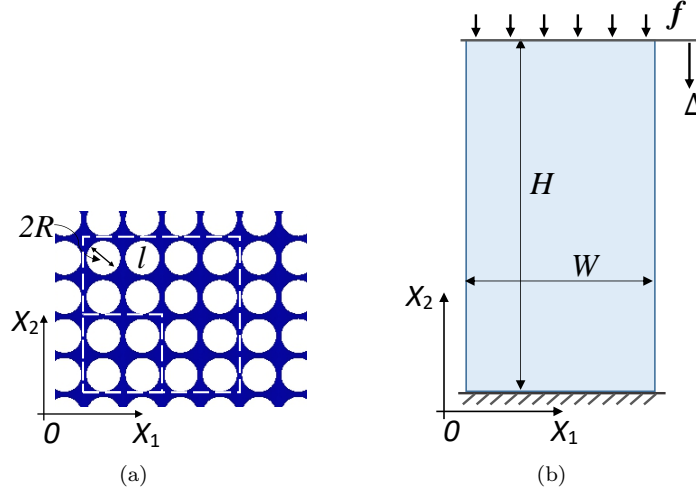
Figure 23: Holed structure: (a) Holed pattern geometry and (b) Geometry and boundary conditions of a compression test.

base material is governed by the elastic potential which reads

$$\psi(\boldsymbol{F}) = c_1(I_1 - 3) + c_2(I_1 - 3)^2 - 2c_1\log(J) + \frac{1}{2}K(J - 1)^2\,, \tag{59}$$

where $I_1 = \mathrm{tr}(\boldsymbol{C})$. The material parameters are based on the experimental characterisation conducted in [35], with $c_1 = 0.55\,\mathrm{MPa}$, $c_2 = 0.3\,\mathrm{MPa}$, $K = 55\,\mathrm{MPa}$. Specimens cut from sheets of photoelastic elastomers were experimentally tested in [35] under uni-axial compression. In order to prevent out-of-plane buckling, the experimental samples were placed between two polymethylmethacrylate plates. In this work, in order to represent the uni-axial compression, we consider 2D elements with the micro-scale (structural-scale) discretisations solved under plane stress condition for the multi-scale analyses (Direct Numerical Simulations).

The geometry and boundary conditions of the studied compression problem are depicted in Fig. 23(b), where the height is successively taken as $H = 14 \times l$ and $H = 34 \times l$, whilst $W = 6 \times l$ in all cases. This allows studying the case of local, i.e. change of patterning, and global, i.e. buckling, instabilities, respectively. The RVEs, see Fig. 23(a), consists successively in 2×2 and 4×4 unit cells in order to capture the change of patterning during the compression analysis.

A similar study was conducted in [26] with the micromorphic approach, in which the higher-scale buckling mode was enforced when the instability was detected in the macro-scale finite element stiffness. With the presented approach, buckling is triggered by the introduced geometrical imperfections, upon which the post-buckling analysis proceeds within the higher order continuum formalism.
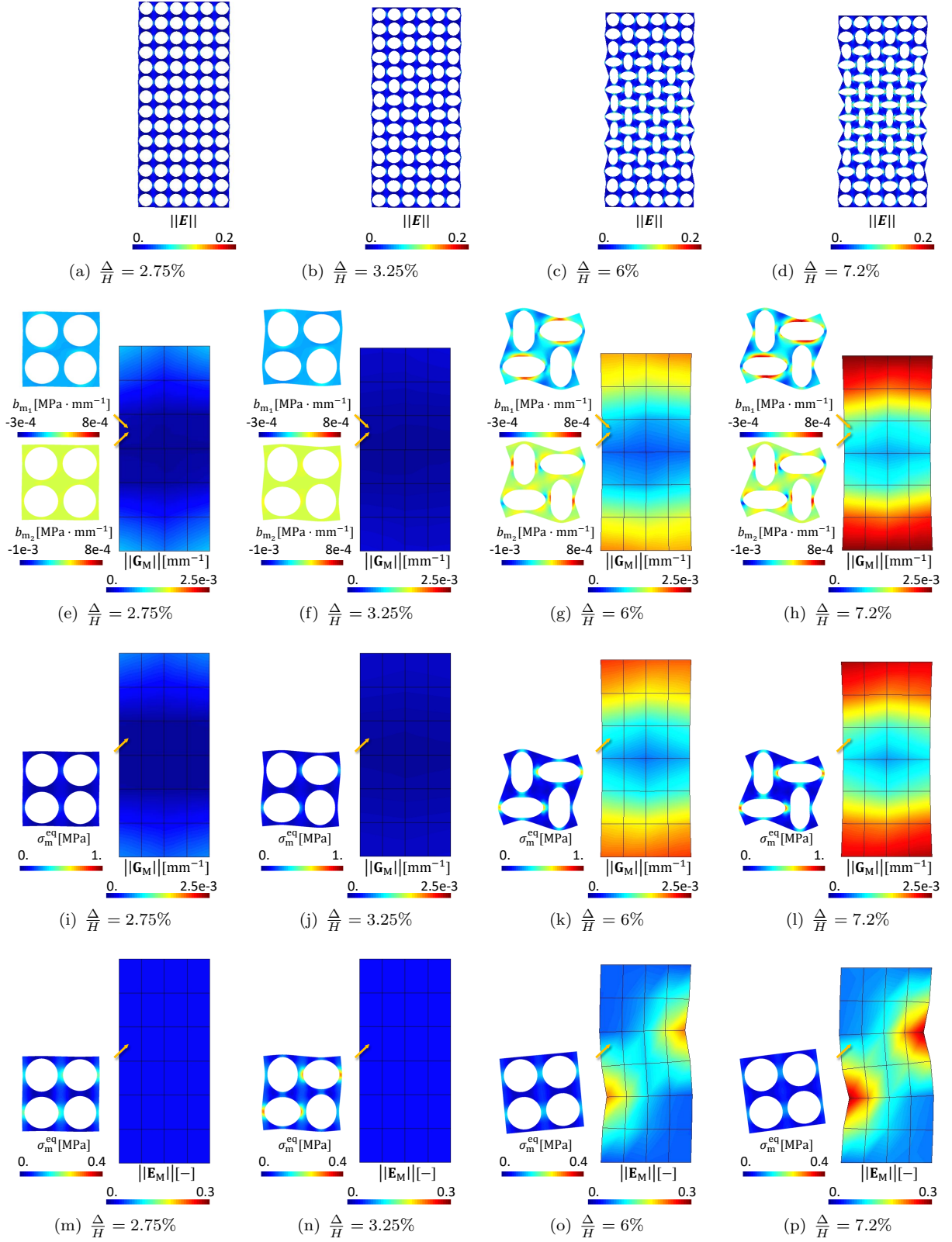
Figure 24: Compression test of a $H = 14 \times l$ holed beam considering a 2×2-unit cell RVE: (a-d) Green-Lagrange strain norm $\|\boldsymbol{E}\|$ obtained with the direct numerical simulation; (e-h) Homogenised gradient of deformation gradient norm $\mathbf{G}_M$ at the macro-scale and body force $\boldsymbol{b}_m$ at the micro-scale using the present method; (i-l) Homogenised gradient of deformation gradient norm $\mathbf{G}_M$ at the macro-scale and equivalent von Mises stress σ_m^{eq} at the micro-scale using second-order homogenisation without body force; and (m-p) Homogenised Green-Lagrange strain norm $\|\boldsymbol{E}_M\|$ at the macro-scale and equivalent von Mises stress σ_m^{eq} at the micro-scale using first-order homogenisation.
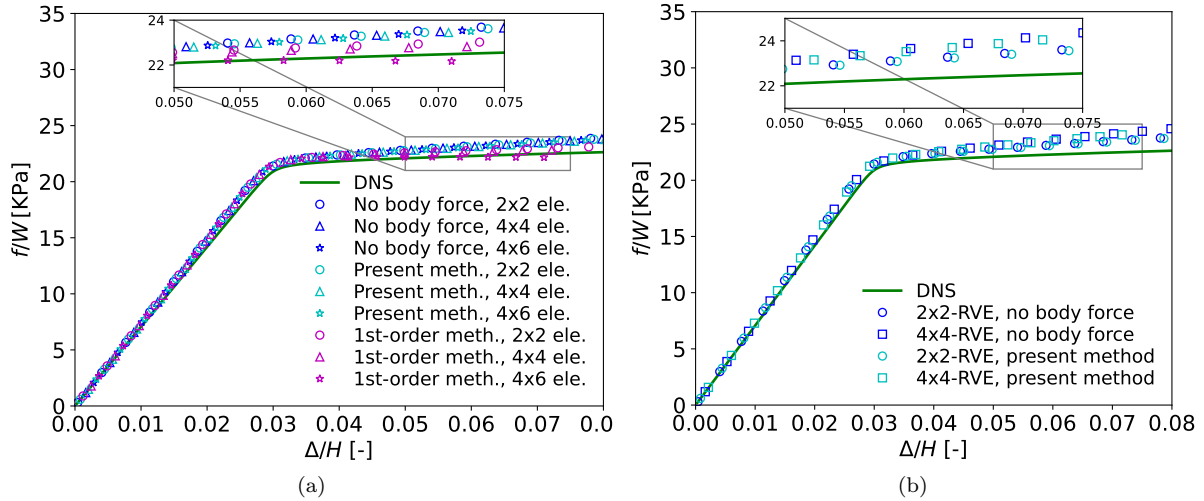
Figure 25: The vertical reaction force f/W vs. relative displacement Δ/H for the compression test of a $H = 14 \times l$ holed beam: (a) Effect of the macro-mesh size for the different first-order and second-order homogenisation methods when considering a 2×2-unit cell RVE; and (b) Effect of the RVE size for the different second-order homogenisation methods

The predicted deformations of the $H = 14 \times l$ holed beam considering a 2×2-unit cell RVE are presented in Fig. 24 for the Direct Numerical Simulations (DNS) and for different multi-scale analyses with 4×6 quadratic elements at the macro-scale: the presented method, the original second-order computational homogenisation without body-force, and the first-order computational homogenisation. On the one hand, the second-order homogenisation methods capture the instability mode predicted by the DNS, see 24(a)-24(d), with at the macro-scale the presence of a gradient of deformation gradient more pronounced before and after the instability point and a change of patterning at the micro-scale, see Figs. 24(e)-24(l). In the case of the present method, the body force components distributions are illustrated at the micro-scale, see Figs. 24(e)-24(h). On the other hand, the first-order homogenisation method cannot sustain the local instability, i.e. the change of patterning and instead predicts a S-shaped global instability, see Figs. 24(m)-24(p). The vertical reaction force f/W vs. relative displacement Δ/H curves predicted by the DNS and the computational homogenisation methods are compared in Fig. 25. The macro-scale mesh convergence is studied in Fig. 25(a) by considering successively 2×2, 4×4 and 6×4 macro-scale quadratic elements. On the one hand, the results are converged for a 4×4 macro-scale mesh when considering the second-order homogenisation schemes, although the prediction are slightly stiffer than with the direct numerical simulation because of the lack of scale separation. On the other hand the first-order homogenisation predictions do not converge with the macro-scale mesh refinement.

The effect of the RVE size when considering the second-order computational homogenisation is studied in Fig. 25(b) by considering successively a 2×2-unit cell RVE and a 4×4-unit cell RVE, successively with and without the body force. Because of the larger memory requirement with the larger RVE, a 3×3 mesh is considered at the macro-scale for this analysis. A slight size dependency is still observed when considering the body forces, although slightly lower than for the case without body force. The distributions of equivalent von Mises stress and, when existing, of the body force in the 4×4-unit cell RVE are illustrated in Fig. 26. In this application the body forces effect is limited because the structure is mostly under compression and not under bending with a limited gradient of deformation gradient and thus a limited amplitude of the body forces. Besides, the 4×4-unit cell RVE is almost as large as the structure width.

The direct numerical simulation (DNS) of the $H = 34 \times l$ holed structure as well as its multi-scale counterparts based on a second-order computational homogenisation with body forces are conducted by considering a macro-scale mesh of 8×3 quadratic quadrangles. In the case of a $H = 34 \times l$ holed beam, the mesh is perturbed to promote buckling. The multi-scale analysis can capture both local and global instabilities, including the change of patterning at the micro-scale as illustrated in Fig. 27, in which the
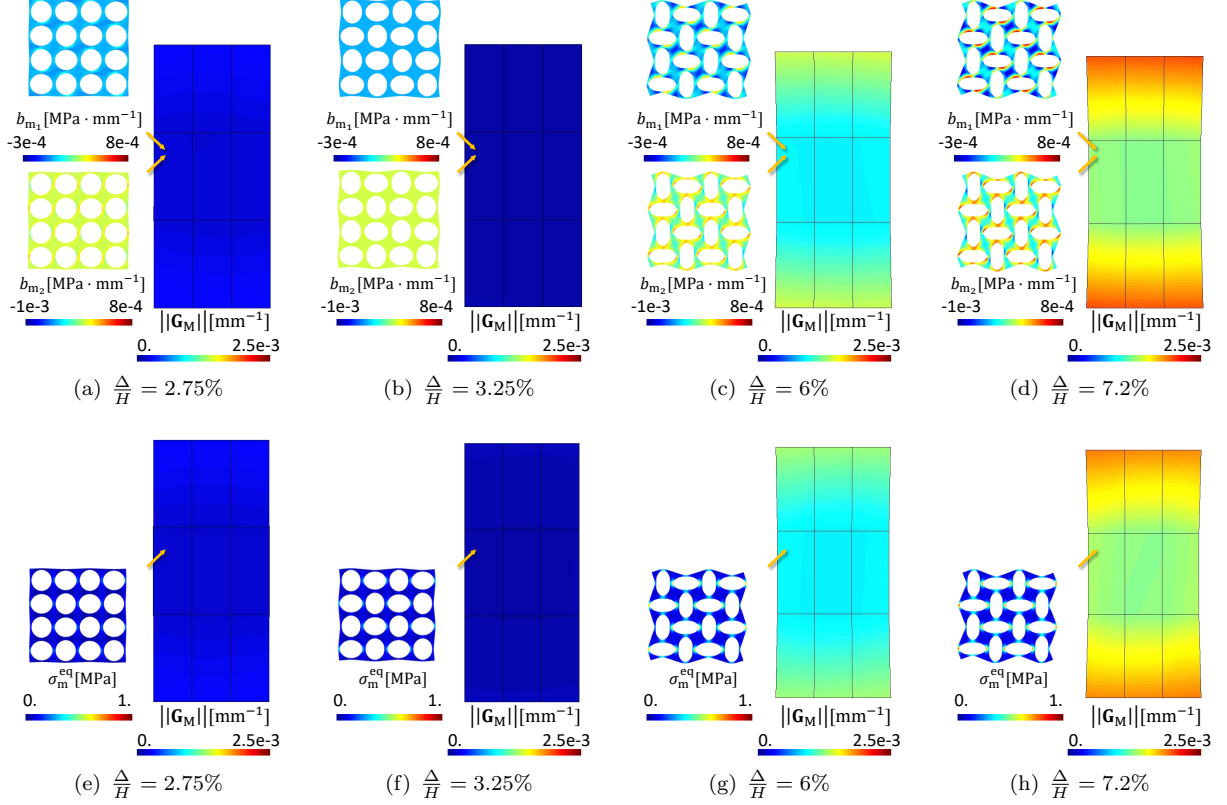
Figure 26: Compression test of a $H = 14 \times l$ holed beam considering a 4×4-unit cell RVE: (a-d) Homogenised gradient of deformation gradient norm $\mathbf{G}_M$ at the macro-scale and body force $\boldsymbol{b}_m$ at the micro-scale using the present method; and (e-h) Homogenised gradient of deformation gradient norm $\mathbf{G}_M$ at the macro-scale and equivalent von Mises stress σ_m^{eq} at the micro-scale using second-order homogenisation without body force.

distributions of the gradient of deformation gradient norm at the macro-scale and of the body force at the micro-scale are shown for the multi-scale simulation. The vertical reaction force f/W vs. relative displacement Δ/H curves predicted by the DNS and the second-order computational homogenisation with body-force are compared in Fig. 28: the second-order computational homogenisation scheme predicts the buckling initiation at a higher load but lower displacement than the DNS; it nevertheless still predicts a softening curve beyond this point.

6. Conclusions

In this work, a second-order computational homogenisation framework is proposed to model strain gradient effects in a finite deformation setting. Compared to the "classical" second-order computational homogenisation framework in [23], a supplementary constraint, which appears as a non-uniform body force, is introduced to form the microscopic boundary value problem. This extra constraint can be related to other contributions in the context of the strain gradient effect study on the RVE. On the one hand Lagrange multipliers are used as supplementary constraints in micromorphic approach in which the deformation of the micro-structure is enriched by pre-defined deformation modes [26]. On the other hand, in more general cases of microscopic deformation, a uniform body force was adopted in linear elastic structures in [21] and thick shell structure in [43]. In the presented work, the expression of the supplementary constraint arises from the definition of an equivalent volume of second-order continuum within the RVE, for general non-linear constitutive laws. The Hill-Mandel condition thus yields a non-uniform body force expression in terms of the
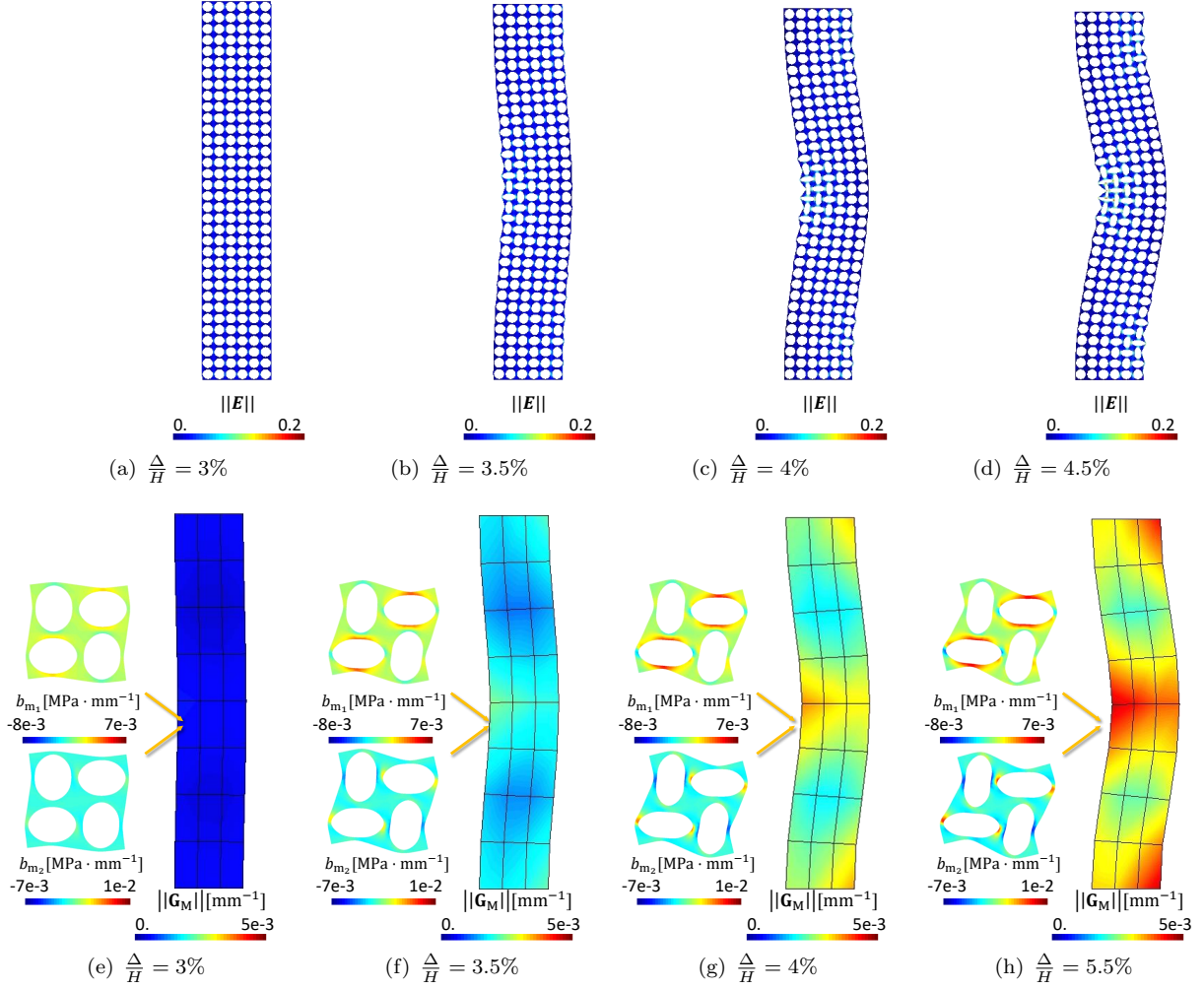
Figure 27: Compression test of a $H = 34 \times l$ holed beam considering a 2×2-unit cell RVE: (a-d) Green-Lagrange strain norm $\|\boldsymbol{E}\|$ obtained with the direct numerical simulation; and (e-h) Homogenised gradient of deformation gradient norm $\mathbf{G}_{\mathrm{M}}$ at the macro-scale and body force $\boldsymbol{b}_{\mathrm{m}}$ at the micro-scale using the present method.

local value of the strain concentration tensor $\frac{\mathrm{d}\boldsymbol{F}_{\mathrm{m}}}{\mathrm{d}\boldsymbol{F}_{\mathrm{M}}}$. This term guarantees that spurious strain-gradient effects vanish when the RVE consists in a homogeneous Cauchy medium and avoids the divergence of higher-order properties with respect to the size of RVEs.

The higher order stiffness coefficients obtained by the presented scheme were compared to that from literature for linear elastic RVEs with different shapes of inclusions, and with various contrasts of properties between matrix and inclusion materials. Then, the proposed second-order homogenisation was integrated in the enriched discontinuous Galerkin framework to carry out multi-scale analyses. In this context, first, simulations on elasto-plastic honeycomb structures under compression confirmed the elimination of macroscopic responses divergence with respect to the size of RVEs. We then simulated the compression of structures made of metamaterials and showed that the change of patterning can be captured by the presented approach.

Nevertheless, we observed that for some simulations, when buckling appears in the micro-structures, the values of the strain concentration $\frac{\mathrm{d}\boldsymbol{F}_{\mathrm{m}}}{\mathrm{d}\boldsymbol{F}_{\mathrm{M}}}$ governing the body force can change in an important way from one macroscopic loading step to another, which can lead to poor convergence of the Newton-Raphson iterations. As a conclusion, the formulation of second-order homogenisation with supplementary constraints remains an open research field and requires further studies.
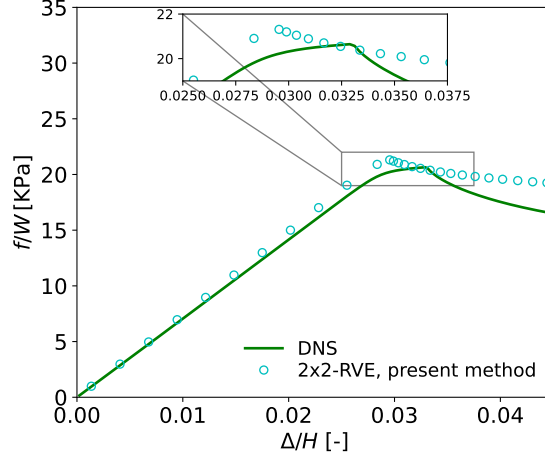
Figure 28: The vertical reaction force f/W vs. relative displacement Δ/H for the compression test of a 6×34 holed beam.

Acknowledgement

Appendix A. High order boundary condition

The volume-average of the product between Eq. (2) and $\boldsymbol{X}_{\mathrm{m}}$ reads

$$
\frac{1}{2V_{\mathrm{m0}}} \int_{\Omega_{\mathrm{m0}}} \left[\boldsymbol{F}_{\mathrm{m}} \otimes \boldsymbol{X}_{\mathrm{m}} + (\boldsymbol{F}_{\mathrm{m}} \otimes \boldsymbol{X}_{\mathrm{m}})^{\mathrm{T}_{2,3}} \right] \mathrm{d}\Omega
$$
$$
= \frac{1}{2V_{\mathrm{m0}}} \int_{\Omega_{\mathrm{m0}}} \left[\mathbf{G}_{\mathrm{M}} \cdot \boldsymbol{X}_{\mathrm{m}} \otimes \boldsymbol{X}_{\mathrm{m}} + (\mathbf{G}_{\mathrm{M}} \cdot \boldsymbol{X}_{\mathrm{m}} \otimes \boldsymbol{X}_{\mathrm{m}})^{\mathrm{T}_{2,3}} \right] \mathrm{d}\Omega +
$$
$$
\frac{1}{2V_{\mathrm{m0}}} \int_{\Omega_{\mathrm{m0}}} \left[(\boldsymbol{w} \otimes \nabla_{\mathrm{m0}}) \otimes \boldsymbol{X}_{\mathrm{m}} + ((\boldsymbol{w} \otimes \nabla_{\mathrm{m0}}) \otimes \boldsymbol{X}_{\mathrm{m}})^{\mathrm{T}_{2,3}} \right] \mathrm{d}\Omega \,. \tag{A.1}
$$

Using the definition of $\boldsymbol{F}_{\mathrm{m}} = \frac{\mathrm{d}\boldsymbol{x}_{\mathrm{m}}}{\mathrm{d}\boldsymbol{X}_{\mathrm{m}}}$, and the divergence theorem, Eq.(A.1) yields

$$
\int_{\Gamma_{\mathrm{m0}}} [\boldsymbol{x}_{\mathrm{m}} \otimes \boldsymbol{X}_{\mathrm{m}} \otimes \boldsymbol{N}_{\mathrm{m0}} + \boldsymbol{x}_{\mathrm{m}} \otimes \boldsymbol{N}_{\mathrm{m0}} \otimes \boldsymbol{X}_{\mathrm{m}}]\mathrm{d}\Gamma - 2\int_{\Omega_{\mathrm{m0}}} \boldsymbol{x}_{\mathrm{m}}\mathrm{d}\Omega \otimes \mathbf{I}
$$
$$
= \mathbf{G}_{\mathrm{M}} \cdot \int_{\Omega_{\mathrm{m0}}} \boldsymbol{X}_{\mathrm{m}} \otimes \boldsymbol{X}_{\mathrm{m}}\mathrm{d}\Omega + \left(\mathbf{G}_{\mathrm{M}} \cdot \int_{\Omega_{\mathrm{m0}}} \boldsymbol{X}_{\mathrm{m}} \otimes \boldsymbol{X}_{\mathrm{m}}\mathrm{d}\Omega \right)^{\mathrm{T}_{2,3}}
$$
$$
+ \int_{\Gamma_{\mathrm{m0}}} [\boldsymbol{w} \otimes \boldsymbol{N}_{\mathrm{m0}} \otimes \boldsymbol{X}_{\mathrm{m}} + \boldsymbol{w} \otimes \boldsymbol{X}_{\mathrm{m}} \otimes \boldsymbol{N}_{\mathrm{m0}}]\mathrm{d}\Gamma - 2\int_{\Omega_{\mathrm{m0}}} \boldsymbol{w}\mathrm{d}\Omega \otimes \mathbf{I} \,, \tag{A.2}
$$

where $\mathbf{I}$ is second-order identity tensor. By defining the geometric inertia $\boldsymbol{J}_{\mathrm{m}} = \int_{\Omega_{\mathrm{m0}}} \boldsymbol{X}_{\mathrm{m}} \otimes \boldsymbol{X}_{\mathrm{m}}\mathrm{d}\Omega$, using Eq. (4), and substituting $\boldsymbol{x}_{\mathrm{m}}$ with its expression, Eq. (1), Eq. (A.2) can be rewritten as

$$
\mathbf{G}_{\mathrm{M}} \cdot \boldsymbol{J}_{\mathrm{m}} + (\mathbf{G}_{\mathrm{M}} \cdot \boldsymbol{J}_{\mathrm{m}})^{\mathrm{T}_{2,3}} + \mathbf{G}_{\mathrm{M}} : \boldsymbol{J}_{\mathrm{m}} \otimes \mathbf{I}
$$
$$
= \int_{\Gamma_{\mathrm{m0}}} [\boldsymbol{x}_{\mathrm{m}} \otimes \boldsymbol{X}_{\mathrm{m}} \otimes \boldsymbol{N}_{\mathrm{m0}} + \boldsymbol{x}_{\mathrm{m}} \otimes \boldsymbol{N}_{\mathrm{m0}} \otimes \boldsymbol{X}_{\mathrm{m}}]\,\mathrm{d}\Gamma
$$
$$
- \int_{\Gamma_{\mathrm{m0}}} [\boldsymbol{w} \otimes \boldsymbol{N}_{\mathrm{m0}} \otimes \boldsymbol{X}_{\mathrm{m}} + \boldsymbol{w} \otimes \boldsymbol{X}_{\mathrm{m}} \otimes \boldsymbol{N}_{\mathrm{m0}}]\,\mathrm{d}\Gamma \,. \tag{A.3}
$$

Since $\mathbf{G}_\mathrm{M}$ should be independent of the fluctuation field, $\boldsymbol{w}$, the following condition arises

$$\int_{\Gamma_\mathrm{m0}} \left[\boldsymbol{w} \otimes \boldsymbol{N}_\mathrm{m0} \otimes \boldsymbol{X}_\mathrm{m} + \boldsymbol{w} \otimes \boldsymbol{X}_\mathrm{m} \otimes \boldsymbol{N}_\mathrm{m0} \right] \mathrm{d}\Gamma = \mathbf{0}. \tag{A.4}$$

Appendix B. Path following iterative resolution

Beside the displacements vector $\mathbf{u}_\mathrm{m}$, a load parameter μ is applied in a path following strategy. In an incremental process, the displacement and load parameter are known at previous time step, $[\mathbf{u}_{\mathrm{m}n}, \mu_n]$, and the values at the present step $[\mathbf{u}_{\mathrm{m}n+1}, \mu_{n+1}]$ are determined by finding their increments $[\Delta\mathbf{u}_\mathrm{m}, \Delta\mu]$, such that

$$\begin{aligned} \mathbf{u}_{\mathrm{m}n+1} &= \mathbf{u}_{\mathrm{m}n} + \Delta\mathbf{u}_\mathrm{m} \quad \text{and} & (\mathrm{B.1}) \\ \mu_{n+1} &= \mu_n + \Delta\mu, & (\mathrm{B.2}) \end{aligned}$$

for each arc-length increment ΔL which can be approximated by

$$\Delta L = \sqrt{\frac{\Delta\mathbf{u}_\mathrm{m}^\mathrm{T}\Delta\mathbf{u}_\mathrm{m}}{\Psi^2} + \Delta\mu^2}, \tag{B.3}$$

where Ψ is a constant parameter used to yield a dimensionless equation since the dimensions of $\Delta\mathbf{u}_\mathrm{m}$ and $\Delta\mu$ are different. The value of Ψ is set at the beginning of the computation to an arbitrary value, which has the same magnitude as the displacement solution. The arc-length increment (B.3) leads to a quadratic constraint

$$h\left(\Delta\mathbf{u}_\mathrm{m}, \Delta\mu\right) = \frac{\Delta\mathbf{u}_\mathrm{m}^\mathrm{T}\Delta\mathbf{u}_\mathrm{m}}{\Psi^2} + \Delta\mu^2 - \Delta L^2 = 0. \tag{B.4}$$

The equilibrium equation under linear constraints reads

$$\mathbf{f}_\mathrm{m} - \mathbf{b}_\mathrm{m} = \mathbf{0} \quad \text{subjected to} \quad \mathcal{C}\mathbf{u}_\mathrm{m} - \mathbf{g} = \mathbf{0}, \tag{B.5}$$

where $\mathbf{g} = \mathcal{S}\mathcal{K}_\mathrm{M}^u$. Using the load parameter, the constraints vector $\mathbf{g}$ is rewritten as

$$\mathbf{g} = \mathbf{g}_0 + \mathbf{q}\Delta\mu = \mathcal{S}\mathcal{K}_{\mathrm{M}n}^u + \mathbf{q}\Delta\mu, \quad \text{with} \quad \mathbf{q} = \frac{\partial\mathbf{g}}{\partial\mu}. \tag{B.6}$$

The non-linear system (B.5) is solved iteratively and is linearised in terms of the increments of displacement vector, $\Delta\mathbf{u}_\mathrm{m}$ and load parameter, $\Delta\mu$, yielding

$$\begin{cases} \mathbf{r} + \mathbf{K}_\mathrm{B}\Delta\mathbf{u}_\mathrm{m} - \mathcal{B}\Delta\mu = \mathbf{0}, \quad \text{with} \quad \mathbf{K}_\mathrm{B} = \frac{\partial(\mathbf{f}_\mathrm{m}-\mathbf{b}_\mathrm{m})}{\partial\mathbf{u}_\mathrm{m}} \text{ and } \mathcal{B} = \frac{\partial\mathbf{b}_\mathrm{m}}{\partial\mu}, \\ \text{subjected to} \quad \mathbf{r}_\mathrm{c} + \mathcal{C}\Delta\mathbf{u}_\mathrm{m} - \mathbf{q}\Delta\mu = \mathbf{0}, \end{cases} \tag{B.7}$$

where $\mathbf{r}$ and $\mathbf{r}_\mathrm{c}$ are the force residual and constraints residual vectors of the system (B.5), respectively. We rearrange the terms of the system (B.7), yielding

$$\begin{cases} \mathbf{K}_\mathrm{B}\Delta\mathbf{u}_\mathrm{m} = \mathcal{B}\Delta\mu - \mathbf{r}, \\ \text{subjected to} \quad \mathcal{C}\Delta\mathbf{u}_\mathrm{m} - (\mathbf{q}\Delta\mu - \mathbf{r}_\mathrm{c}) = \mathbf{0}. \end{cases} \tag{B.8}$$

Using the method presented in [42] leads to an equivalent form of the linearised system (B.8), which reads

$$\left[\mathcal{C}^\mathrm{T}\mathcal{C} + \mathbf{Q}^\mathrm{T}\mathbf{K}_\mathrm{B}\mathbf{Q}\right]\Delta\mathbf{u}_\mathrm{m} = \left[\mathcal{C}^\mathrm{T} - \mathbf{Q}^\mathrm{T}\mathbf{K}_\mathrm{B}\mathbf{R}\right]\left[\mathbf{q}\Delta\mu - \mathbf{r}_\mathrm{c}\right] + \mathbf{Q}^\mathrm{T}\left[\mathcal{B}\Delta\mu - \mathbf{r}\right], \tag{B.9}$$

where $\mathbf{R}^\mathrm{T} = (\mathcal{C}\mathcal{C}^\mathrm{T})^{-1}\mathcal{C}$ and $\mathbf{Q}^\mathrm{T} = \mathbf{I} - (\mathbf{R}\mathcal{C})^\mathrm{T}$. The system (B.9) simplifies as

$$\begin{aligned} \tilde{\mathbf{K}}\Delta\mathbf{u}_\mathrm{m} &= \tilde{\mathbf{q}}\Delta\mu - \tilde{\mathbf{r}}, & (\mathrm{B.10}) \\ \tilde{\mathbf{K}} &= \mathcal{C}^\mathrm{T}\mathcal{C} + \mathbf{Q}^\mathrm{T}\mathbf{K}_\mathrm{B}\mathbf{Q}, & (\mathrm{B.11}) \\ \tilde{\mathbf{q}} &= \left[\mathcal{C}^\mathrm{T} - \mathbf{Q}^\mathrm{T}\mathbf{K}_\mathrm{B}\mathbf{R}\right]\mathbf{q} + \mathbf{Q}^\mathrm{T}\mathcal{B}, \text{ and} & (\mathrm{B.12}) \\ \tilde{\mathbf{r}} &= \mathbf{Q}^\mathrm{T}\mathbf{r} + \left[\mathcal{C}^\mathrm{T} - \mathbf{Q}^\mathrm{T}\mathbf{K}_\mathrm{B}\mathbf{R}\right]\mathbf{r}_\mathrm{c}. & (\mathrm{B.13}) \end{aligned}$$

During one arc-length step $[n, n+1]$, the system is solved following a predictor-corrector scheme:

- Predictor step, iteration $k = 0$:
  The residual $\tilde{\mathbf{r}}$ is first linearised around the converged solution at the arc-length increment as

$$\tilde{\mathbf{r}} = -\tilde{\mathbf{K}}\Delta\mathbf{u}_\mathrm{m} + \tilde{\mathbf{q}}\Delta\mu = \mathbf{0}\,, \tag{B.14}$$

which yields $\Delta\mathbf{u}_\mathrm{m} = \mathbf{v}\Delta\mu$ with $\mathbf{v} = \tilde{\mathbf{K}}^{-1}\tilde{\mathbf{q}}$. Using the arc-length constraints of Eq. (B.3), the increment $\Delta\mu$ can be computed by equation

$$\left(\frac{\mathbf{v}^\mathrm{T}\mathbf{v}}{\Psi^2} + 1\right)\Delta\mu^2 = \Delta L^2\,, \tag{B.15}$$

which has two possible solutions

$$\Delta\mu = \pm\frac{\Delta L}{\sqrt{A}}, \ \text{with } A = \frac{\mathbf{v}^\mathrm{T}\mathbf{v}}{\Psi^2} + 1\,. \tag{B.16}$$

The increment $\Delta\mu$ takes one of two possible solutions following

$$\begin{cases} \Delta\mu = \frac{\Delta L}{\sqrt{A}} & \text{if } \mathbf{v}^\mathrm{T}\Delta\mathbf{u}_{\mathrm{m}n} \geq 0\,, \\ \Delta\mu = -\frac{\Delta L}{\sqrt{A}} & \text{if } \mathbf{v}^\mathrm{T}\Delta\mathbf{u}_{\mathrm{m}n} < 0\,, \end{cases} \tag{B.17}$$

where $\Delta\mathbf{u}_{\mathrm{m}n}$ is the displacement increment solution at the previous arc-length increment.

- Convergence check: The residual is evaluated through Eqs. (B.5) and (B.13), and the convergence criterion is defined by

$$\epsilon = \frac{\|\tilde{\mathbf{r}}\|}{\|\mathbf{f}_\mathrm{m}^{k=0} - \mathbf{b}_\mathrm{m}^{k=0}\|} < \text{Tolerance}\,. \tag{B.18}$$

If this criterion is satisfied, the simulation enters the next arc-length increment, else the correction step is applied.

- Correction step, iteration $k \leftarrow k + 1$: The residual $\tilde{\mathbf{r}}$ is linearised in terms of the increments $\delta\mathbf{u}_\mathrm{m}$ and $\delta\mu$ yielding

$$\begin{aligned} \tilde{\mathbf{r}}(\Delta\mathbf{u}_\mathrm{m} + \delta\mathbf{u}_\mathrm{m},\ \Delta\mu + \delta\mu) &= \tilde{\mathbf{r}}^k(\Delta\mathbf{u}_\mathrm{m},\ \Delta\mu) + \tilde{\mathbf{K}}^k(\Delta\mathbf{u}_\mathrm{m},\ \Delta\mu)\delta\mathbf{u}_\mathrm{m} - \\ &\quad \tilde{\mathbf{q}}^k(\Delta\mathbf{u}_\mathrm{m},\ \Delta\mu)\delta\mu = \mathbf{0}\,. \end{aligned} \tag{B.19}$$

Eventually, Eq.(B.19) leads to

$$\delta\mathbf{u}_\mathrm{m} = \mathbf{v}^k\delta\mu + \mathbf{d}_\mathrm{r}^k\,, \tag{B.20}$$

with $\mathbf{v}^k = (\tilde{\mathbf{K}}^k)^{-1}\tilde{\mathbf{q}}^k$ and $\mathbf{d}_\mathrm{r}^k = -(\tilde{\mathbf{K}}^k)^{-1}\tilde{\mathbf{r}}^k$. The arc-length constraint $h(\Delta\mathbf{u}_\mathrm{m} + \delta\mathbf{u}_\mathrm{m},\ \Delta\mu + \delta\mu) = 0$, Eq. (B.4), leads to a quadratic equation in $\delta\mu$,

$$A(\delta\mu)^2 + B\delta\mu + C = 0\,, \tag{B.21}$$

where

$$A = \frac{(\mathbf{v}^k)^\mathrm{T}\mathbf{v}^k}{\Psi^2} + 1\,, \tag{B.22}$$

$$B = 2\left[\Delta\mu + \frac{(\mathbf{v}^k)^\mathrm{T}(\mathbf{d}_\mathrm{r}^k + \Delta\mathbf{u}_\mathrm{m})}{\Psi^2}\right] \text{ and} \tag{B.23}$$

$$C = \frac{(\Delta\mathbf{u}_\mathrm{m} + \mathbf{d}_\mathrm{r}^k)^\mathrm{T}(\Delta\mathbf{u}_\mathrm{m} + \mathbf{d}_\mathrm{r}^k)}{\Psi^2} + \Delta\mu^2 - \Delta L^2\,. \tag{B.24}$$

The two roots of Eq. (B.21) are

$$\gamma_{1,2} = \frac{-B \pm \sqrt{B^2 - 4AC}}{2A}\,, \tag{B.25}$$

and the correction $\delta\mu$ takes one of the two solutions

$$
\begin{cases}
\delta\mu = \gamma_1 & \text{if } (\Delta\mathbf{u}_{\mathrm{m}})^{\mathrm{T}} \left(\gamma_2 \mathbf{v}^k + \mathbf{d}_{\mathrm{r}}^k \right) \leq (\Delta\mathbf{u}_{\mathrm{m}})^{\mathrm{T}} \left(\gamma_1 \mathbf{v}^k + \mathbf{d}_{\mathrm{r}}^k \right), \\
\delta\mu = \gamma_2 & \text{if } (\Delta\mathbf{u}_{\mathrm{m}})^{\mathrm{T}} \left(\gamma_1 \mathbf{v}^k + \mathbf{d}_{\mathrm{r}}^k \right) < (\Delta\mathbf{u}_{\mathrm{m}})^{\mathrm{T}} \left(\gamma_2 \mathbf{v}^k + \mathbf{d}_{\mathrm{r}}^k \right).
\end{cases}
\tag{B.26}
$$

The displacement and constraint increments are then updated with the correction values

$$
\begin{cases}
\Delta\mathbf{u}_{\mathrm{m}} \leftarrow \Delta\mathbf{u}_{\mathrm{m}} + \delta\mathbf{u}_{\mathrm{m}}, \\
\Delta\mu \leftarrow \Delta\mu + \delta\mu,
\end{cases}
\tag{B.27}
$$

and one can go back to the convergence check.

Appendix C. Expansion of the derivatives involved in the macroscopic tangent operators

Appendix C.1. Derivatives of the body forces

Using expression (47), the derivatives of the body force terms, $\boldsymbol{b}_{\mathrm{m}} \otimes \boldsymbol{X}_{\mathrm{m}}$ and $\boldsymbol{b}_{\mathrm{m}} \otimes \boldsymbol{X}_{\mathrm{m}} \otimes \boldsymbol{X}_{\mathrm{m}}$, read respectively

$$
\left[\frac{\partial (\boldsymbol{b}_{\mathrm{m}} \otimes \boldsymbol{X}_{\mathrm{m}})}{\partial \boldsymbol{F}_{\mathrm{m}}} \right]_{iJkL}^{(t+1)} = - \left[\frac{\partial^2 \boldsymbol{P}_{\mathrm{m}}}{\partial \boldsymbol{F}_{\mathrm{m}}^2} \right]_{iRpQkL} \left[\frac{\partial \boldsymbol{F}_{\mathrm{m}}}{\partial \boldsymbol{F}_{\mathrm{M}}} \right]_{pQmN}^{(t)} G_{\mathrm{M}mNR} X_{\mathrm{m}J},
\tag{C.1}
$$

and

$$
\begin{aligned}
\left[\frac{\partial (\boldsymbol{b}_{\mathrm{m}} \otimes \boldsymbol{X}_{\mathrm{m}} \otimes \boldsymbol{X}_{\mathrm{m}})}{\partial \boldsymbol{F}_{\mathrm{m}}} \right]_{iJOkL}^{(t+1)} = \ & - \left[\frac{\partial^2 \boldsymbol{P}_{\mathrm{m}}}{\partial \boldsymbol{F}_{\mathrm{m}}^2} \right]_{iRpQkL} \left[\frac{\partial \boldsymbol{F}_{\mathrm{m}}}{\partial \boldsymbol{F}_{\mathrm{M}}} \right]_{pQmN}^{(t)} \\
& G_{\mathrm{M}mNR} X_{\mathrm{m}J} X_{\mathrm{m}O}.
\end{aligned}
\tag{C.2}
$$

When using the approximation (48), these derivatives vanish,

$$
\frac{\partial (\boldsymbol{b}_{\mathrm{m}} \otimes \boldsymbol{X}_{\mathrm{m}})}{\partial \boldsymbol{F}_{\mathrm{m}}} = \mathbf{0}, \quad \frac{\partial (\boldsymbol{b}_{\mathrm{m}} \otimes \boldsymbol{X}_{\mathrm{m}} \otimes \boldsymbol{X}_{\mathrm{m}})}{\partial \boldsymbol{F}_{\mathrm{m}}} = \mathbf{0}.
\tag{C.3}
$$

According to the expression of the microscopic body force (30), the derivatives of body force terms with respect to $\mathbf{G}_{\mathrm{M}}$, in Eqs. (51) and (53), read

$$
\left[\frac{\partial (\boldsymbol{b}_{\mathrm{m}} \otimes \boldsymbol{X}_{\mathrm{m}})}{\partial \mathbf{G}_{\mathrm{M}}} \right]_{iJkLS} = -\frac{1}{2} \left\{ \left[\frac{\partial \boldsymbol{P}_{\mathrm{m}}}{\partial \boldsymbol{F}_{\mathrm{m}}} \frac{\partial \boldsymbol{F}_{\mathrm{m}}}{\partial \boldsymbol{F}_{\mathrm{M}}} \right]_{iSkL} + \left[\frac{\partial \boldsymbol{P}_{\mathrm{m}}}{\partial \boldsymbol{F}_{\mathrm{m}}} \frac{\partial \boldsymbol{F}_{\mathrm{m}}}{\partial \boldsymbol{F}_{\mathrm{M}}} \right]_{iLkS} \right\} X_{\mathrm{m}J},
\tag{C.4}
$$

and

$$
\left[\frac{\partial (\boldsymbol{b}_{\mathrm{m}} \otimes \boldsymbol{X}_{\mathrm{m}} \otimes \boldsymbol{X}_{\mathrm{m}})}{\partial \mathbf{G}_{\mathrm{M}}} \right]_{iJOkLS} = -\frac{1}{2} \left\{ \left[\frac{\partial \boldsymbol{P}_{\mathrm{m}}}{\partial \boldsymbol{F}_{\mathrm{m}}} \frac{\partial \boldsymbol{F}_{\mathrm{m}}}{\partial \boldsymbol{F}_{\mathrm{M}}} \right]_{iLkS} + \left[\frac{\partial \boldsymbol{P}_{\mathrm{m}}}{\partial \boldsymbol{F}_{\mathrm{m}}} \frac{\partial \boldsymbol{F}_{\mathrm{m}}}{\partial \boldsymbol{F}_{\mathrm{M}}} \right]_{iSkL} \right\} X_{\mathrm{m}J} X_{\mathrm{m}O}.
\tag{C.5}
$$

Appendix C.2. Derivatives of the stress correction terms

The derivatives in Eqs. (52-53) are further expanded as

$$
\begin{aligned}
& \left[\frac{\partial}{\partial \boldsymbol{F}_{\mathrm{M}}} \left(\frac{\partial \boldsymbol{P}_{\mathrm{M}}}{\partial \boldsymbol{F}_{\mathrm{M}}} : \mathbf{G}_{\mathrm{M}} \cdot \boldsymbol{J}_{\mathrm{M}} + \left(\frac{\partial \boldsymbol{P}_{\mathrm{M}}}{\partial \boldsymbol{F}_{\mathrm{M}}} : \mathbf{G}_{\mathrm{M}} \cdot \boldsymbol{J}_{\mathrm{M}} \right)^{\mathrm{T}_{2,3}} \right) \right]_{iJSkL} = \\
& \left[\frac{\partial^2 \boldsymbol{P}_{\mathrm{M}}}{\partial (\boldsymbol{F}_{\mathrm{M}})^2} \right]_{iJpQkL} G_{\mathrm{M}pQR} J_{\mathrm{M}RS} + \left[\frac{\partial^2 \boldsymbol{P}_{\mathrm{M}}}{\partial (\boldsymbol{F}_{\mathrm{M}})^2} \right]_{iSpQkL} G_{\mathrm{M}pQR} J_{\mathrm{M}RJ},
\end{aligned}
\tag{C.6}
$$

and

$$
\left[\frac{\partial}{\partial \mathbf{G}_\mathrm{M}} \left(\frac{\partial \boldsymbol{P}_\mathrm{M}}{\partial \boldsymbol{F}_\mathrm{M}} : \mathbf{G}_\mathrm{M} \cdot \boldsymbol{J}_\mathrm{M} + \left(\frac{\partial \boldsymbol{P}_\mathrm{M}}{\partial \boldsymbol{F}_\mathrm{M}} : \mathbf{G}_\mathrm{M} \cdot \boldsymbol{J}_\mathrm{M} \right)^{\mathrm{T}_{2,3}} \right) \right]_{iJSkLO} =
$$

$$
\left[\frac{\partial^2 \boldsymbol{P}_\mathrm{M}}{\partial \boldsymbol{F}_\mathrm{M} \partial \mathbf{G}_\mathrm{M}} \right]_{iJpQkLO} G_{\mathrm{M}pQR} J_{MRS} + \left[\frac{\partial^2 \boldsymbol{P}_\mathrm{M}}{\partial \boldsymbol{F}_\mathrm{M} \partial \mathbf{G}_\mathrm{M}} \right]_{iSpQkLO} G_{\mathrm{M}pQR} J_{MRJ}
$$

$$
+ \frac{1}{2} \left[\frac{\partial \boldsymbol{P}_\mathrm{M}}{\partial \boldsymbol{F}_\mathrm{M}} \right]_{iJkL} J_{MOS} + \frac{1}{2} \left[\frac{\partial \boldsymbol{P}_\mathrm{M}}{\partial \boldsymbol{F}_\mathrm{M}} \right]_{iJkO} J_{MLS} +
$$

$$
\frac{1}{2} \left[\frac{\partial \boldsymbol{P}_\mathrm{M}}{\partial \boldsymbol{F}_\mathrm{M}} \right]_{iSkL} J_{MOJ} + \frac{1}{2} \left[\frac{\partial \boldsymbol{P}_\mathrm{M}}{\partial \boldsymbol{F}_\mathrm{M}} \right]_{iSkO} J_{MLJ} , \tag{C.7}
$$

The homogenised stress derivatives in Eqs. (C.6) and (C.7) can be further extended as

$$
\frac{\partial^2 \boldsymbol{P}_\mathrm{M}}{\partial (\boldsymbol{F}_\mathrm{M})^2} = \frac{1}{V_0} \int_{\Omega_{\mathrm{m}0}} \left(\frac{\partial^2 \boldsymbol{P}_\mathrm{m}}{\partial \boldsymbol{F}_\mathrm{m}^2} - \frac{\partial^2 (\boldsymbol{b}_\mathrm{m} \otimes \boldsymbol{X}_\mathrm{m})}{\partial \boldsymbol{F}_\mathrm{m}^2} \right) :: \left(\frac{\partial \boldsymbol{F}_\mathrm{m}}{\partial \boldsymbol{F}_\mathrm{M}} \otimes \frac{\partial \boldsymbol{F}_\mathrm{m}}{\partial \boldsymbol{F}_\mathrm{M}} \right) \mathrm{d}\Omega +
$$

$$
\frac{1}{V_0} \int_{\Omega_{\mathrm{m}0}} \left(\frac{\partial \boldsymbol{P}_\mathrm{m}}{\partial \boldsymbol{F}_\mathrm{m}} - \frac{\partial (\boldsymbol{b}_\mathrm{m} \otimes \boldsymbol{X}_\mathrm{m})}{\partial \boldsymbol{F}_\mathrm{m}} \right) : \frac{\partial^2 \boldsymbol{F}_\mathrm{m}}{\partial \boldsymbol{F}_\mathrm{M}^2} \mathrm{d}\Omega , \tag{C.8}
$$

and

$$
\frac{\partial^2 \boldsymbol{P}_\mathrm{M}}{\partial \boldsymbol{F}_\mathrm{M} \partial \mathbf{G}_\mathrm{M}} = \frac{1}{V_0} \int_{\Omega_{\mathrm{m}0}} \left(\frac{\partial^2 \boldsymbol{P}_\mathrm{m}}{\partial \boldsymbol{F}_\mathrm{m}^2} - \frac{\partial^2 (\boldsymbol{b}_\mathrm{m} \otimes \boldsymbol{X}_\mathrm{m})}{\partial \boldsymbol{F}_\mathrm{m}^2} \right) :: \left(\frac{\partial \boldsymbol{F}_\mathrm{m}}{\partial \boldsymbol{F}_\mathrm{M}} \otimes \frac{\partial \boldsymbol{F}_\mathrm{m}}{\partial \mathbf{G}_\mathrm{M}} \right) \mathrm{d}\Omega +
$$

$$
\frac{1}{V_0} \int_{\Omega_{\mathrm{m}0}} \left(\frac{\partial \boldsymbol{P}_\mathrm{m}}{\partial \boldsymbol{F}_\mathrm{m}} - \frac{\partial (\boldsymbol{b}_\mathrm{m} \otimes \boldsymbol{X}_\mathrm{m})}{\partial \boldsymbol{F}_\mathrm{m}} \right) : \frac{\partial^2 \boldsymbol{F}_\mathrm{m}}{\partial \boldsymbol{F}_\mathrm{M} \partial \mathbf{G}_\mathrm{M}} \mathrm{d}\Omega -
$$

$$
\frac{1}{V_0} \int_{\Omega_{\mathrm{m}0}} \left(\frac{\partial^2 (\boldsymbol{b}_\mathrm{m} \otimes \boldsymbol{X}_\mathrm{m})}{\partial \mathbf{G}_\mathrm{M} \partial \boldsymbol{F}_\mathrm{m}} \right) : \frac{\partial \boldsymbol{F}_\mathrm{m}}{\partial \boldsymbol{F}_\mathrm{M}} \mathrm{d}\Omega . \tag{C.9}
$$

However, $\frac{\partial^2 \boldsymbol{F}_\mathrm{m}}{\partial \boldsymbol{F}_\mathrm{M}^2}$ and $\frac{\partial^2 \boldsymbol{F}_\mathrm{m}}{\partial \boldsymbol{F}_\mathrm{M} \partial \mathbf{G}_\mathrm{M}}$ cannot be computed during one RVE resolution. Therefore, the same approximations as the ones used when evaluating the body forces, Eqs. (47) and (48), are considered. In the first approximation, the terms $\frac{\partial^2 \boldsymbol{F}_\mathrm{m}}{\partial (\boldsymbol{F}_\mathrm{M})^2}$ and $\frac{\partial^2 \boldsymbol{F}_\mathrm{m}}{\partial \boldsymbol{F}_\mathrm{M} \partial \mathbf{G}_\mathrm{M}}$ are neglected, yielding,

$$
\frac{\partial^2 \boldsymbol{P}_\mathrm{M}}{\partial (\boldsymbol{F}_\mathrm{M})^2} \approx \frac{1}{V_0} \int_{\Omega_{\mathrm{m}0}} \left(\frac{\partial^2 \boldsymbol{P}_\mathrm{m}}{\partial \boldsymbol{F}_\mathrm{m}^2} - \frac{\partial^2 (\boldsymbol{b}_\mathrm{m} \otimes \boldsymbol{X}_\mathrm{m})}{\partial \boldsymbol{F}_\mathrm{m}^2} \right) :: \left(\frac{\partial \boldsymbol{F}_\mathrm{m}}{\partial \boldsymbol{F}_\mathrm{M}} \otimes \frac{\partial \boldsymbol{F}_\mathrm{m}}{\partial \boldsymbol{F}_\mathrm{M}} \right) \mathrm{d}\Omega , \tag{C.10}
$$

and

$$
\frac{\partial^2 \boldsymbol{P}_\mathrm{M}}{\partial \boldsymbol{F}_\mathrm{M} \partial \mathbf{G}_\mathrm{M}} \approx \frac{1}{V_0} \int_{\Omega_{\mathrm{m}0}} \left(\frac{\partial^2 \boldsymbol{P}_\mathrm{m}}{\partial \boldsymbol{F}_\mathrm{m}^2} - \frac{\partial^2 (\boldsymbol{b}_\mathrm{m} \otimes \boldsymbol{X}_\mathrm{m})}{\partial \boldsymbol{F}_\mathrm{m}^2} \right) :: \left(\frac{\partial \boldsymbol{F}_\mathrm{m}}{\partial \boldsymbol{F}_\mathrm{M}} \otimes \frac{\partial \boldsymbol{F}_\mathrm{m}}{\partial \mathbf{G}_\mathrm{M}} \right) \mathrm{d}\Omega -
$$

$$
\frac{1}{V_0} \int_{\Omega_{\mathrm{m}0}} \left(\frac{\partial^2 (\boldsymbol{b}_\mathrm{m} \otimes \boldsymbol{X}_\mathrm{m})}{\partial \mathbf{G}_\mathrm{M} \partial \boldsymbol{F}_\mathrm{m}} \right) : \frac{\partial \boldsymbol{F}_\mathrm{m}}{\partial \boldsymbol{F}_\mathrm{M}} \mathrm{d}\Omega . \tag{C.11}
$$

In the second approximation, the homogenised tangent at previous step, i.e. $\frac{\partial \boldsymbol{P}_\mathrm{M}}{\partial \boldsymbol{F}_\mathrm{M}}^{(t)}$, is used to evaluate the body force, and we have

$$
\frac{\partial^2 \boldsymbol{P}_\mathrm{M}}{\partial (\boldsymbol{F}_\mathrm{M})^2} = \boldsymbol{0} \text{ and } \frac{\partial^2 \boldsymbol{P}_\mathrm{M}}{\partial \boldsymbol{F}_\mathrm{M} \partial \boldsymbol{G}_\mathrm{M}} = \boldsymbol{0} . \tag{C.12}
$$

Appendix D. Discontinuous Galerkin weak formulation of the macroscopic second-order continuum

The macroscopic continuum follows the homogeneous anisotropic Mindlin strain gradient model. The $\mathcal{C}^0$ elements are used to discretised the macroscopic weak formulation in this work. In order to avoid introducing

extra unknown fields beside the nodal displacements, such as the derivatives of nodal displacements [23], the $\mathcal{C}^1$ continuity at elements interfaces is weakly constrained by using the enriched discontinuous Galerkin (EDG) method [38]. In this section, the enriched discontinuous Galerkin method is briefly recalled.

Appendix D.1. Macroscopic weak form

The strong form of the Mindlin strain gradient continuum in a body Ω_{M0} reads

$$\boldsymbol{B}_M + (\boldsymbol{P}_M - \mathbf{Q}_M \cdot \nabla_{M0}) \cdot \nabla_{M0} = \mathbf{0}, \quad \boldsymbol{X}_M \in \Omega_{M0}, \tag{D.1}$$

where $\boldsymbol{B}_M$ is the applied body force on Ω_{M0} (this is not the volume-average of the micro-structure body force, but an external load). Beside the prescribed displacements, $\boldsymbol{u}_M^0$, and traction, $\boldsymbol{T}_M^0$, on the Dirichlet and Neumann boundary parts, respectively, the prescribed high order boundary conditions for normal gradient of displacements, $D_{M0}\boldsymbol{u}_M^0$ and double traction $\boldsymbol{R}_M^0$ are also enforced,

$$\boldsymbol{u}_M = \boldsymbol{u}_M^0 \quad \forall \boldsymbol{X}_M \in \partial_D \Omega_{M0}, \tag{D.2}$$

$$\boldsymbol{T}_M = \boldsymbol{T}_M^0 \quad \forall \boldsymbol{X}_M \in \partial_N \Omega_{M0}, \tag{D.3}$$

$$D_{M0}\boldsymbol{u}_M = D_{M0}\boldsymbol{u}_M^0 \quad \forall \boldsymbol{X}_M \in \partial_T \Omega_{M0}, \tag{D.4}$$

$$\boldsymbol{R}_M = \boldsymbol{R}_M^0 \quad \forall \boldsymbol{X}_M \in \partial_M \Omega_{M0}. \tag{D.5}$$

Following the Mindlin's theory [5], the gradient is decomposed into a surface gradient $\overset{s}{\nabla}_{M0}$ and a normal part D_{M0} such that

$$\nabla_{M0} = \overset{s}{\nabla}_{M0} + \boldsymbol{N}_{M0} D_{M0}, \tag{D.6}$$

where $\overset{s}{\nabla}_{M0} = (\boldsymbol{I} - \boldsymbol{N}_{M0} \otimes \boldsymbol{N}_{M0}) \cdot \nabla_{M0}$, $D_{M0} = \boldsymbol{N}_{M0} \cdot \nabla_0$ and $\boldsymbol{N}_{M0}$ is the unit outward normal in the reference configuration. The traction per reference unit surface $\boldsymbol{T}_M$ is given by, [36],

$$\boldsymbol{T}_M = (\boldsymbol{P}_M - \mathbf{Q}_M \cdot \nabla_{M0}) \cdot \boldsymbol{N}_{M0} + (\mathbf{Q}_M \cdot \boldsymbol{N}_{M0}) \cdot \left(\boldsymbol{N}_{M0} \overset{s}{\nabla}_{M0} \cdot \boldsymbol{N}_{M0} - \overset{s}{\nabla}_{M0} \right), \tag{D.7}$$

and the double traction $\boldsymbol{R}_M$ reads

$$\boldsymbol{R}_M = \mathbf{Q}_M : (\boldsymbol{N}_{M0} \otimes \boldsymbol{N}_{M0}). \tag{D.8}$$

The strong form (D.1) can be reformulated as

$$\int_{\Omega_{M0}} [\boldsymbol{B}_M + (\boldsymbol{P}_M - \mathbf{Q}_M \cdot \nabla_{M0}) \cdot \nabla_{M0}] \cdot \delta\boldsymbol{u}_M d\Omega = 0. \tag{D.9}$$

for any arbitrary kinematic field $\delta\boldsymbol{u}_M$.

Appendix D.2. FEM discretisation of second-order continuum problem with EDG method.

The macroscopic domain Ω_{M0} is discretised into a group of finite element $\bar{\Omega}_{M0}^e$, such that $\Omega_{M0} \approx \cup_e \bar{\Omega}_{M0}^e$, where $\bar{\Omega}_{M0}^e$ is the union of the open domain Ω_{M0}^e with its boundary $\partial\Omega_{M0}^e$. The boundary $\cup_e \partial\Omega_{M0}^e$ is further divided into internal and external boundary parts which satisfy

$$\cup_e \partial\Omega_{Ext0}^e = \partial\Omega_{M0} \text{ and } \cup_e \partial\Omega_{Int0}^e = \cup_e \partial\Omega_{M0}^e \backslash \partial\Omega_{M0}. \tag{D.10}$$

Using the divergence theorem on the form (D.9) and the boundary conditions Eqs. (D.3) and (D.5), and the relation [44]

$$\int_{\partial\Omega_{M0}} \overset{s}{\nabla}_{M0} \cdot [\delta\boldsymbol{u}_M \cdot \mathbf{Q}_M \cdot \boldsymbol{N}_{M0}] d\Gamma =$$

$$\int_{\partial\Omega_{M0}} \left[\overset{s}{\nabla}_{M0} \cdot \boldsymbol{N}_{M0} \right] \delta\boldsymbol{u}_M \cdot \mathbf{Q}_M : [\boldsymbol{N}_{M0} \otimes \boldsymbol{N}_{M0}] d\Gamma, \tag{D.11}$$

leads to

$$\sum_e \int_{\Omega_{\mathrm{M0}}^e} \left[\boldsymbol{P}_{\mathrm{M}} : \boldsymbol{F}\left(\delta \boldsymbol{u}_{\mathrm{M}}\right) + \mathbf{Q}_{\mathrm{M}} \vdots \mathbf{G}\left(\delta \boldsymbol{u}_{\mathrm{M}}\right) \right] \mathrm{d}\Omega - \sum_e \int_{\partial \Omega_{\mathrm{Int0}}^e} \delta \boldsymbol{u}_{\mathrm{M}} \cdot \left[\boldsymbol{P}_{\mathrm{M}} - \mathbf{Q}_{\mathrm{M}} \cdot \nabla_{\mathrm{M0}} \right] \cdot \boldsymbol{N}_{\mathrm{M0}} \mathrm{d}\Gamma$$

$$- \sum_e \int_{\partial \Omega_{\mathrm{Int0}}^e} \mathbf{Q}_{\mathrm{M}} \vdots (\delta \boldsymbol{u}_{\mathrm{M}} \otimes \nabla_{\mathrm{M0}} \otimes \boldsymbol{N}_{\mathrm{M0}}) \mathrm{d}\Gamma = \int_{\Omega_{\mathrm{M0}}} \boldsymbol{B}_{\mathrm{M}} \cdot \delta \boldsymbol{u}_{\mathrm{M}} \mathrm{d}\Omega +$$

$$\int_{\partial_{\mathrm{N}}\Omega_{\mathrm{M0}}} \boldsymbol{T}_{\mathrm{M}}^0 \cdot \delta \boldsymbol{u}_{\mathrm{M}} \mathrm{d}\Gamma + \int_{\partial_{\mathrm{M}}\Omega_{\mathrm{M0}}} \boldsymbol{R}_{\mathrm{M}}^0 \cdot \mathrm{D}_{\mathrm{M0}} \delta \boldsymbol{u}_{\mathrm{M}} \mathrm{d}\Gamma \,. \tag{D.12}$$

The internal boundary of the mesh discretisation corresponds to the interfaces between two elements arbitrarily denoted "+" and "-", and with outward normal of the minus element denoted by $\boldsymbol{N}_{\mathrm{M0}}^-$. Hence, one has for two neighbouring elements "+" and "-": $\boldsymbol{N}_{\mathrm{M0}}^+ = -\boldsymbol{N}_{\mathrm{M0}}^-$. Then the jump $[\![\bullet]\!]$ and mean $\langle \bullet \rangle$ operators are defined at the element interfaces by

$$[\![\bullet]\!] = \bullet^+ - \bullet^- \text{ and } \langle \bullet \rangle = \frac{1}{2}(\bullet^+ + \bullet^-)\,, \tag{D.13}$$

where $\bullet^+$ and $\bullet^-$ are respectively the tensor variables at the boundary of the "+" and "-" elements. Classical C^0 finite elements are used for the discretisation, and the kinematic field is defined as $\delta \boldsymbol{u}_{\mathrm{M}} \in \mathcal{W}$, where

$$\mathcal{W} = \{\delta \boldsymbol{u}_{\mathrm{M}} \in \mathcal{C}^0\left(\Omega_{\mathrm{M0}}\right) | \text{Eq. (D.2) is satisfied}\}\,, \tag{D.14}$$

so that $\delta \boldsymbol{u}_{\mathrm{M}} \in \mathcal{W}$ is continuous at the element interfaces under the EDG framework [38]. Therefore the third term in $\delta \boldsymbol{u}_{\mathrm{M}} \cdot [\boldsymbol{P}_{\mathrm{M}} - \mathbf{Q}_{\mathrm{M}} \cdot \nabla_{\mathrm{M0}}] \cdot \boldsymbol{N}_{\mathrm{M0}}$ on the left side of Eq. (D.12) can be omitted without altering the consistency of the method. However, the displacement gradients $\delta \boldsymbol{u}_{\mathrm{M}} \otimes \nabla_{\mathrm{M0}}$ are discontinuous across the element interfaces, and the corresponding term on the left side of Eq. (D.12) at the interface of two neighbouring elements is rewritten

$$\int_{\partial \Omega_{\mathrm{0Int}}^{e-}} N_{\mathrm{M0}K}^- Q_{\mathrm{M}iJK}^- \frac{\partial \delta u_{\mathrm{M}i}^-}{\partial X_{\mathrm{M}J}} \mathrm{d}\Gamma + \int_{\partial \Omega_{\mathrm{0Int}}^{e+}} N_{\mathrm{M0}K}^+ Q_{\mathrm{M}iJK}^+ \frac{\partial \delta u_{\mathrm{M}i}^+}{\partial X_{\mathrm{M}J}} \mathrm{d}\Gamma \,. \tag{D.15}$$

Defining the interface elements $s \in \partial_{\mathrm{I}} \Omega_{\mathrm{M0}}$ between all the neighbouring elements, yields

$$\sum_e \int_{\partial \Omega_{\mathrm{0Int}}^e} \mathbf{Q}_{\mathrm{M}} \vdots (\delta \boldsymbol{u}_{\mathrm{M}} \otimes \nabla_{\mathrm{M0}} \otimes \boldsymbol{N}_{\mathrm{M0}}) \, \mathrm{d}\Gamma = - \sum_{s \in \partial_{\mathrm{I}} \Omega_{\mathrm{M0}}} \int_s N_{\mathrm{M0}K}^- \left[\!\left[Q_{\mathrm{M}iJK} \frac{\partial \delta u_{\mathrm{M}i}}{\partial X_{\mathrm{M}J}} \right]\!\right] \mathrm{d}\Gamma \,. \tag{D.16}$$

In the EDG formula [38], an approximated expression is used to replace the jump term in Eq. (D.16) and to enforce the continuity of the displacement gradients $\delta \boldsymbol{u}_{\mathrm{M}} \otimes \nabla_{\mathrm{M0}}$ at element interfaces, which reads

$$\sum_{s \in \partial_{\mathrm{I}} \Omega_{\mathrm{M0}}} \int_s N_{\mathrm{M0}K}^- \left[\!\left[Q_{\mathrm{M}iJK} \frac{\partial \delta u_{\mathrm{M}i}}{\partial X_{\mathrm{M}J}} \right]\!\right] \mathrm{d}\Gamma \approxeq \sum_{s \in \partial_{\mathrm{I}} \Omega_{\mathrm{M0}}} \int_s \left[\!\left[\frac{\partial \delta u_{\mathrm{M}i}}{\partial X_{\mathrm{M}J}} \right]\!\right] H_{iJ} \left(\mathbf{Q}_{\mathrm{M}}^+, \mathbf{Q}_{\mathrm{M}}^-, \boldsymbol{N}_{\mathrm{M0}}^-\right) \mathrm{d}\Gamma\,, \tag{D.17}$$

where $\boldsymbol{H}\left(\mathbf{Q}_{\mathrm{M}}^+, \mathbf{Q}_{\mathrm{M}}^-, \boldsymbol{N}_{\mathrm{M0}}^-\right)$ is the so-called numerical flux. In this work we consider

$$H_{iJ}\left(\mathbf{Q}_{\mathrm{M}}^+, \mathbf{Q}_{\mathrm{M}}^-, \boldsymbol{N}_{\mathrm{M0}}^-\right) =$$

$$\langle Q_{\mathrm{M}iJK} \rangle N_{\mathrm{M0}K}^- + \frac{1}{2} N_{\mathrm{M0}K}^- \left\langle \frac{\beta^{\mathrm{Q}}}{h^{\mathrm{s}}} L_{iJKpQR}^0 \right\rangle \left[\!\left[\frac{\partial u_{\mathrm{M}p}}{\partial X_{\mathrm{M}Q}} \right]\!\right] N_{\mathrm{M0}R}^-\,, \tag{D.18}$$

where β^{Q} is a user stabilisation parameter and h^{s} is the characteristic mesh size of the problem. In [38], the high order tangent operator is defined by $\mathbb{L}^0 = \frac{\partial \mathbf{Q}}{\partial \mathbf{G}}$ and is chosen constant during the simulation. Because the presented method could yield a low or even negative high order modulus, in this work, the following high order operator is adopted to ensure the stability of the method:

$$L_{iJKpQR}^0 = \frac{1}{2V_0} \left[C_{iJpQ}^0 J_{MKR} + C_{iKpQ}^0 J_{MJR} \right]\,, \tag{D.19}$$

where $\mathbb{C}^0 = \frac{\partial \boldsymbol{P}_{\mathrm{M}}}{\partial \boldsymbol{F}_{\mathrm{M}}}$ is the initial homogenised elastic tensor of the RVE. The term $\mathbb{L}^0_{iJKpQR}$ is only computed at the beginning of the simulation and chosen to be constant afterwards. A symmetrisation term is added to the method as classically done in interior penalty DG methods. This term reads

$$\sum_{s \in \partial_{\mathrm{I}} \Omega_{\mathrm{M0}}} \int_s \left[\!\!\left[\frac{\partial u_{\mathrm{M}i}}{\partial X_{\mathrm{M}J}} \right]\!\!\right] H_{iJ}(\mathbf{Q}^+(\delta \boldsymbol{u}_{\mathrm{M}}), \mathbf{Q}^-(\delta \boldsymbol{u}_{\mathrm{M}}), \boldsymbol{N}_{\mathrm{M0}}^-) \mathrm{d}\Gamma = 0, \tag{D.20}$$

where

$$H_{iJ}\left(\mathbf{Q}^+(\delta \boldsymbol{u}_{\mathrm{M}}), \mathbf{Q}^-(\delta \boldsymbol{u}_{\mathrm{M}}), \boldsymbol{N}_{\mathrm{M0}}^-\right) =$$
$$\langle Q_{iJK}(\delta \boldsymbol{u}_{\mathrm{M}}) \rangle N_{\mathrm{M0}K}^- + \frac{1}{2} N_{\mathrm{M0}K}^- \left\langle \frac{\beta^{\mathrm{Q}}}{h^{\mathrm{s}}} L^0_{iJKpQR} \right\rangle \left[\!\!\left[\frac{\partial \delta \boldsymbol{u}_{\mathrm{M}p}}{\partial X_{\mathrm{M}Q}} \right]\!\!\right] N_{\mathrm{M0}R}^-. \tag{D.21}$$

The variation of the high order stress is practically computed using constant elastic operator and reads

$$Q_{iJK}(\delta \boldsymbol{u}_{\mathrm{M}}) = L^0_{iJKpQR} \frac{\partial^2 \delta \boldsymbol{u}_{\mathrm{M}p}}{\partial X_{\mathrm{M}Q} \partial X_{\mathrm{M}R}} + M^{\mathrm{QF0}}_{iJKpQ} \frac{\partial \delta \boldsymbol{u}_{\mathrm{M}p}}{\partial X_{\mathrm{M}Q}}, \tag{D.22}$$

where $\mathbb{M}^{\mathrm{QF0}} = \frac{\partial \mathbf{Q}_{\mathrm{M}}}{\partial \boldsymbol{F}_{\mathrm{M}}}$ is evaluated at the initial time. We note that the numerical flux ensuring the consistency of the method is the $\langle Q_{\mathrm{M}iJK} \rangle N_{\mathrm{M0}K}^-$-term of $H_{iJ}\left(\mathbf{Q}_{\mathrm{M}}^+, \mathbf{Q}_{\mathrm{M}}^-, \boldsymbol{N}_{\mathrm{M0}}^-\right)$ in Eq. (D.18). Neither modifying the penalty coefficient $\left\langle \frac{\beta^{\mathrm{Q}}}{h^{\mathrm{s}}} L^0_{iJKpQR} \right\rangle$ of the stability terms in Eqs. (D.18) and (D.21) nor modifying the symmetrisation term $\langle Q_{iJK}(\delta \boldsymbol{u}_{\mathrm{M}}) \rangle$ in Eq. (D.21) would affect the consistency of the method and thus the converged results, as long as the method is stable which is the case with the assumption of Eq. (D.19).

Eventually, considering Eqs. (D.17) and (D.20), the weak form (D.12) is rewritten

$$\sum_e \int_{\Omega_{\mathrm{M0}}^e} \left[\boldsymbol{P}_{\mathrm{M}} : \boldsymbol{F}(\delta \boldsymbol{u}_{\mathrm{M}}) + \mathbf{Q}_{\mathrm{M}} \dot{:} \mathbf{G}(\delta \boldsymbol{u}_{\mathrm{M}}) \right] \mathrm{d}\Omega$$
$$+ \sum_{s \in \partial_{\mathrm{I}} \Omega_{\mathrm{M0}}} \int_s [\![\delta \boldsymbol{u}_{\mathrm{M}} \otimes \nabla_{\mathrm{M0}}]\!] : \boldsymbol{H}(\mathbf{Q}_{\mathrm{M}}^+, \mathbf{Q}_{\mathrm{M}}^-, \boldsymbol{N}_{\mathrm{M0}}^-) \mathrm{d}\Gamma$$
$$+ \sum_{s \in \partial_{\mathrm{I}} \Omega_{\mathrm{M0}}} \int_s [\![\boldsymbol{u}_{\mathrm{M}} \otimes \nabla_{\mathrm{M0}}]\!] : \boldsymbol{H}(\mathbf{Q}^+(\delta \boldsymbol{u}_{\mathrm{M}}), \mathbf{Q}^-(\delta \boldsymbol{u}_{\mathrm{M}}), \boldsymbol{N}_{\mathrm{M0}}^-) \mathrm{d}\Gamma =$$
$$\int_{\Omega_0} \boldsymbol{B}_{\mathrm{M}} \cdot \delta \boldsymbol{u}_{\mathrm{M}} \mathrm{d}\Omega + \int_{\partial_{\mathrm{N}} \Omega_{\mathrm{M0}}} \boldsymbol{T}_{\mathrm{M}}^0 \cdot \delta \boldsymbol{u}_{\mathrm{M}} \mathrm{d}\Gamma + \int_{\partial_{\mathrm{M}} \Omega_{\mathrm{M0}}} \boldsymbol{R}_{\mathrm{M}}^0 \cdot \mathrm{D}_{\mathrm{M0}} \delta \boldsymbol{u}_{\mathrm{M}} \mathrm{d}\Gamma. \tag{D.23}$$

Without introducing extra degree of freedom, conventional $\mathcal{C}^0$ finite elements can be used to implement Eq. (D.23). More details on the finite element implementation can be found in reference [38].

Appendix E. Finite strain J_2 elasto-plastic material model

The material obeys a finite strain J_2 elasto-plastic constitutive model [45]. The deformation gradient $\mathbf{F}$ is decomposed into the reversible elastic part $\mathbf{F}^{\mathrm{e}}$ and the irreversible plastic part $\mathbf{F}^{\mathrm{p}}$ such that $\mathbf{F} = \mathbf{F}^{\mathrm{e}} \cdot \mathbf{F}^{\mathrm{p}}$. The elastic potential energy is defined as

$$\psi(\mathbf{C}^{\mathrm{e}}) = \frac{K}{2} \ln^2 J + \frac{\mu}{4} (\ln \mathbf{C}^{\mathrm{e}})^{\mathrm{dev}} : (\ln \mathbf{C}^{\mathrm{e}})^{\mathrm{dev}}, \tag{E.1}$$

where $\mathbf{C}^{\mathrm{e}} = \mathbf{F}^{\mathrm{eT}} \cdot \mathbf{F}^{\mathrm{e}}$, and K, and μ correspond to the bulk and shear moduli of the material. The first Piola-Kirchhoff stress tensor $\mathbf{P}$ derives from the elastic potential (E.1) following

$$\mathbf{P} = \frac{\partial \psi(\mathbf{F}; \mathbf{F}^{\mathrm{p}})}{\partial \mathbf{F}} = K \mathbf{F}^{\mathrm{-T}} \ln J + \mu \mathbf{F}^{\mathrm{e}} \cdot \left[\mathbf{C}^{\mathrm{e}\,-1} \cdot (\ln \mathbf{C}^{\mathrm{e}})^{\mathrm{dev}} \right] \cdot \mathbf{F}^{\mathrm{p}\,\mathrm{-T}}. \tag{E.2}$$

The elastic part $\mathbf{F}^{\mathrm{e}}$ and the plastic part $\mathbf{F}^{\mathrm{p}}$ of the deformation gradient are obtained through a J_2 plastic flow expressed in terms of the Kirchhoff stress. The Kirchhoff stress $\boldsymbol{\kappa} = \mathbf{P} \cdot \mathbf{F}^{\mathrm{T}}$ is first computed by Eq. (E.2) as

$$\boldsymbol{\kappa} = K \ln J \mathbf{I} + \mu \mathbf{F}^{\mathrm{e}} \cdot \left[\mathbf{C}^{\mathrm{e}-1} \cdot (\ln \mathbf{C}^{\mathrm{e}})^{\mathrm{dev}} \right] \cdot \mathbf{F}^{\mathrm{e\,T}} . \tag{E.3}$$

The equivalent von Mises stress is then calculated through the deviatoric part of $\boldsymbol{\kappa}$, $i.e.$ $\tau_{eq} = \sqrt{\frac{3}{2} \boldsymbol{\kappa}^{\mathrm{dev}} : \boldsymbol{\kappa}^{\mathrm{dev}}}$. According to the J_2-plasticity theory, the von Mises stress criterion reads

$$f = \tau_{\mathrm{eq}} - \tau_{\mathrm{y}}^0 - R(\gamma) \le 0 , \tag{E.4}$$

where f is the yield surface, τ_{y}^0 is the initial yield stress, γ is the equivalent plastic strain and where the isotropic hardening stress $R(\gamma)$ takes the form

$$R(\gamma) = h\gamma , \tag{E.5}$$

with h a material constant. The evolution of $\mathbf{F}^{\mathrm{p}}$ is determined by the normal plastic flow theory following

$$\dot{\mathbf{F}}^{\mathrm{p}} = \dot{\gamma} \mathbf{N} \cdot \mathbf{F}^{\mathrm{p}} , \tag{E.6}$$

where $\mathbf{N}$ is the normal to the yield surface, see [45] for more details.

[1] S. H. Lee, C. M. Park, Y. M. Seo, Z. G. Wang, C. K. Kim, Acoustic metamaterial with negative modulus, Journal of Physics: Condensed Matter 21 (17) (2009) 175704. doi:10.1088/0953-8984/21/17/175704.
URL https://doi.org/10.1088/0953-8984/21/17/175704

[2] M. Eidini, Zigzag-base folded sheet cellular mechanical metamaterials, Extreme Mechanics Letters 6 (2016) 96–102. doi:https://doi.org/10.1016/j.eml.2015.12.006.
URL https://www.sciencedirect.com/science/article/pii/S2352431615300109

[3] M. Kadic, T. Bckmann, N. Stenger, M. Thiel, M. Wegener, On the practicability of pentamode mechanical metamaterials, Applied Physics Letters 100 (19) (2012) 191901. arXiv:https://doi.org/10.1063/1.4709436, doi:10.1063/1.4709436.
URL https://doi.org/10.1063/1.4709436

[4] X. Zheng, H. Lee, T. H. Weisgraber, M. Shusteff, J. DeOtte, E. B. Duoss, J. D. Kuntz, M. M. Biener, Q. Ge, J. A. Jackson, S. O. Kucheyev, N. X. Fang, C. M. Spadaccini, Ultralight, ultrastiff mechanical metamaterials, Science 344 (6190) (2014) 1373–1377. arXiv:https://www.science.org/doi/pdf/10.1126/science.1252291, doi:10.1126/science.1252291.
URL https://www.science.org/doi/abs/10.1126/science.1252291

[5] R. Mindlin, Microstructure in linear elasticity, arch, Rational Mech. Anal. Vol. 6 (1964) 51–78.

[6] R. A. Toupin, Elastic materials with couple-stresses, Archive for Rational Mechanics and Analysis 11 (1962) 385–414. doi:10.1007/BF00253945.
URL https://doi.org/10.1007/BF00253945

[7] A. Eringen, E. Suhubi, Nonlinear theory of simple micro-elastic solidsi, International Journal of Engineering Science 2 (2) (1964) 189–203. doi:https://doi.org/10.1016/0020-7225(64)90004-7.
URL https://www.sciencedirect.com/science/article/pii/0020722564900047

[8] A. C. Eringen, Microcontinuum field theories: I. Foundations and solids, Springer Science & Business Media, 2012.

[9] W. Nowacki, Theory of asymmetric elasticity, Pergamon Press, Headington Hill Hall, Oxford OX 3 0 BW, UK, 1986.

[10] S. Forest, K. Sab, Cosserat overall modeling of heterogeneous materials, Mechanics Research Communications 25 (4) (1998) 449–454. doi:https://doi.org/10.1016/S0093-6413(98)00059-7.
URL https://www.sciencedirect.com/science/article/pii/S0093641398000597

[11] S. Forest, F. Pradel, K. Sab, Asymptotic analysis of heterogeneous cosserat media, International Journal of Solids and Structures 38 (26) (2001) 4585–4608. doi:https://doi.org/10.1016/S0020-7683(00)00295-X.
URL https://www.sciencedirect.com/science/article/pii/S002076830000295X

[12] S. Barboura, J. Li, Establishment of strain gradient constitutive relations by using asymptotic analysis and the finite element method for complex periodic microstructures, International Journal of Solids and Structures 136-137 (2018) 60–76. doi:https://doi.org/10.1016/j.ijsolstr.2017.12.003.
URL https://www.sciencedirect.com/science/article/pii/S0020768317305383

[13] V. Smyshlyaev, K. Cherednichenko, On rigorous derivation of strain gradient effects in the overall behaviour of periodic heterogeneous media, Journal of the Mechanics and Physics of Solids 48 (6) (2000) 1325–1357. doi:https://doi.org/10.1016/S0022-5096(99)00090-3.
URL https://www.sciencedirect.com/science/article/pii/S0022509699000903

[14] T.-H. Tran, V. Monchiet, G. Bonnet, A micromechanics-based approach for the derivation of constitutive elastic coefficients of strain-gradient media, International Journal of Solids and Structures 49 (5) (2012) 783–792. doi:https://doi.org/10.1016/j.ijsolstr.2011.11.017.
URL https://www.sciencedirect.com/science/article/pii/S0020768311003994

[15] I. Goda, J.-F. Ganghoffer, Construction of first and second order grade anisotropic continuum media for 3d porous and textile composite structures, Composite Structures 141 (2016) 292–327. doi:https://doi.org/10.1016/j.compstruct.2016.01.061.
URL https://www.sciencedirect.com/science/article/pii/S026382231600074X

[16] D. K. Trinh, R. Janicke, N. Auffray, S. Diebels, S. Forest, Evaluation of generalized continuum substitution models for heterogeneous materials, International Journal for Multiscale Computational Engineering 10 (6) (2012) 527–549.

[17] A. Bacigalupo, L. Gambarotta, Homogenization of periodic hexa- and tetrachiral cellular solids, Composite Structures 116 (2014) 461–476. doi:https://doi.org/10.1016/j.compstruct.2014.05.033.
URL https://www.sciencedirect.com/science/article/pii/S0263822314002438

[18] P. Trovalusci, M. Ostoja-Starzewski, M. L. De Bellis, A. Murrali, Scale-dependent homogenization of random composites as micropolar continua, European Journal of Mechanics - A/Solids 49 (2015) 396–407. doi:https://doi.org/10.1016/j.euromechsol.2014.08.010.
URL https://www.sciencedirect.com/science/article/pii/S0997753814001223

[19] X. Yuan, Y. Tomita, T. Andou, A micromechanical approach of nonlocal modeling for media with periodic microstructures, Mechanics Research Communications 35 (1) (2008) 126–133, multiscale Modeling. doi:https://doi.org/10.1016/j.mechrescom.2007.07.004.
URL https://www.sciencedirect.com/science/article/pii/S0093641307000419

[20] K. Berkache, S. Deogekar, I. Goda, R. Picu, J.-F. Ganghoffer, Construction of second gradient continuum models for random fibrous networks and analysis of size effects, Composite Structures 181 (2017) 347–357. doi:https://doi.org/10.1016/j.compstruct.2017.08.078.
URL https://www.sciencedirect.com/science/article/pii/S0263822317313508

[21] J. Yvonnet, N. Auffray, V. Monchiet, Computational second-order homogenization of materials with effective anisotropic strain-gradient behavior, International Journal of Solids and Structures 191-192 (2020) 434–448. doi:https://doi.org/10.1016/j.ijsolstr.2020.01.006.
URL https://www.sciencedirect.com/science/article/pii/S0020768320300123

[22] F. Feyel, A multilevel finite element method (fe2) to describe the response of highly non-linear structures using generalized continua, Computer Methods in Applied Mechanics and Engineering 192 (28) (2003) 3233–3244, multiscale Computational Mechanics for Materials and Structures. doi:https://doi.org/10.1016/S0045-7825(03)00348-7.
URL https://www.sciencedirect.com/science/article/pii/S0045782503003487

[23] V. Kouznetsova, M. Geers, W. Brekelmans, Multi-scale second-order computational homogenization of multi-phase materials: a nested finite element solution strategy, Computer Methods in Applied Mechanics and Engineering 193 (48-51) (2004) 5525 – 5550, advances in Computational Plasticity. doi:DOI:10.1016/j.cma.2003.12.073.

[24] P. Blanco, P. Snchez, E. de Souza Neto, R. Feijo, The method of multiscale virtual power for the derivation of a second order mechanical model, Mechanics of Materials 99 (2016) 53–67. doi:https://doi.org/10.1016/j.mechmat.2016.05.003.
URL https://www.sciencedirect.com/science/article/pii/S0167663616300400

[25] O. Roko, M. Ameen, R. Peerlings, M. Geers, Micromorphic computational homogenization for mechanical metamaterials with patterning fluctuation fields, Journal of the Mechanics and Physics of Solids 123 (2019) 119–137, the N.A. Fleck 60th Anniversary Volume. doi:https://doi.org/10.1016/j.jmps.2018.08.019.
URL https://www.sciencedirect.com/science/article/pii/S0022509618306148

[26] S. van Bree, O. Rokoš, R. Peerlings, M. Doškář, M. Geers, A newton solver for micromorphic computational homogenization enabling multiscale buckling analysis of pattern-transforming metamaterials, Computer Methods in Applied Mechanics and Engineering 372 (2020) 113333. doi:https://doi.org/10.1016/j.cma.2020.113333.
URL https://www.sciencedirect.com/science/article/pii/S0045782520305181

[27] R. Biswas, L. Poh, A. Shedbale, A micromorphic computational homogenization framework for auxetic tetra-chiral structures, Journal of the Mechanics and Physics of Solids 135 (2020) 103801. doi:https://doi.org/10.1016/j.jmps.2019.103801.
URL https://www.sciencedirect.com/science/article/pii/S0022509619307203

[28] L. Kaczmarczyk, C. J. Pearce, N. Bićanić, Scale transition and enforcement of rve boundary conditions in second-order computational homogenization, International Journal for Numerical Methods in Engineering 74 (3) (2008) 506–522. arXiv:https://onlinelibrary.wiley.com/doi/pdf/10.1002/nme.2188, doi:https://doi.org/10.1002/nme.2188.
URL https://onlinelibrary.wiley.com/doi/abs/10.1002/nme.2188

[29] A. Bacigalupo, L. Gambarotta, Second-order computational homogenization of heterogeneous materials with periodic microstructure, ZAMM - Journal of Applied Mathematics and Mechanics / Zeitschrift fr Angewandte Mathematik und Mechanik 90 (10-11) (2010) 796–811. arXiv:https://onlinelibrary.wiley.com/doi/pdf/10.1002/zamm.201000031, doi:https://doi.org/10.1002/zamm.201000031.
URL https://onlinelibrary.wiley.com/doi/abs/10.1002/zamm.201000031

[30] C. Huet, Application of variational concepts to size effects in elastic heterogeneous bodies, Journal of the Mechanics and Physics of Solids 38 (6) (1990) 813–841. doi:https://doi.org/10.1016/0022-5096(90)90041-2.
URL https://www.sciencedirect.com/science/article/pii/0022509690900412

[31] M. Ostoja-Starzewski, S. D. Boccara, I. Jasiuk, Couple-stress moduli and characteristics length of a two-phase composite, Mechanics Research Communications 26 (4) (1999) 387–396. doi:https://doi.org/10.1016/S0093-6413(99)00039-7.
URL https://www.sciencedirect.com/science/article/pii/S0093641399000397

[32] J. Li, Establishment of strain gradient constitutive relations by homogenization, Comptes Rendus Mcanique 339 (4) (2011) 235–244. doi:https://doi.org/10.1016/j.crme.2011.02.002.
URL https://www.sciencedirect.com/science/article/pii/S1631072111000271

[33] V. Monchiet, N. Auffray, J. Yvonnet, Strain-gradient homogenization: A bridge between the asymptotic expansion and quadratic boundary condition methods, Mechanics of Materials 143 (2020) 103309. doi:https://doi.org/10.1016/j.mechmat.2019.103309.
URL https://www.sciencedirect.com/science/article/pii/S0167663619308385

[34] K. Bertoldi, M. C. Boyce, Wave propagation and instabilities in monolithic and periodically structured elastomeric materials undergoing large deformations, Phys. Rev. B 78 (2008) 184107. doi:10.1103/PhysRevB.78.184107.
URL https://link.aps.org/doi/10.1103/PhysRevB.78.184107

[35] K. Bertoldi, M. Boyce, S. Deschanel, S. Prange, T. Mullin, Mechanics of deformation-triggered pattern transformations and superelastic behavior in periodic elastomeric structures, Journal of the Mechanics and Physics of Solids 56 (8) (2008) 2642–2668. doi:https://doi.org/10.1016/j.jmps.2008.03.006.
URL https://www.sciencedirect.com/science/article/pii/S0022509608000434

[36] V. Kouznetsova, Computational homogenization for the multi-scale analysis of multi-phase materials, Ph.D. thesis, Mechanical Engineering (2002). doi:10.6100/IR560009.

[37] V.-D. Nguyen, L. Noels, Computational homogenization of cellular materials, International Journal of Solids and Structures 51 (11) (2014) 2183–2203. doi:https://doi.org/10.1016/j.ijsolstr.2014.02.029.
URL https://www.sciencedirect.com/science/article/pii/S0020768314000778

[38] V.-D. Nguyen, G. Becker, L. Noels, Multiscale computational homogenization methods with a gradient enhanced scheme based on the discontinuous galerkin formulation, Computer Methods in Applied Mechanics and Engineering 260 (2013) 63–77. doi:https://doi.org/10.1016/j.cma.2013.03.024.
URL https://www.sciencedirect.com/science/article/pii/S0045782513000832

[39] J. Hutchinson, N. Fleck, Strain gradient plasticity, Advances in applied mechanics 33 (1997) 295–361.

[40] M. Poncelet, A. Somera, C. Morel, C. Jailin, N. Auffray, An experimental evidence of the failure of cauchy elasticity for the overall modeling of a non-centro-symmetric lattice under static loading, International Journal of Solids and Structures 147 (2018) 223–237. doi:https://doi.org/10.1016/j.ijsolstr.2018.05.028.
URL https://www.sciencedirect.com/science/article/pii/S0020768318302221

[41] V.-D. Nguyen, L. Wu, L. Noels, Unified treatment of microscopic boundary conditions and efficient algorithms for estimating tangent operators of the homogenized behavior in the computational homogenization method, Computational Mechanics 59 (3) (2017) 483–505.

[42] M. Ainsworth, Essential boundary conditions and multi-point constraints in finite element analysis, Computer Methods in Applied Mechanics and Engineering 190 (48) (2001) 6323–6339. doi:https://doi.org/10.1016/S0045-7825(01)00236-5.
URL https://www.sciencedirect.com/science/article/pii/S0045782501002365

[43] A. K. Hii, B. El Said, A kinematically consistent second-order computational homogenisation framework for thick shell models, Computer Methods in Applied Mechanics and Engineering 398 (2022) 115136. doi:https://doi.org/10.1016/j.cma.2022.115136.
URL https://www.sciencedirect.com/science/article/pii/S0045782522003139

[44] R. Mindlin, Second gradient of strain and surface-tension in linear elasticity, International Journal of Solids and Structures 1 (4) (1965) 417–438. doi:https://doi.org/10.1016/0020-7683(65)90006-5.
URL https://www.sciencedirect.com/science/article/pii/0020768365900065

[45] A. Cuitino, M. Ortiz, A material-independent method for extending stress update algorithms from small-strain plasticity to finite plasticity with multiplicative kinematics, Engineering computations 9 (1992) 437–437.